



5-2018

Development and application of synchronized wide-area power grid measurement

Wenxuan Yao

University of Tennessee, wyao3@vols.utk.edu

Follow this and additional works at: https://trace.tennessee.edu/utk_graddiss

Recommended Citation

Yao, Wenxuan, "Development and application of synchronized wide-area power grid measurement. " PhD diss., University of Tennessee, 2018.
https://trace.tennessee.edu/utk_graddiss/4938

This Dissertation is brought to you for free and open access by the Graduate School at TRACE: Tennessee Research and Creative Exchange. It has been accepted for inclusion in Doctoral Dissertations by an authorized administrator of TRACE: Tennessee Research and Creative Exchange. For more information, please contact trace@utk.edu.

To the Graduate Council:

I am submitting herewith a dissertation written by Wenxuan Yao entitled "Development and application of synchronized wide-area power grid measurement." I have examined the final electronic copy of this dissertation for form and content and recommend that it be accepted in partial fulfillment of the requirements for the degree of Doctor of Philosophy, with a major in Electrical Engineering.

Yilu Liu, Major Professor

We have read this dissertation and recommend its acceptance:

Wei Gao, Mingzhou Jin, Hairong Qi

Accepted for the Council:

Dixie L. Thompson

Vice Provost and Dean of the Graduate School

(Original signatures are on file with official student records.)

Development and application of synchronized
wide-area power grid measurement

A Dissertation Presented for the
Doctor of Philosophy
Degree

The University of Tennessee, Knoxville

Wenxuan Yao

May 2018

Copyright © 2018 by Wenxuan Yao

All rights reserved.

To my beloved wife, Kanghong He and daughter, Grace Yao. You have made me happier, better and stronger than I could have ever imagined. I love you with all my heart.

ACKNOWLEDGEMENTS

I am grateful to everyone who has helped me to achieve my dream of becoming a Ph. D in the University of Tennessee.

First I would like to express my deepest gratitude to my advisor, Dr. Yilu Liu for her continuous guidance and persistent help in my journey in the United States. She is a great advisor for my research and a wise mentor for my personal development. Thank you for your support and friendship. I would also like to thank my dissertation committee members, Dr. Hairong Qi, Dr. Wei Gao, and Dr. Mingzhou Jin. I appreciate their constructive suggestions and comments on my research and dissertation.

Many thanks to members of Power IT Laboratory, Dr. Yong Liu, Dr. Shutang You, Dr. Dao Zhou, Dr. Lingwei Zhan, Dr. Jiecheng Zhao, Dr. Lin Zhu, Dr. Gefei Kou, Dr. Jiahui Guo, Dr. Yin Lei, Dr. Ye Zhang, Dr. Jidong Chai, Dr. Hesen Liu, Dr. Micah J. Till, Dr. Yingchen Zhang, Dr. Feifei Bai, Dr. Yi Cui, Dr. Zhuohong Pan, Dr. Yao Zhang, Dr. Yue Xiang, Yinfeng Zhao, Yu Su, Weikang Wang, Xuemeng Zhang, Yicheng Li. I am greatly appreciative of friendship and help they have given to me.

I also would like to thank David Wells and SmartSenseCom for their help to my research.

I am greatly appreciative of the consistent support and encouragement from Dr. Zhaosheng Teng and Dr. Qiu Tang in Hunan University.

In addition, I would like to thank all my friends in Knoxville. I could not have the memorable time there without your friendship.

Last but not least I would like to express my deepest love to my family: my father Limin Yao, my mother Minzhi He for their endless love and support.

How time flies! I will cherish my four years in the Knoxville as one of my best memories.

ABSTRACT

Phasor measurement units (PMUs) provide an innovative technology for real-time monitoring of the operational state of entire power systems and significantly improve power grid dynamic observability. This dissertation focuses on development and application of synchronized power grid measurements. The contributions of this dissertation are as followed:

First, a novel method for successive approximation register analog to digital converter control in PMUs is developed to compensate for the sampling time error caused by the division remainder between the desirable sampling rate and the oscillator frequency. A variable sampling interval control method is presented by interlacing two integers under a proposed criterion. The frequency of the onboard oscillator is monitored in using the PPS from GPS.

Second, the prevalence of GPS signal loss (GSL) on PMUs is first investigated using real PMU data. The correlation between GSL and time, spatial location, solar activity are explored via comprehensive statistical analysis. Furthermore, the impact of GSL on phasor measurement accuracy has been studied via experiments. Several potential solutions to mitigate the impact of GSL on PMUs are discussed and compared.

Third, PMU integrated the novel sensors are presented. First, two innovative designs for non-contact PMUs presented. Compared with conventional synchrophasors, non-contact PMUs are more flexible and have lower costs. Moreover, to address nonlinear issues in conventional CT and PT, an optical sensor is used for signal acquisition in PMU. This is the first time the utilization of an optical sensor in PMUs has ever been reported.

Fourth, the development of power grid phasor measurement function on an Android based mobile device is developed. The proposed device has the advantages of flexibility, easy installation, lower cost, data visualization and built-in communication channels, compared with conventional PMUs.

Fifth, an identification method combining a wavelet-based signature extraction and artificial neural network based machine learning, is presented to identify the location of unsourced measurements. Experiments at multiple geographic scales are performed to validate the effectiveness of the proposed method using ambient frequency measurements. Identification accuracy is presented and the factors that affect identification performance are discussed.

TABLE OF CONTENTS

Chapter 1	Introduction	1
1.1	Phasor measurement	1
1.2	Frequency monitoring network	3
1.3	Motivation and objective	7
1.3.1	FDR calibration and sampling control	7
1.3.2	GPS signal loss issues	9
1.3.3	Integration with novel sensors.....	9
1.3.4	Development of PMU on mobile platform	10
1.3.5	ENF application using phasor measurement	10
1.4	Organization of study	11
Chapter 2	GPS Signal Based Self-Adaptive Sampling Control for Phasor Measurement ..	13
2.1	Background and motivation	13
2.2	Analysis of sampling time error and its impacts	14
2.2.1	GPS-disciplined sampling method.....	15
2.2.2	Sampling-time error	15
2.2.3	Oscillator frequency drift	19
2.3	Proposed sampling method.....	20
2.3.1	Variable sampling interval control.....	20
2.3.2	Oscillator frequency monitor	21
2.3.3	Complete process for the proposed sampling method	23
2.4	Simulation and implementation result.....	24
2.4.1	Simulation	24
2.4.2	Laboratory experiment	27
2.5	Conclusion	32

Chapter 3	Impact of GPS Signal Loss and Its Mitigation on Phasor Measurement Units ..	34
3.1	Background and motivation	34
3.2	Methodology for GSL prevalence analysis	35
3.3	Analysis results of GSL prevalence analysis in PMU	36
3.3.1	Presence of GSL in PMUs	36
3.3.2	GSL event recovery time.....	38
3.3.3	Spatial-temporal analysis of GSL event.....	38
3.3.4	Daily pattern of GPS sign strength.....	40
3.4	Impact analysis of GSL on PMU measurement	41
3.4.1	Analysis of timing error after losing GPS signal	41
3.4.2	Impact of timing error on measurement.....	41
3.5	Impact test of GSL in SMDs	42
3.5.1	PPS timing error test	42
3.5.2	Test with a signal generator	44
3.5.3	Test with real power grid signals	48
3.6	Potential solutions for GPS signal loss on PMU	48
3.6.1	Angle Compensation Solution	49
3.6.2	Supplementary timing source solution.....	51
3.6.3	Discussion	53
3.7	Conclusion	53
Chapter 4	Phasor Measurement Integrated with Novel Sensors.....	55
4.1	Introduction	55
4.2	Theoretical foundation.....	56
4.2.1	Acquisition of electric field signal	56
4.2.2	Acquisition of magnetic field signal	58

4.3	Device prototype development	60
4.4	Performance evaluation	61
4.4.1	Laboratory experiment	61
4.4.2	Field experiment.....	65
4.5	Optical sensor based PMU	69
4.5.1	Motivation	69
4.5.2	Performance evaluation of optical sensor based PMU.....	70
4.6	Conclusion	73
Chapter 5	Power Grid Monitoring on Mobile Platform.....	75
5.1	Introduction	75
5.2	Phasor measurement on mobile device	77
5.2.1	Overview of hardware design	77
5.2.2	Overview of software design.....	80
5.2.3	GUI design on mobile platform	81
5.2.4	Phasor calculation	82
5.2.5	Frequency accuracy enhancement.....	84
5.2.6	Single-phase angle accuracy enhancement	85
5.2.7	Harmonic distortion calculation	85
5.3	Time synchronization on mobile platform	89
5.3.1	NTP based time synchronization.....	89
5.3.2	GPS based time synchronization.....	89
5.3.3	Sampling interval control	89
5.4	Performance evaluation	91
5.4.1	Experiment setup.....	91
5.4.2	Signals from Doble F6150	91

5.4.3	Signals from power grid.....	93
5.5	Power grid disturbance event detection.....	95
5.5.1	Event detection mechanism.....	95
5.5.2	Detected event.....	97
5.6	Conclusion.....	98
Chapter 6	Source Location Identification of Electric Network Frequency Signals.....	100
6.1	Introduction	100
6.2	ENF reference database	101
6.3	Methodology.....	103
6.3.1	Signature extraction.....	103
6.3.2	Location identification	105
6.4	Performance evaluation	109
6.4.1	Model training	109
6.4.2	Results of location Identification	109
6.4.3	Discussion	112
6.5	Conclusion.....	114
List of References	116
Appendix	124
Appendix A	125
Appendix B	128
Vita	129

LIST OF TABLES

Table 1.1 Comparison of calibration methods	8
Table 2.1 Result summary and comparison	26
Table 2.2 Result summary for laboratory experiment	30
Table 3.1 Test result of timing error	44
Table 3.2 Angle measurement result comparison using compensation method	50
Table 3.3 Angle measurement result comparison	52
Table 4.1 Dimensions of Electric Field Sensor.....	58
Table 4.2 Dimensions of magnetic field sensor	60
Table 4.3 Maximum error for frequency (Hz) and angle (°)	63
Table 4.4 Standard deviation of frequency error (Hz)	64
Table 4.5 Standard deviation of angle error (°)	64
Table 4.6 Measurement error	69
Table 4.7 Frequency errors of PT-FDR and OPS-FDR (Hz).....	73
Table 4.8 Accuracy of OPS-FDR with power grid singal	73
Table 5.1 Measurement error comparison	93
Table 6.1 Accuracy for FDR location identification.....	110
Table 6.2 Confusion matrix for case I with a 1-month time interval.....	111
Table 6.3 Confusion matrix for case I with a 12-month time interval	111
Table 6.4 Comparison of normalized cross-correlation of extracted signature	113

LIST OF FIGURES

Figure 1.1. Synchronized phasor representations of sinusoid waveforms	1
Figure 1.2. PMU installation and connection diagram	2
Figure 1.3. PMU hardware architecture	2
Figure 1.4. FDR deployment map in North America.....	3
Figure 1.5. World map of FDRs.....	4
Figure 1.6. Second generation FDR.....	4
Figure 1.7. Architecture of FNET data center.....	5
Figure 1.8. FNET/GridEye real-time frequency and angle visualization	6
Figure 1.9 Example of the disturbance detection recognition and location report	7
Figure 1.10. FDR calibration	8
Figure 2.1. The role of the PPS signal in waveform sampling	15
Figure 2.2. Schematic diagram of the sampling error for GPS-disciplined sample process....	16
Figure 2.3. Sampling time error for N_L and N_H	17
Figure 2.4. Frequency and angle error caused by sampling time error.....	18
Figure 2.5. Sampling time error caused by oscillator frequency drift	19
Figure 2.6. Variable sample interval control with FP=0.5	21
Figure 2.7. Variable sampling interval control strategy.....	21
Figure 2.8. Monitoring of oscillator frequency	22
Figure 2.9. Flowchart of the proposed method	24
Figure 2.10. Selection of N_k	25
Figure 2.11. Average TPR in a one second period	25
Figure 2.12. Sampling time error comparison	26
Figure 2.13. Comparison of angle and frequency results.....	27
Figure 2.14. Experiment settings	28
Figure 2.15. Illustration of SAR ADC control.....	28
Figure 2.16. Comparison of angle and frequency results.....	29
Figure 2.17. The curve of oscillator frequency drift	31
Figure 2.18. Comparison of angle and frequency results.....	31
Figure 3.1. Illustration of PMU with GPS time synchronization.....	34
Figure 3.2. Methodology for PMU GSL prevalence analysis.....	36

Figure 3.3. Presence of GSL in PMUs from 2010 to 2012	37
Figure 3.4. Probability distribution of GPS signal recovery time.....	38
Figure 3.5. Spatial distribution of GSL in North America.....	39
Figure 3.6. Correlation analysis of GSL and solar activity.....	39
Figure 3.7. Monthly distribution of GSL in PMU	39
Figure 3.8. Daily pattern of GSS in FDR.....	40
Figure 3.9. PPS error from a GPS receiver when GPS signal is lost	42
Figure 3.10. Accumulated time drift when GPS signal is lost.....	43
Figure 3.11. Pattern of the output PPS when GPS signal is lost.....	43
Figure 3.12. Block diagram of the test system.....	44
Figure 3.13. The test system setup	45
Figure 3.14. Test results with the signal generator	46
Figure 3.15. Test results with real power grid signals	47
Figure 3.16. Monitoring of crystal oscillator frequency	50
Figure 3.17. Angle measurement test result.....	51
Figure 3.18. Test setup block for the supplementary timing source solution	52
Figure 3.19. Angle measurement comparison for the supplementary timing source solution.	52
Figure 4.1. Electric field calculation of three straight power line conductors	56
Figure 4.2. Illustration of electric field sensor and amplifier circuit	58
Figure 4.3. Magnetic field strength of three infinite straight conductors.....	59
Figure 4.4. Illustration of magnetic field sensor and amplifier circuit.....	59
Figure 4.5. Hardware design of the E-NCSMD and M-NCSMD	61
Figure 4.6. Illustration of synchronous sampling for phasor measurement.....	61
Figure 4.7. Laboratory experiment setup	62
Figure 4.8. Angle measurement results.....	62
Figure 4.9. Frequency measurement results.....	63
Figure 4.10. Field experiment setup.....	65
Figure 4.11. Waveforms captured by three types of sensors	66
Figure 4.12. Harmonic component analysis.....	66
Figure 4.13. Angle measurement results.....	67
Figure 4.14. Frequency measurement results.....	68

Figure 4.15. Distribution of angle measurement.....	68
Figure 4.16. Distribution of frequency measurement	69
Figure 4.17. Experiment setup	71
Figure 4.18. Test results with real power grid signals	72
Figure 5.1. Hardware design of the proposed mobile device.....	78
Figure 5.2. Arduino Uno board.....	79
Figure 5.3. PCB of data acquisition board	79
Figure 5.4. Prototype of data acquisition board	79
Figure 5.5. Illustration of software designs of the mobile device	80
Figure 5.6. Arduino development environment	80
Figure 5.7. Software development on Android Studio	81
Figure 5.8. Illustration of re-sampling procedure	84
Figure 5.9. Spectral leakage and picket fence effects of FFT due to asynchronous sampling	87
Figure 5.10. NTP based synchronized sampling control technology.....	88
Figure 5.11. Illustration of synchronized sampling control strategy	90
Figure 5.12. Experiment Setup	91
Figure 5.13. Measurement result for input signals from Doble F1650.....	92
Figure 5.14. Measurement result for input signal from distribution level power grid.....	94
Figure 5.15. The flowchart of the distributed event trigger	96
Figure 5.16. The illustration of major voting process for event trigger	96
Figure 5.17. Frequency plots during power system disturbance events	97
Figure 6.1. The framework of FNET/GridEye system	102
Figure 6.2. Plot of FDR measurement and ENF extracted from an audio recording.....	103
Figure 6.3. The plot of frequency measurements recorded on difference locations in EI	105
Figure 6.4. Flowchart of the signature extraction from raw ENF signal	105
Figure 6.5. Signature extraction from ENF signal using wavelet transform	106
Figure 6.6. Spectrum distribution of extracted signature from raw ENF signal	106
Figure 6.7. Structure of the F-ANN	107
Figure 6.8. Illustration of location identification of extracted signatures from	108
Figure 6.9. Map of FDR locations for Case I and Case II	108
Figure 6.10. Map of FDR locations for Case III.....	108

Figure 6.11. Identification accuracy versus the time interval used.....	112
Figure 6.12. Comparison of extracted signatures from ENF signals	114
Figure 6.13. The probability distribution of normalized cross-correlation.....	114

Chapter 1 Introduction

1.1 Phasor measurement

Phasor measurement is one of the key elements of wide area measurement systems (WAMS) in advanced power system monitoring, protection, transient stability assessment, inertia change identification, model validation and control application [1]-[6]. Synchrophasor measurements can provide a unique capability to monitor system dynamics in wide area and in real-time, as well as the possibility of controlling and protecting the electric power system. The idea of performing wide area phasor measurement using phasor measurement units (PMUs) is originated from the research on computer-based relaying of transmission lines in 1977 [7][8]. Due to the help of Global Positioning System (GPS) for synchronization, the first PMU prototype was invented in 1988 and then the first commercial PMU was built in 1992. Since PMUs are able to significantly improve the observability of system status, the importance of PMUs is being gradually recognized by the power system industry [9].

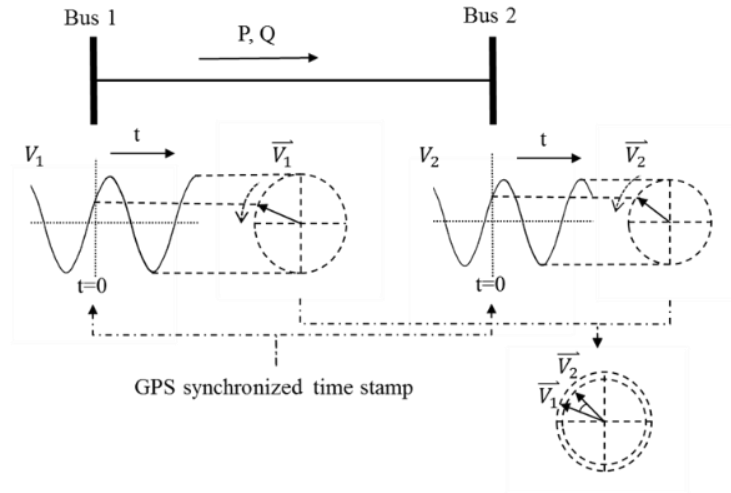


Figure 1.1. Synchronized phasor representations of sinusoid waveforms

The concept of phasor measurement and the basics of PMUs will be introduced in this section. Figure 1.1 shows the sinusoidal voltage waveforms at both the sending and receiving ends of a transmission line and their phasor representations \vec{V}_1 and \vec{V}_2 . (DFT), these two phasors can be calculated using Discrete Fourier transform. Most importantly, these two phasor representations

sharing the same time reference from GPS satellites, which are time-stamped and sent to the control room respectively from two different locations. Therefore, though measurements may not arrive simultaneously due to communication delays, they can be aligned and compared using same GPS time reference at the data center.

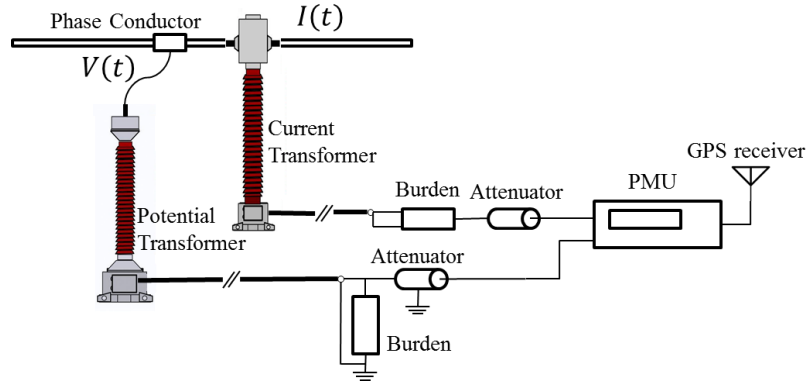


Figure 1.2. PMU installation and connection diagram

PMUs are mainly installed at the high-voltage side requiring three phases current and voltage input signals. A diagram of the typical PMU installation on one phase at a substation is shown in Figure 1.2. The current transformer (CT) and potential transformer (PT) scale down the current and voltage of the high voltage buses to fit the input ranges of the A/D converters in the PMU. The burdens in Figure 1.2 represent the VA rating of the electronic instruments connected to the PT/CT secondary circuits and the attenuators are used for adjusting the output amplitudes further. Due to the high installation and manufactory costs of PTs and CTs, PMUs are installed only at the most important nodes of the power system at current state.

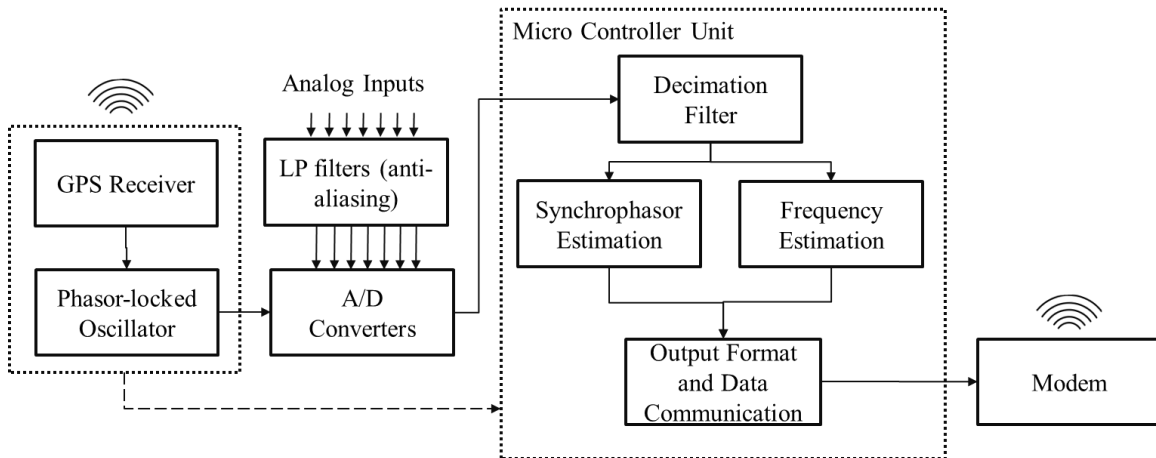


Figure 1.3. PMU hardware architecture

A typical hardware structure of PMU is shown in Figure 1.3. The analog inputs from CT and PT will first go through a low-pass filter to cut off high frequency interference. The Micro Controller Unit performs phasor and frequency estimation using the sampled digital data. The accuracy requirement of phasor measurement is defined in IEEE standard C37.118.1[10]. To address data transmission delays from PMUs to the phasor data concentrators (PDCs) via the communication network, the phasor measurement data are stamped with Universal Time Coordinated (UTC) time index and send to a phasor data concentrator (PDC) on the standard communication protocol C37.118.1[11].

1.2 Frequency monitoring network

As a member of the PMU family, the Frequency Monitoring Network (FNET) developed by the Power IT Laboratory at the University of Tennessee, Knoxville is a low-cost, GPS-synchronized wide area power system voltage, angle and frequency measurement network [9],[12]. As the synchronized single-phase measurement device of FNET, the Frequency Disturbance Recorder (FDR) uses one phase at the distribution level (120 V electrical outlets) to measure voltage amplitude, phase angle, and frequency. The measurement data are then transmitted via the Internet to the FNET servers. Up to Nov.2017, there are about 250 FDRs installed in the United States and about 50 FDRs installed worldwide. Figure 1.4 shows the map of FDRs location in North America, and Figure 1.5 shows the world map of FDRs [13].



Figure 1.4. FDR deployment map in North America

To realize the phasor measurement at as many locations as possible, the FDR was designed to be deployed at the low voltage power grid instead of high voltage substations or power plants [14]. Therefore, the high manufactory cost of PT and CT for conventional PMUs can be waived and the installation cost can be reduced.

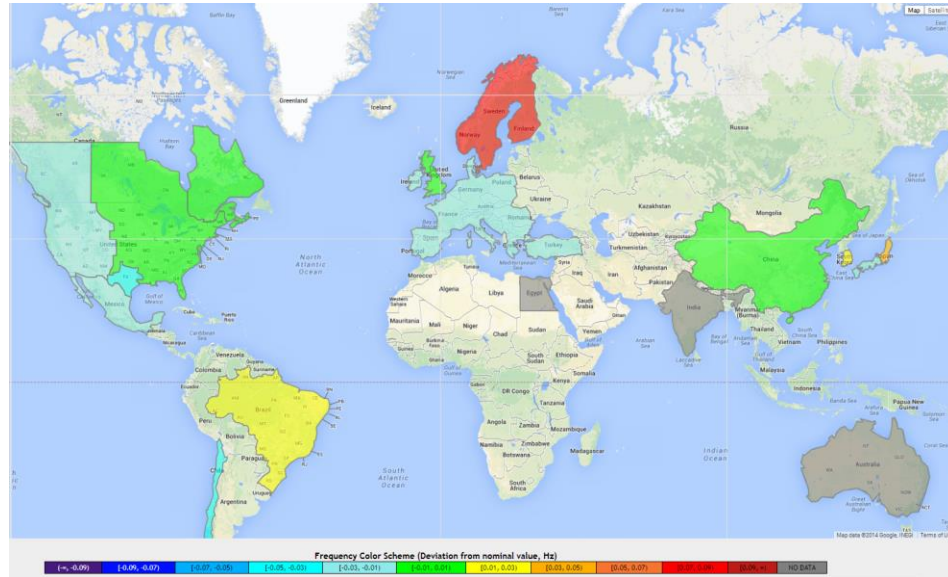


Figure 1.5. World map of FDRs

Three generations of FDR have been developed since 2003 in order to improve measurement accuracy and add more measurement functions [15]. Figure 1.6 shows the second generation FDR which is the most widely deployed so far. Its measurement accuracy reaches ± 0.0005 Hz in terms of frequency and ± 0.0002 rad in terms of voltage angle.



Figure 1.6. Second generation FDR

Employing a multi-layer architecture, the FNET/GridEye data center is designed to receive, process, utilize, and archive a large volume of phasor measurements in real-time. Its main structure is shown in Figure 1.7.

The first layer of the data center is the data concentrator, where the measurement data packages are extracted and forwarded to the subsequent layers. The bad data will be labeled and abandoned. The second layer includes two agents: the storage agent and the real-time application agent. Various FNET/GridEye real-time application modules are running on the real-time application agent to monitor power grid status by scanning the data streaming in. For example, on this agent, the real-time disturbance detection module sends out alerts to system operators once it detects the occurrence of a disturbance. Meanwhile, the data storage agent archives phasor measurement data streams and outputs from the real-time application agent for off-line applications. All the data are archived in an efficient format to preserve data integrity while saving space. In the third layer, the non-real-time application agent runs offline applications to further exploit the archived data. The multi-layer structure of the FNET/GridEye data center facilitates the concentrating, processing, and archiving of a large volume of phasor measurements so as to successfully meet the timeliness requirements of various applications [16].

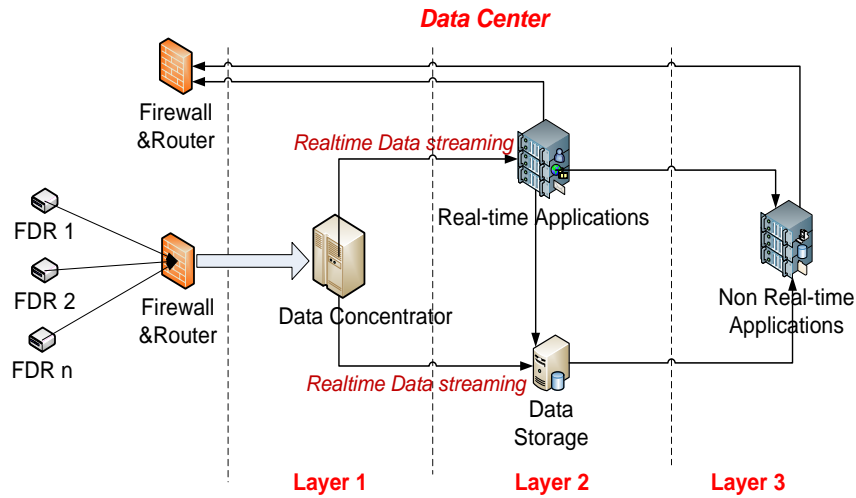
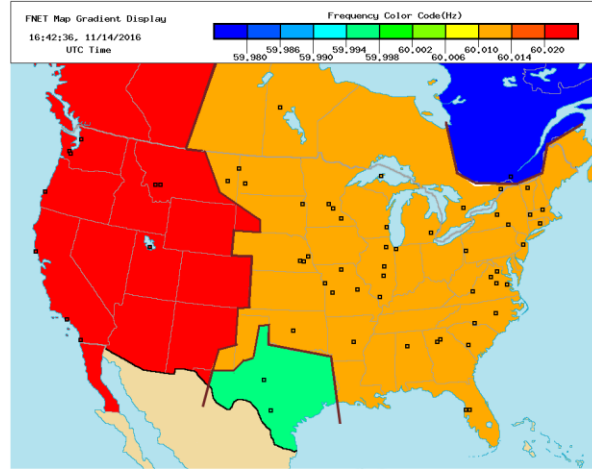
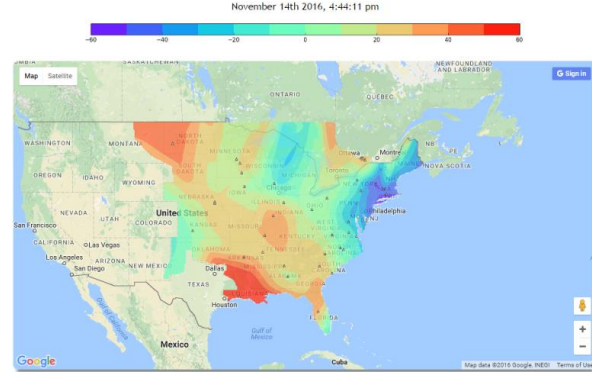


Figure 1.7. Architecture of FNET data center

Figure 1.8(a) shows a snapshot of the real-time frequency display of different U.S. power grids while Figure 1.8(b) presents a snapshot of the real-time voltage angle display of the U.S. Eastern Interconnection (EI). These real-time displays are also available on the FNET/GridEye website [12].



(a) frequency



(b) angle

Figure 1.8. FNET/GridEye real-time frequency and angle visualization

Since any frequency and voltage angle deviation indicates a system operation status change, this web-based application helps system operators capture the most recent variations of the grid status. It is the first time the entire U.S. power grid status can be real-time visualized. Since any significant disturbance will be reflected by a sudden frequency change, this application scans the streaming frequency measurement data from different locations in real time to look for any abrupt frequency change. Specifically, this FNET/GridEye disturbance detection application calculates the rate of average frequency change df/dt continuously and a disturbance will be considered detected if a pre-defined threshold is exceeded. Once a disturbance is detected, it will be classified into different categories, such as generation loss and load shedding, based on its unique frequency characteristics and then its location will be calculated by use of a geometrical tri-angulation algorithm. This triangulation method basically makes use of the time difference of arrival (TDOA) between different sensors and employs the least square algorithm to estimate the disturbance location. Furthermore, if the disturbance is recognized as a generation loss, the net active power

loss ΔP will also be calculated by multiplying the system frequency deviation Δf during the disturbance and the historical coefficient beta value β . The frequency nadir and settling frequency will also be calculated according to the NERC guidelines. These detection and location results will be in reflected FNET/GridEye disturbance report (as shown in Figure 1.9) and sent out via an email to utility operators.

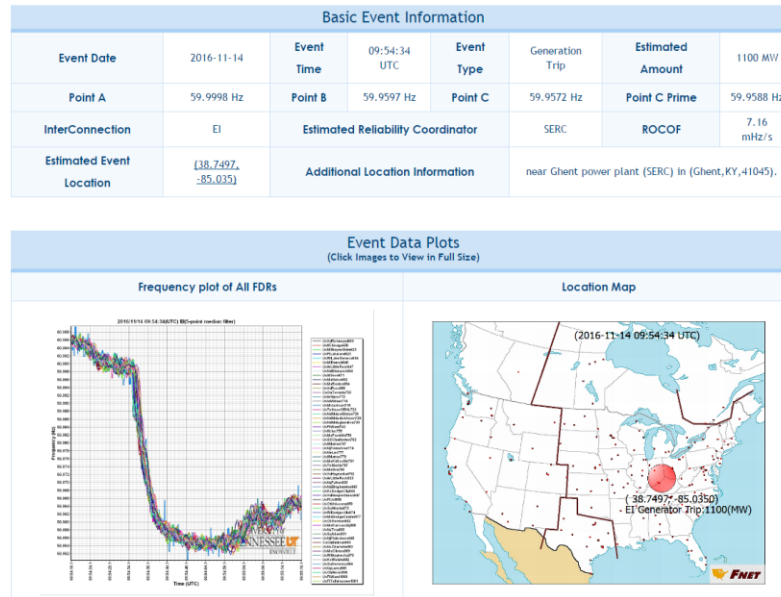


Figure 1.9 Example of the disturbance detection recognition and location report

1.3 Motivation and objective

1.3.1 FDR calibration and sampling control

Each FDR needs calibration before deployment to ensure the acceptable accuracy. Overall, there are three factors that need to be calibrated in sequence: sampling rate, voltage magnitude and angle-shift. The sampling rate calibration is the most critical factor since it is related to the accuracy of the frequency and angle measurement. Voltage magnitude calibration will decrease the deviation of magnitude while the phase angle delay calibration guarantees that the angle delay caused by hardware is compensated.

A manual calibration method has been used in FNET/GridEye for more than 7 years. However, it takes more than two hours to calibrate one unit. Furthermore, the manual method loses accuracy when the frequency of the oscillator drifts due the change of environment temperature and aging.

Therefore, there is a need to establish a faster and more reliable calibration method. We introduce a self-calibration method. This new method can improve both the calibration efficiency and the FDR's measurement accuracy. Additionally, this method does not increase the hardware cost and can easily be implemented in other phasor measurement devices for quick calibration. The comparison of calibration methods is listed in Table 1.1

To calibrate the sampling rate is most challenging in FDR calibration. To resolve this sampling time error, a sampling rate compensation method was used for sampling rate calibration in Frequency Disturbance Recorders (FDRs). All FDRs are manually calibrated before deployment and the sampling time error is effectively resolved. However, since the actual oscillator frequency is unknown, it uses the calculated angle to resolve the sampling time error, which is time-consuming and vulnerable to oscillator frequency drift. To solve this problem, the frequency of the onboard oscillator is monitored in real-time using the PPS timing reference from GPS and a variable sampling interval control method is presented by interlacing two integers under a proposed criterion [17].

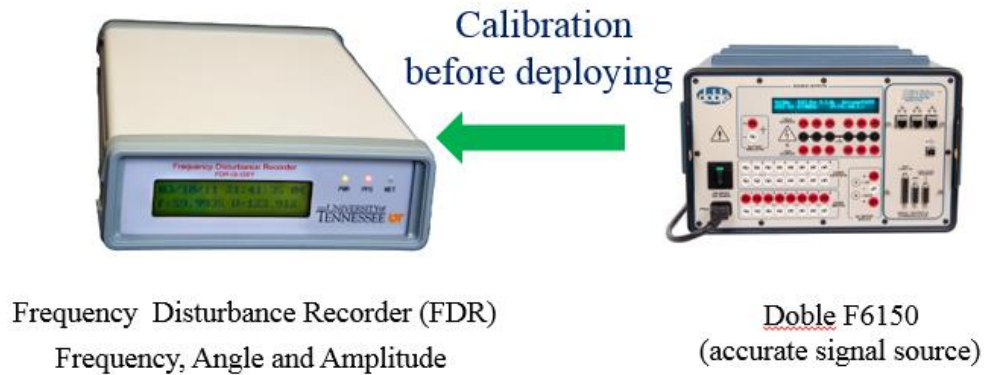


Figure 1.10. FDR calibration

Table 1.1 Comparison of calibration methods

Calibration parameter	Manual calibration	Self-calibration
Sampling rate	Manual (use measured angle)	Self-adaptive sampling (updates every second)
Angle	Manual	One time automatic
Amplitude	Manual	One time automatic

1.3.2 GPS signal loss issues

Since GPS signal is significant in synchronization, one of the critical issues is the reliability of GPS signal. Various uncontrollable and unpredictable factors may cause GPS receivers to lose signal occasionally. This may consequently influence the quality of measurement data [18][19]. Applications in power systems that rely on synchronized measurements that may be vulnerable to GPS signal loss (GSL) include 1) state estimation [21], power system protection[22], [26]2) fault detection[27], and 3) event location [28] etc. As an increasing number of PMU are deployed in power grids, the necessity to evaluate the unavailability and instability of GPS signals among these deployed devices via analysis of real measurement data arises. To study the impact of GSL in PMU, both analysis and experiments are performed. Although in the current stage, the GSL issue in PMU cannot be fully resolved, the impact of GSL can be effectively mitigated to an acceptable level via various methods. Therefore, two typical potential solutions to mitigate the impact of GSL on PMUs are discussed and compared.

1.3.3 Integration with novel sensors

Traditional synchrophasor, usually installed in substations at the transmission level, must be connected physically with a bus or line through potential transformers (PTs) and current transformers (CTs), which requires high manufacturing, installation, and maintenance costs. Furthermore, in some remote areas, far from any substation, it is difficult to install and maintain a synchrophasor due to the lack of facilities. However, high voltage overhead transmission lines are indispensable components of the power grid and abnormal changes of parameters in any part of the transmission network may lead to serious damage or even interruption of power delivery. Per electromagnetic theory, overhead transmission lines generate electric and magnetic fields simultaneously in their right-of-way corridors[24],[25]. The electric fields of overhead power transmission lines are used for non-contact voltage monitoring in Ref.[29]. Since the frequency of these two fields reflects the frequency of the transmission line, it is, then, feasible to obtain frequency characteristic of the transmission line by sensing these two fields. An electric or magnetic sensor can be used to translate the alternating field signal into an alternating current or voltage signal. Thus, an input signal can be obtained without a direct connection. Based on this principle, two types of devices, one using each field type, an electric field sensor based PMU and a magnetic field sensor based PMU are developed.

Moreover, optical sensor technology has proved to be technically mature to the point that they

are preferred over their electronic counterparts in numerous applications across the industry. Compared with conventional transformers, optical sensors have advantages in linearity over dynamic range, seismic performance, noise immunity, increased safety, reduced weight and space, and low installation and maintenance costs [31]. Optical sensors enable a high reliability, wide dynamic range sensor for PMUs. The optical sensor technology is incorporated into PMUs replacing traditional CT and PT for signal acquisition [32].

1.3.4 Development of PMU on mobile platform

Traditional PMUs have several limitations, especially on the conditions of distribution level power grid. First, most of PMUs are installed in substations at the transmission level with three-phase connection, posing high requirements for installation and maintenance. Second, the manufacturing and installation costs of current PMUs are too high. Third, in some remote areas, far from any substation or microgrid operated in either grid connected mode or islanded mode, it is difficult to install and maintain a PMU due to the lack of facilities and high installation cost[9]. Fourth, as most of the current PMU cannot save the measurement data locally, the long distance between the measurement point and the data servers, e.g., phasor concentrator centers (PDCs), will lead to potential threats in data missing due to failure of data communication or cyber-attack [30]. However, it is critical to continually monitor the phasor state in such areas to intercept any potential problem before it reaches the point of no return e.g., a generation trip[33] or islanding process [34].

To overcome the aforementioned issues, one potential solution is to realize the power grid phasor measurement with the integration of a low cost mobile device (MD), e.g., personal smartphone, at single phase distribution level power grid. Current smartphones can achieve high computation speeds to execute real-time measurement algorithm. Implementing the phasor measurement on MDs will facilitate widespread deployment with advantages in the aspects of low cost, data visualization and analytics function, upgrade flexibility and built-in communication channels [35].

1.3.5 ENF application using phasor measurement

The distribution-level electric network frequency (ENF) extracted from an electric power signal is a promising forensic tool for multimedia recording authentication. Local characteristics in ENF

signals recorded in different locations act as environmental signatures, which can be potentially used as a fingerprint for location identification [36].

However, there are significant fundamental questions remaining, prominently: what are the limitations of ENF location identification? Can the ENF signal from a given location be regarded as unique in order to verify the place a recording was taken? The answers to these two questions could potentially pave the way for the usage of ENF-based applications and provide direction for future research for recording authentication[36].

To answer the above question, a new approach which combines both signature extraction and machine learning are proposed. A L-level Daubechies wavelet is used to remove the common component from an ENF signal and a Fourier transform is used to extract the local signatures. To determine the source location of the ENF, a feed-forward artificial neural network (F-ANN) is applied to the extracted signature. These experiments use FNET/GridEye frequency measurements from the EI at multiple geographic scales (500 miles, 200 miles, and 2 miles) to evaluate identification performance. The outcomes of this work are beneficial for authentication of digital multimedia and preventing cyber-attacks on critical infrastructure, e.g., power systems, by detecting if real data have been tampered with or wholly replaced by fake data [36].

1.4 Organization of study

This dissertation is divided into six chapters, each of which discusses a specific aspect of the wide area power grid monitoring.

Chapter 1 has presented background information on the FNET/Grideye system and has explained the motivation behind the work presented in this document. The history and impetus behind FNET and the current generation FDR are discussed. The advances to the state of the art have been outlined, as well as an overview of how the work accomplishes these objectives.

Chapter 2 presents a novel synchronized sampling control method for in PMUs. The sampling control is fundamental for in PMU technology. The proposed method is able to compensate for the sampling time error caused by the division remainder between the desirable sampling rate and the oscillator frequency. Experiments are performed to verify the accuracy of the sampling control method.

Chapter 3 presents the prevalence of GPS signal loss (GSL) on PMU since GPS receivers are likely to lose satellite signals due to various unpredictable factors. The historical GSL events are

extracted from a phasor data concentrator (PDC) and FNET server. The correlation between GSL and time, spatial location, solar activity are explored via comprehensive statistical analysis. Furthermore, the impact of GSL on phasor measurement accuracy has been studied via experiments.

Chapter 4 presents the PMU integrated the novel sensors. First, two innovative designs for wireless PMU, including an electric field sensor based PMU and a magnetic field sensor based PMU are presented. Compared with conventional PMU, wireless PMU is much more flexible to be deployed and have much lower costs. Moreover, to address these nonlinear issue in conventional CT and PT, an optical sensor is used for signal acquisition. This is the first time the successful utilization of an optical sensor in PMUs has ever been reported.

Chapter 5 discusses development of power grid phasor measurement on an Android based mobile device. The mobile device has the advantages of flexibility, easy installation, lower cost, data visualization and built-in communication channels, compared with conventional PMUs.

Chapter 6 presents an application of using electric network frequency for multimedia recording authentication. An ENF identification method combining a wavelet-based signature extraction and feed-forward artificial neural network (F-ANN) based machine learning, is presented to identify the location of unsourced ENF signals without relying on the availability of concurrent ENF signals. Experiments using ENF at multiple geographic scales are performed to validate the effectiveness of the proposed method using ambient frequency measurements. Identification accuracy is presented and the factors that affect identification performance are discussed.

Chapter 2 GPS Signal Based Self-Adaptive Sampling Control for Phasor Measurement

2.1 Background and motivation

PMUs can provide phasor measurements with time stamps utilizing Global Positioning System GPS synchronization technology. According to IEEE standard C37.118.2011, the total vector error (TVE) of phasor measurements should be less than 1% [10], which requires precise time synchronization. Since GPS receiver can provide theoretical synchronization accuracy better than 100 ns via pulse per second (PPS) signals, it is used for waveform sampling in PMUs. PMUs share a uniform time reference PPS output from GPS receivers, essentially enabling all the PMUs across a wide geographical area to synchronize their clocks.

One critical factor of developing synchronized PMUs is PPS-disciplined analog-to-digital converters (ADCs) sampling control. Since sampling of sigma-delta cannot directly be synchronized with the PPS, sigma-delta ADCs are not suitable to synchronous sampling [39]-[41]. To cope with this inherent issue of sigma-delta ADCs, field programmable gate array (FPGA) technology is utilized to realize synchronous sampling control [42]. However, the high manufacturing cost of FPGAs impedes its application within PMUs [43]. Because successive approximation register (SAR) ADC can be directly controlled by a digital signal processor (DSP) while sigma-delta ADC cannot, SAR ADCs are widely used in PMUs for synchronized measurement [20]. The analog to digital conversion is triggered by a PPS each second and the sampling interval between each PPS is controlled by a timer period register (TPR) in the DSP and its connecting oscillator. The value of the TPR represents the number of timer input clock cycles to count

$$N = \frac{f_{osc}}{f_s} \quad (2.1)$$

where N is the number of clock pulses between adjacent samples, f_{osc} is the nominal oscillator frequency, and f_s is the desirable sampling rate.

Ideally the TPR is set to N . However, in practical implementation for DSPs, TPR can only be set as an integer number while N is usually a fractional value. With the limited choice of f_{osc} and integer restriction of TPR, a division remainder inevitably arises, leading to sampling time errors.

For example, if 24 samples per cycle is desirable, the sampling rate f_s (1440Hz) is unlikely to be divisible by f_{osc} (usually 20 or 30 MHz), which leaves a remainder when choosing N [43]. Furthermore, there is an unintended and generally arbitrary frequency drift from f_{osc} for onboard oscillators, caused by various factors which are both uncontrollable and unpredictable (e.g., aging, change of temperature or humidity, etc. [45][46]). Since f_{osc} cannot be considered as a fixed number in real applications as the remainder error will compound over time and erode the accuracy of sampling and the corresponding phasor measurements further. Thus, monitoring the actual performance of f_{osc} is a necessity in hardware implementation.

This sampling error creates inaccuracy in phasor measurement since it accumulates in one second and is cleared by the arrival of PPS. As a result, it causes the phasor angle drift inside each second and a sudden angle change at the end of each second, referred as “saw tooth” shape of phasor angle error.

There are two main options to address this sampling time error. The sampling time error can be corrected by digitally processing the ADC outputs to interpolate the sampling values via oversampling and resampling [47]. The drawbacks of this approach include the additional computation burden and time delay. Alternatively, the sampling intervals could be adjusted to eliminate the sampling error [48][49]. This approach is more effective since it improves the sampling accuracy directly. A proper sampling interval control scheme is the key factor for this approach. Unfortunately, neither of these methods can eliminate the sampling time error without knowing the actual oscillator frequency. To resolve this sampling time error, a sampling rate compensation method was used for sampling rate calibration in Frequency Disturbance Recorders (FDRs). All FDRs are manually calibrated before deployment and the sampling time error is effectively resolved [49]. However, since the actual oscillator frequency is unknown, it uses the calculated angle to resolve the sampling time error, which is time-consuming and vulnerable to oscillator frequency drift.

2.2 Analysis of sampling time error and its impacts

The analysis of sampling time error and its impact on the synchronized measurement unit are discussed in this section. First the ideal GPS-disciplined sampling method is introduced. Second, the sampling-time error, which is likely to occur in PMU implementation, and its impacts on

measurement are discussed. Third, another inevitable issue, on board oscillator frequency drifts, is presented.

2.2.1 GPS-disciplined sampling method

Accurate GPS time information is essential for data synchronization in PMUs. By demodulating the GPS signal, GPS receivers can align their time with UTC and then output a high precision PPS signal for synchronization. Waveform sampling by an SAR ADC in synchronized PMUs is triggered by PPSs as illustrated in Figure 2.1, which ensures that the first sample in each second is aligned to the PPS. From the second sample to the last sample between adjacent PPS signals, the sampling interval is controlled by the oscillator frequency and timer in the DSP. From Figure 2.1, the sampling-interval T , which is equal to the reciprocal of f_s , is a fixed number with the value in TPR held constant. Ideally the time gap T_L between the last sample inside each second and the next PPS signal is equal to T .

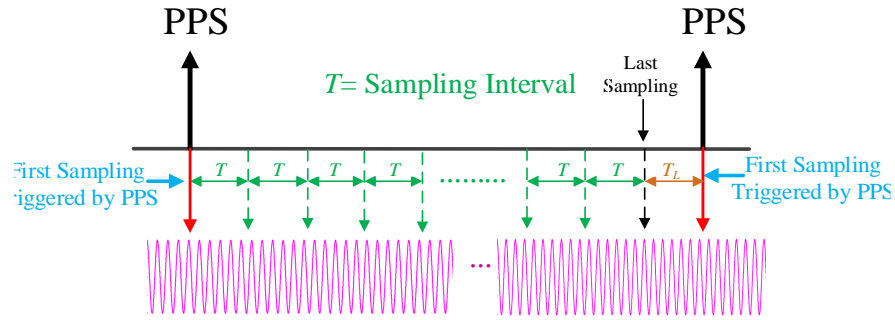


Figure 2.1. The role of the PPS signal in waveform sampling

2.2.2 Sampling-time error

In hardware applications, a timer counter register (TCR) is used to count the clock pulses and trigger an interrupt to send a sampling command when the value in the TPR is reached. The interrupt provides timing information to control each sampling interval. In (2.1), when f_{osc} is not evenly divisible by f_s , the fractional part FP of N can be expressed as

$$FP = N - \text{Floor}(N) \quad (2.2)$$

where $\text{Floor}(\cdot)$ is a function that rounds the input value down to the nearest integer smaller than N .

Due to the integer constraint of TPR, it cannot be set to a fractional N . Assuming N_L and N_H are the nearest integers satisfying $N_L = \text{Floor}(N)$ and $N_L + 1 = N_H$, TPR can be practically set as either N_L or N_H . A remainder and consequent sampling time error arises whether N_L or N_H is selected. This situation is likely to arise in real applications. For example, a sampling interval set to 2 ms by the DSP may actually be 1.9 or 2.1 ms due to integer constraints. Such inaccurate sampling intervals will result in instantaneous sampling time errors, which will accumulate over time. The sampling time error for one sampling point is

$$t_{error} = \frac{1}{f_s} - \text{Floor}\left(\frac{f_{osc}}{f_s}\right) \times \frac{1}{f_{osc}} \quad (2.3)$$

The angle measurement error caused by this error is

$$\varepsilon_a = 360^\circ \times t_{error} \times f_0 \quad (2.4)$$

where f_0 is the power grid frequency.

Assuming the nominal frequency of the crystal oscillator is 200 MHz and $f_s = 1440$ Hz, the time error is $0.44 \mu\text{s}$ and the corresponding angle error for one sampling point is $1.31 \times 10^{-3}^\circ$ assuming 60 Hz power grid frequency. Although these errors are seemingly negligible, they will accumulate over each full second, resulting in a cumulative $644 \mu\text{s}$ time error and 1.88° angle error.

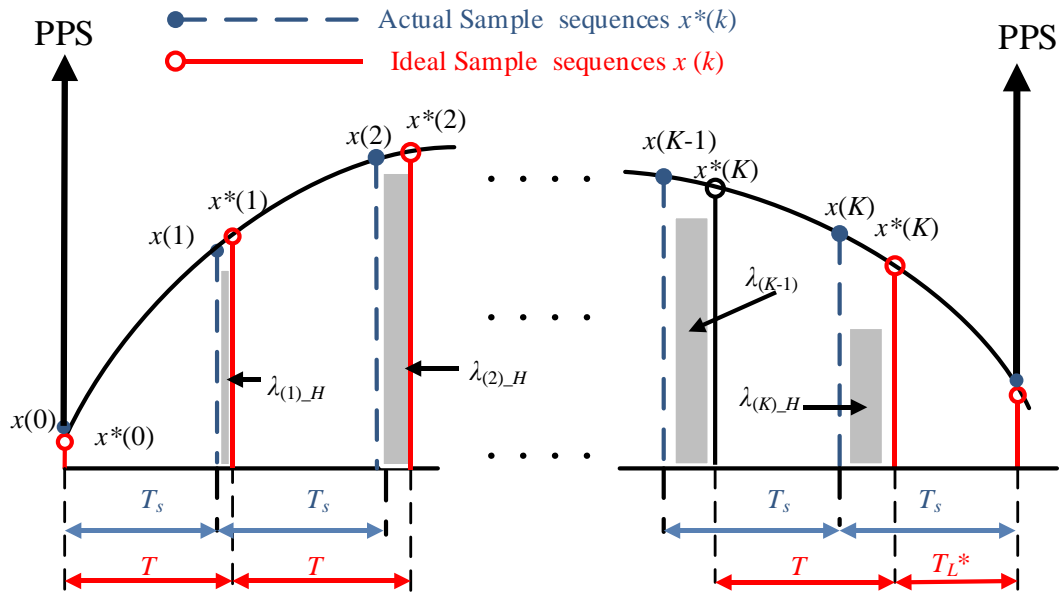


Figure 2.2. Schematic diagram of the sampling error for GPS-disciplined sample process

As frequency can be defined as the derivation of angle [50], a sequence of phase angles is usually used to calculate the rate change of angle and frequency. The frequency error can be expressed as

$$\varepsilon_f = \frac{d(\varepsilon_a(t))}{dt} \quad (2.5)$$

From (2.5), linear drift of angle error will lead to a DC-offset of frequency measurement.

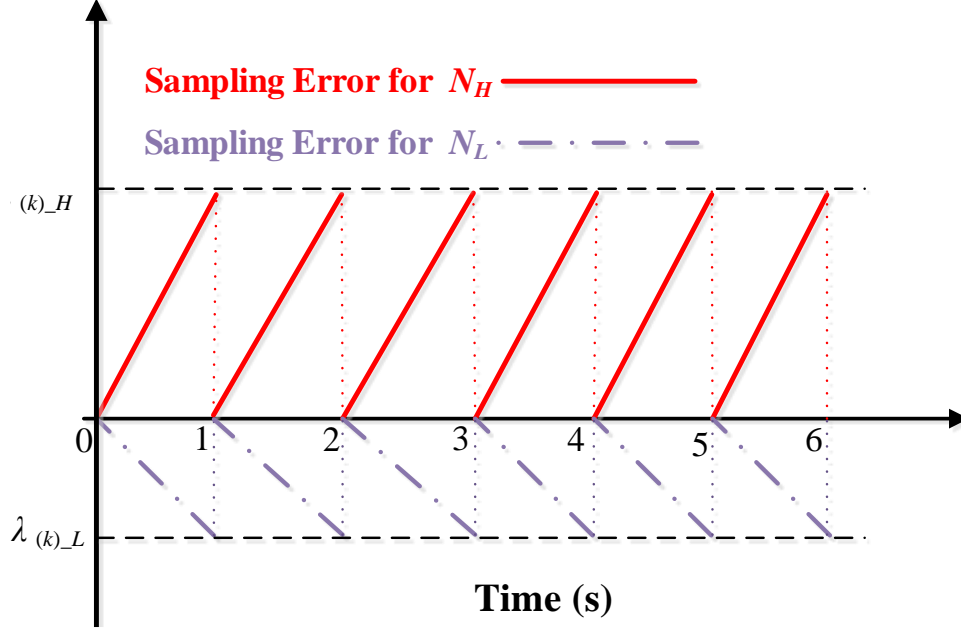


Figure 2.3. Sampling time error for N_L and N_H

Assuming TPR is set as N_H for sampling interval control, a typical GPS-disciplined sample process is shown in Figure 2.2, where $x(k)$ and $x^*(k)$ denote the ideal sampling sequence with N and practical sampling sequence with N_H . K is the number of sampling points in one second. $x(0)$ and $x^*(0)$ represent the first point triggered by the PPS at the begin of each second, which are overlapped with each other. Because f_{osc} is not an integral multiple of the f_s , the actual sampling interval T_s is not equal to the desirable sampling interval T , that is, $\lambda_{(1)_H} = T - T_s \neq 0$ where $\lambda_{(1)_H}$ is the sampling error for the second sampling point. The sampling error accumulates each point at a same speed, satisfying the following equation

$$\lambda_{(k)_H} = k \times \lambda_{(1)_H} \quad (2.6)$$

where k represent the index of the sampling points. T_L^* is the time interval between the last

sampling point in the previous second and the next PPS. The sampling time error is finally accumulated to T_L^* since PPS signals trigger the first sampling each second and clear the error. Similarly, if N_L is selected for TPR, a similar sampling time error occurs with an opposite drift direction, which is illustrated in Figure 2.3.

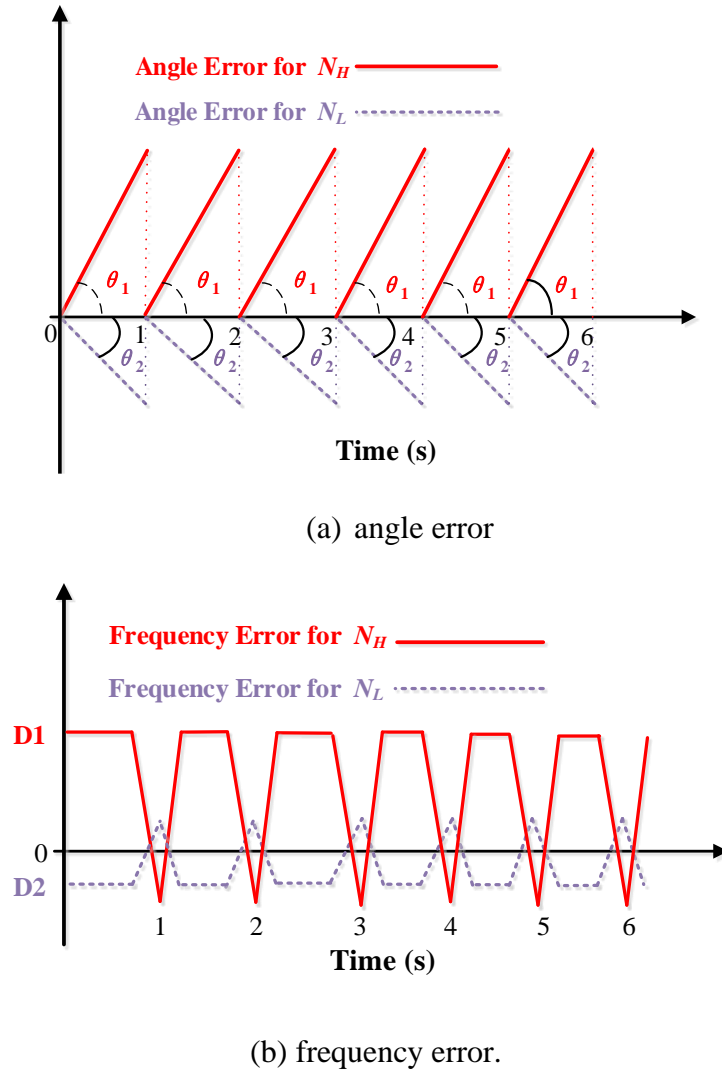


Figure 2.4. Frequency and angle error caused by sampling time error

Figure 2.4 shows the error of frequency and angle caused by sample time error in Fig.2. 3. It can be seen from Figure 2.4 (a) that the angle errors for N_L and N_H drift in opposite directions with slope angle θ_1 and θ_2 , respectively. As a significant time gap exists at the connection of two adjacent seconds, a sudden change in measurement angle is seen. According to frequency estimation algorithm [50], linear angle drift θ_1 and θ_2 in Figure 2.4 (a) will cause constant DC-

offsets D1 and D2 in frequency measurement error in Figure 2.4 (b). It is assumed frequency is constant within the computation windows, thus the value of phase angles should be continuous . Therefore, when the sudden angle change at the end of each second is included in the sliding window of phase angle sequences for frequency calculation, irregular frequency spike will be caused by this phase angle discontinuity. The width of the spike is equal to the window length of the phase angles sequences. These abnormalities in both angle and frequency measurements may trigger false detection of a power system event or protection action in some measurement based power grid applications [51].

2.2.3 Oscillator frequency drift

Because of their accessibility and low cost, quartz-based crystals are used as the timing source in most measurement devices. However, f_{osc} is likely to drift from its nominal value at the level of 30 PPM (part per million) due to changes in temperature that alter the piezoelectric effect, problems with voltage regulators which control the bias voltage to the oscillator, component aging, etc. For example, shifts in temperature can increase frequency drift by tens of PPM even within the standard temperature range. As a result, the drift of f_{osc} will affect the sample interval control and introduce the division remainder. For example, assuming that the desirable sampling rate is 1440 Hz and the nominal oscillator frequency is 32.256 MHz, then (1) results in an ideal with no remainder for this hardware configuration. However, if f_{osc} drift is considered, the sampling time error appears again. Figure 2.5 shows sampling time error with positive 1 PPM, 10 PPM, and 50 PPM f_{osc} drift. The time error exceeds $0.5 \mu s$ for these three conditions, which will cause at least $1.62 \times 10^{-3}^\circ$ phasor angle error.

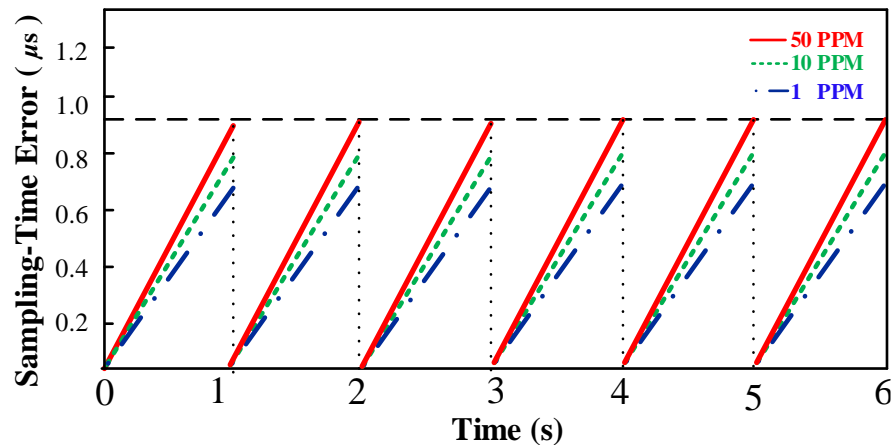


Figure 2.5. Sampling time error caused by oscillator frequency drift

2.3 Proposed sampling method

In this section, a method is introduced to compensate the sampling time error. Since TPR must be set as an integer number while the actual N is a fractional number, N_L and N_H are alternately selected to approach the true N , based on a proposed criterion. The sampling intervals are varied between the two values to compensate for the sampling time error. In order to fully compensate for the error, oscillator frequency f_{osc} is monitored in real-time using the PPS reference each second.

2.3.1 Variable sampling interval control

For a conventional sampling interval control, the time interval for each sample point is fixed. FP can be expressed by θ_1 and θ_2 in Figure 2.4.

$$FP = \frac{|\theta_1|}{|\theta_1| + |\theta_2|} \quad (2.7)$$

Assuming $FP = 0.5$, then $|\theta_1| = |\theta_2|$. Since the slope of the drift speeds have different signs but the same magnitudes, the sampling time error can be compensated for by evenly alternating between N_L and N_H for TPR when $FP = 0.5$, as illustrated in Figure 2.6.

Based on this idea, the variable sampling interval can be achieved by the interval selection of N_L and N_H . To compensate the sampling time error, the ratio R of the selection N_L and N_H should be set as

$$R = \frac{FP}{1 - FP} \quad (2.8)$$

Sometimes R cannot be exactly achieved with a limited number of sampling points. For each sample inside a single second period, either N_L or N_H is selected to control the sampling intervals based on the following criterion:

$$N_k = \begin{cases} N_L & \left(\text{IF } \frac{v_k}{k} \geq FP \right) \\ N_H & \left(\text{IF } \frac{v_k}{k} < FP \right) \end{cases} \quad (2.9)$$

where FP is the unique parameter that determines the ratio of N_L and N_H . v_k is a control variable that counts the number of periods where N_H has been selected, which can be expressed as

$$v_k = \begin{cases} v_k = v_{k-1} + 1 & \text{when } N_H \text{ is selected} \\ v_k = v_{k-1} & \text{when } N_L \text{ is selected} \\ v_k = 0 & \text{when } k = 0 \end{cases} \quad (2.10)$$

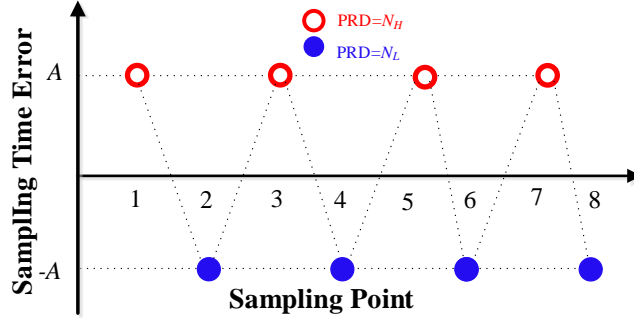


Figure 2.6. Variable sample interval control with FP=0.5

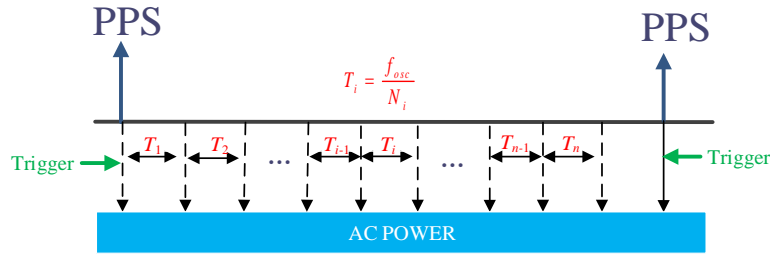


Figure 2.7. Variable sampling interval control strategy

N_L and N_H are selected proportionally according to (2.9) and (2.10). This two-value variable sampling interval control is able to compensate most of the sampling time error. It should be noted that to optimally balance time error between N_L and N_H , the use of both N_L and N_H is distributed across each second based on the criterion as illustrated Figure 2.7. The actual overall ratio R_a of the selection N_L and N_H can be expressed using formula (2.11). With a large K for high sample rate, R_a converges toward R . Thus, this proposed method has advantages for high sampling rate conditions.

$$R_a = \frac{v_K}{K - v_K} \quad (2.11)$$

2.3.2 Oscillator frequency monitor

From the previous analysis, FP can be obtained from (2.1) and (2.2). Ideally, the oscillator frequency f_{osc} equals its nominal value and FP is a constant. Unfortunately, in real application, the

frequency of f_{osc} tends to drift, which may consequently impair the accuracy of sampling interval control. Since there is a gap between f_{osc} and its nominal value, it would be helpful to monitor the real performance of f_{osc} and update FP for sampling control. The importance and idea of oscillator frequency monitoring in synchronized measurement devices was first proposed for use in the universal grid analyzer (UGA). As a PPS signal can achieve an accuracy of 100 ns with stable acquisition of GPS signals, it can be used as a time reference to monitor the onboard oscillator frequency.

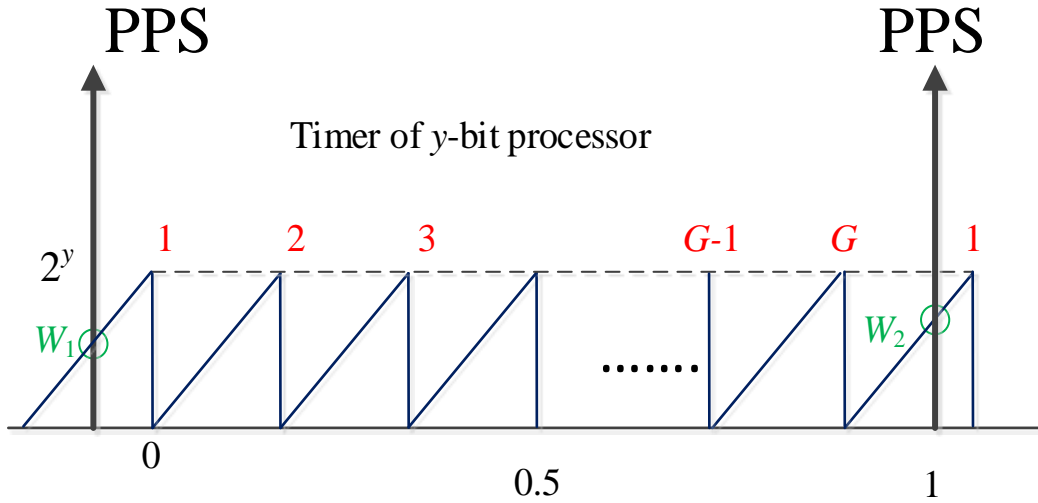


Figure 2.8. Monitoring of oscillator frequency

Assuming that a y-bit DSP and onboard oscillator with f_{osc} , a timer can be triggered by rising edges of PPS signal to count the number of cycles from an oscillator between two consecutive PPS signals, which is illustrated in Figure 2.8.

The maximum length of the timer is

$$t_{max} = 2^y / f_{os} \quad (2.12)$$

When t_{max} is less than 1 s, the timer must run continuously, configured to automatic reset and restart mode. The measured actual oscillator frequency can be expressed as

$$f_{osc} = 2^y \times G - W_1 + W_2 \quad (2.13)$$

where G is the number of times the timer restarts between two adjacent PPS signals. W_1 and W_2 are the values of the timer counter register at the arrival of adjacent PPSs, respectively. f_{osc} can be measured and updated every second in real time, thus eliminating (or greatly reducing) the adverse impact of oscillator frequency drift.

Rectified sampling intervals control parameters $N'_{(i)}$ and FP' can then be calculated via the following formulas

$$N'_{(i)} = \frac{f_{osc(ti)}}{f_s} \quad (2.14)$$

$$FP'_{(i)} = N'_{(i)} - \text{floor}(N'_{(i)}) \quad (2.15)$$

where i denotes the integer time index of the current second.

2.3.3 Complete process for the proposed sampling method

By using the sampling method discussed above, the sampling time error can be resolved effectively. The flowchart of the proposed method for SAR ADC sampling control is presented in Figure 2.9. First, f_{osc} is monitored under a PPS time reference. The interrupt triggered by the PPS is used to issue the first sampling command of each second and to monitor f_{osc} . The FP for the ideal value of N is obtained in the second step. Variable sampling interval control is conducted to compensate sampling time error. No extra hardware is added to the proposed method. The entire process is straightforward and effective without high complexity calculations, thus the computation burden of the sample method is low and negligible compared with typical phasor measurement algorithms in terms of accumulation and multiplication, which is easy to implement in hardware. The new sampling method can be outlined in the following steps.

Step 1: Obtain the actual oscillator frequency, f_{osc} from (2.13).

Step 2: Calculate FP for the ideal value of N from (2.14) and (2.15)

Step 3: Initiate the first sampling, triggered by PPS interrupt.

Step 4: Determine the selection of N_L or N_H for sampling interval control based on the criterion in (2.9).

Step 5: Update v_k using (2.10), return to Step 4 to complete all the samples inside a one second period.

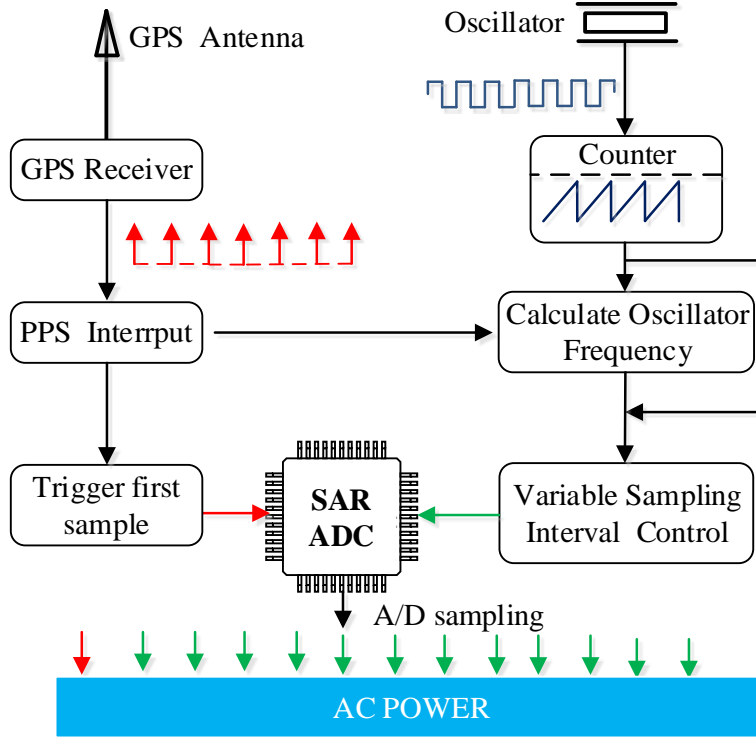


Figure 2.9. Flowchart of the proposed method

2.4 Simulation and implementation result

The aim of this section is to validate the proposed method by means of simulation and real implementation.

2.4.1 Simulation

To demonstrate the effectiveness of the proposed method, simulations are performed in MATLAB[®]. The desired sampling rate and oscillator frequency are 1440 Hz and 32.11 MHz, respectively. The window length of phase angle for frequency calculation is 144 to balance the tradeoff between the accuracy and speed. From equation (2.1), the ideal sampling interval N is 22298.61111. As N is a fractional number, N_L and N_H are 22298 and 22299 respectively. By applying the proposed method, the selection of the first 65 N_k in a one second period is shown in Figure 2.10. N_L and N_H are alternatively selected at a ratio $R_a \approx 3$. To evaluate the performance of the variable sampling method, a parameter $TPR_{(k)}$ that reflects the average TPR for k sampling points is defined as

$$TPR_{(k)} = \frac{v_k \times N_L + (k - v_k) \times N_H}{k} \quad (2.16)$$

All $TPR_{(k)}$ in the one second period are illustrated in Figure 2.11. By using this variable sampling scheme, the $TPR_{(k)}$ approaches the ideal N within a short time. Figure 2.12 shows the comparison of sampling time error for the fixed and variable sampling methods in a five second. The drifting errors nearly reach $27 \mu s$ and $-18 \mu s$ from fixed use of N_H and N_L , respectively, where it is removed using the variable sampling method.

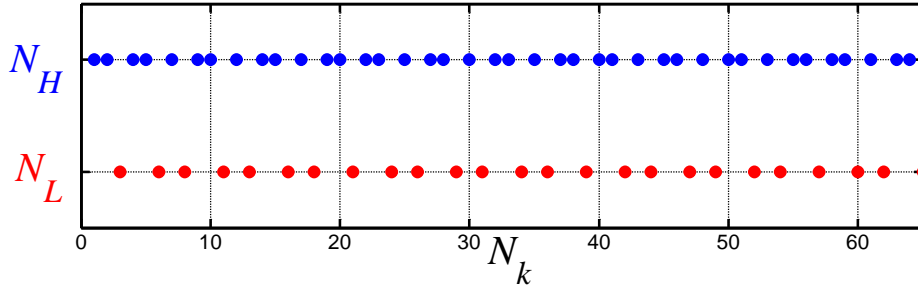


Figure 2.10. Selection of N_k

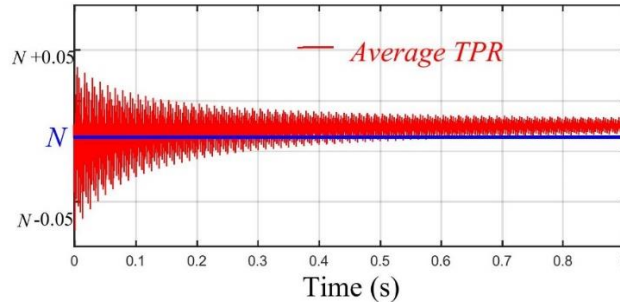


Figure 2.11. Average TPR in a one second period

Figure 2.13 shows the comparisons of angle and frequency measurement for these methods. The frequency of the ideal sinusoidal input signal is 60 Hz and the initial angle is 0° . As can be seen from Figure 2.13 (a), the angle error of the two fixed sampling methods drift with opposite directions, whereas the angle error of the variable sampling method is greatly reduced. The new method eliminates the noticeable “saw-tooth” waveform and the error no longer accumulates over time. There is obvious DC offset and spikes in frequency measurement for the fixed sampling intervals, illustrated in Figure 2.13 (b), caused by angle drift and sudden changes, respectively. As

the sampling time error has been effectively compensated by the new method, frequency and angle error curve of the proposed method presents a straight line without fluctuation.

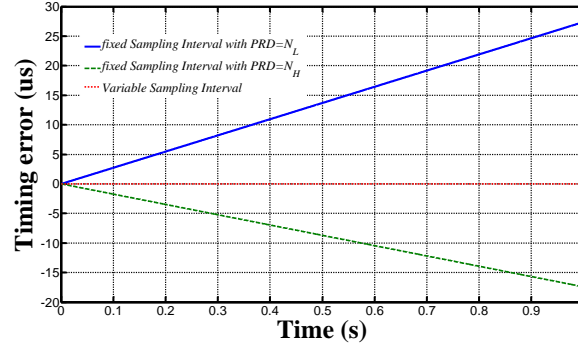


Figure 2.12. Sampling time error comparison

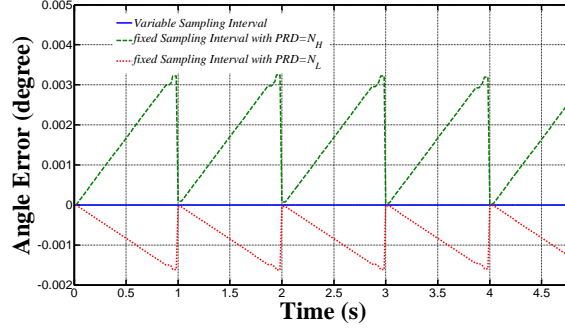
The comparison of frequency and angle error are also listed in Table 2.1. The accuracy of the variable sampling interval method is obviously improved with respect to both angle and frequency error.

It should be noted that the drift of f_{osc} is considered in this simulation. Due to the f_{osc} drift, sampling time error could not be completely compensated without f_{osc} monitoring and error is in the order of 10^{-4} for both angle and frequency. With f_{osc} monitoring and adaptive adjustment, the angle error is reduced from $1.9 \times 10^{-3}^\circ$ to $8.5 \times 10^{-5}^\circ$ and the frequency error is reduced from 1.5×10^{-3} Hz to 9.2×10^{-5} Hz for 1 PPM drift.

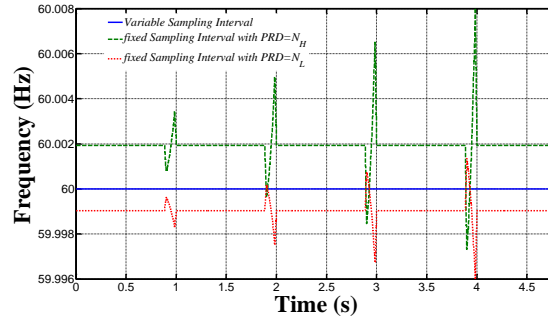
Nevertheless, there are some practical issues that need to be looked into. Since the resolution of oscillator frequency measurement is the reciprocal of f_{osc} and the measurement time is one second, the f_{osc} drift is not known if the drift value is less than the reciprocal of f_{osc} or the drift duration is less than one second. Also adaptive adjustment of sampling control has maximum one second time delay after the f_{osc} is drifted.

Table 2.1 Result summary and comparison

Error	Fixed Interval		Variable Interval		
	N_H	N_L	1PPM	10PPM	f_{osc} monitor
Angle ($^\circ$)	1.18×10^{-3}	3.12×10^{-3}	1.9×10^{-4}	3.9×10^{-4}	8.5×10^{-5}
Freq. (Hz)	2.48×10^{-3}	3.18×10^{-3}	1.5×10^{-4}	3.5×10^{-4}	9.2×10^{-5}



(a) plot of angle results



(b) plot of frequency results.

Figure 2.13. Comparison of angle and frequency results

2.4.2 Laboratory experiment

To examine and verify the proposed method, experiments were performed in the Power Information Technology Laboratory at the University of Tennessee, Knoxville. The experiment settings are shown in Figure 2.14. The methods are implemented FDRs [13], a single-phase variant of PMUs, with input signals from a Doble F6150 Power System Simulator. These results can be generalized to all other PMUs which rely on PPS signals for synchronization. The Doble power source generates an ideal sinusoidal 120V/60Hz signal, which acts as an accurate and reliable reference for this evaluation. The initial angle is 0° at each PPS. The output signal from Doble is fed into FDRs directly. The frequency, angle, and amplitude measurement results are extracted from the network TCP/IP data package, time-aligned, and then transmitted to and stored in the FNET/GridEye server at outputting rate 10 Hz. All the FDRs measurement results can be compared with Doble output for accuracy evaluation since both the Doble and FDRs obtain stable GPS signals throughout the test.

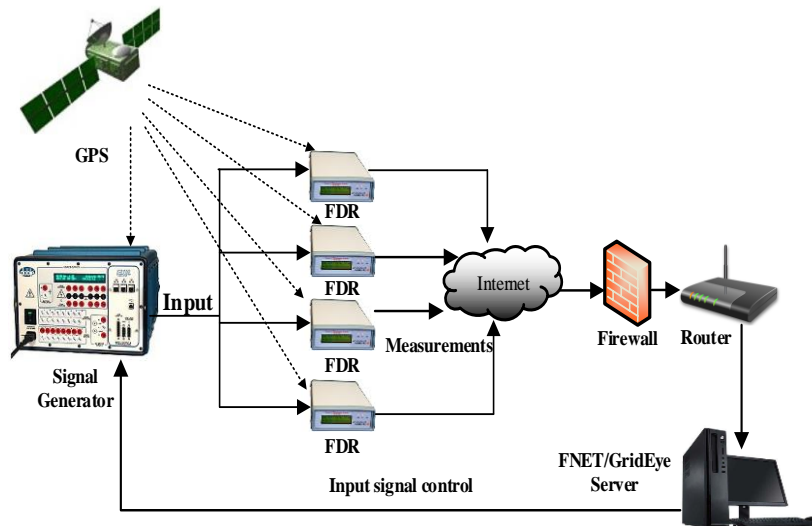


Figure 2.14. Experiment settings

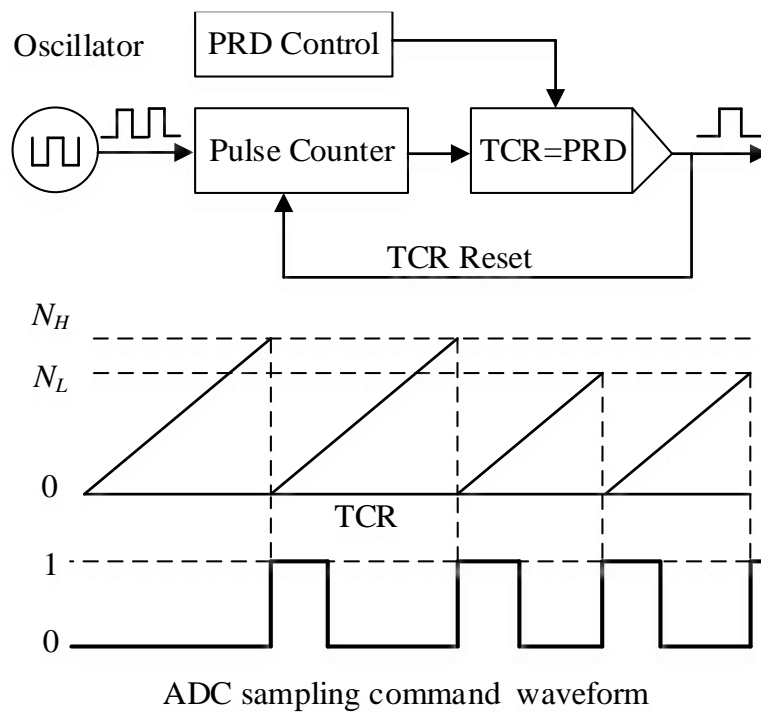
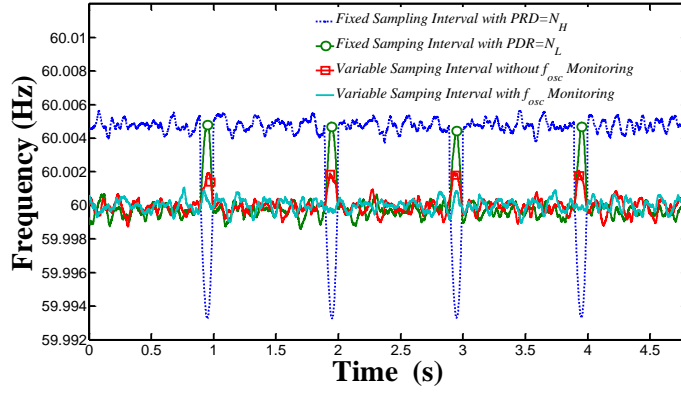
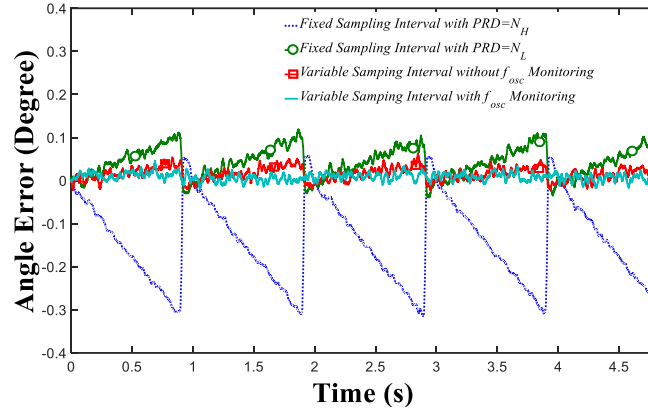


Figure 2.15. Illustration of SAR ADC control



(a) Plot of angle results



(b) Plot of frequency result

Figure 2.16. Comparison of angle and frequency results

In this experiment, the SAR ADC is 14-bit AD7865 with a desired sampling rate of 1440 Hz and the DSP is a TMS320LF2407 with a nominal f_{osc} of 30 MHz. According to (2.1), N is 20833.333. N_L and N_H are 20833 and 20834, respectively. The ADC and the DSP use serial peripheral interface (SPI) for data communications. Each conversion is initiated by the DSP. The sampling interval is controlled by the interval timer in DSP. The ADC control is illustrated in Figure 2.15. The criterion to set the TPR between the selection of N_H and N_L is based on formulas (2.9) and (2.10). Once TCR reaches the value of TPR, it automatically resets to zero and immediately generates high-level voltage for the rectangle waveform. The rising edge of the waveform will trigger the ADC sampling.

Four FDRs are each loaded with a different firmware options: the conventional fixed sampling interval method with $TPR = N_L$, the fixed sampling interval method with $TPR = N_H$, the variable sampling interval method without f_{osc} monitoring, and variable interval method with f_{osc} monitoring. In order to obtain a fair comparison of sampling accuracy, the same typical DFT based phasor measurement algorithm is used in these four FDRs.

Motorola M12+ GPS receiver is used in FDRs to generate PPS signals as timing reference for synchronization. For the real time f_{osc} monitoring, due to hardware errors there is a small time delay for all FDRs that needs to be compensated for in real implementation. For the devices with the same hardware configuration, the time delay can be considered as a constant number. Thus this constant delay parameter D is subtracted for f_{osc} measurement

$$f_{osc} = 2^y \times G - W_1 + W_2 - D \quad (2.17)$$

Angle and frequency errors for a five-second window are plotted in Figure 2.16. The fluctuation of the angle and frequency measurements is inevitably caused by the hardware resolution limitation, white noise, etc. There is an obvious “saw tooth” component in the angle error of the fixed methods which is effectively eliminated using the variable methods. This is a clear demonstration of the validity of the proposed method. From Figure 2.16(b), the DC offset and large frequency spikes are both removed using the proposed methods. It should be noted that there is a small spike for the variable method without f_{osc} monitoring whereas the frequency for the method with f_{osc} monitoring is smoother. These results prove the efficacy of the proposed method for reducing frequency and angle error.

Table 2.2 Result summary for laboratory experiment

Error	Fixed Interval		Variable Interval	
	N_H	N_L	without f_{osc} monitor	with f_{osc} monitor
Angle (°)	3.93×10^{-1}	1.24×10^{-1}	5.71×10^{-2}	3.25×10^{-3}
Freq. (Hz)	5.24×10^{-3}	6.1×10^{-3}	2.13×10^{-3}	1.15×10^{-3}

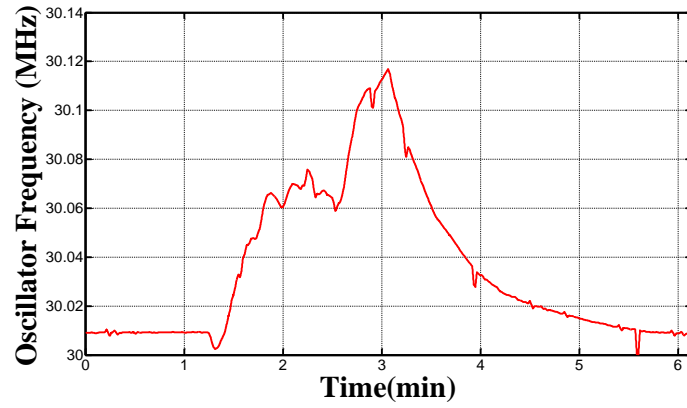
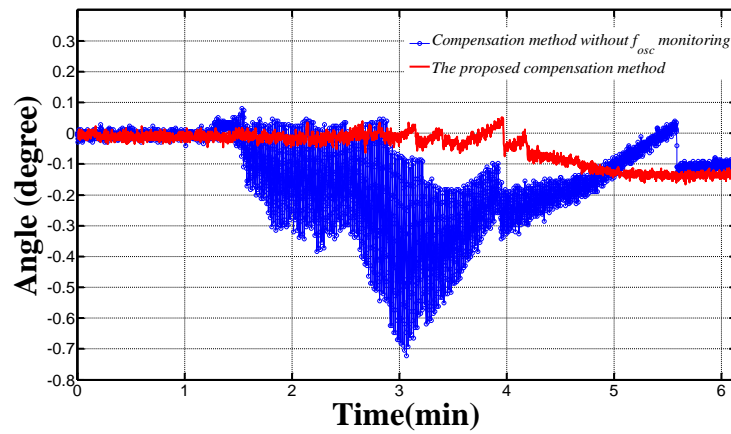
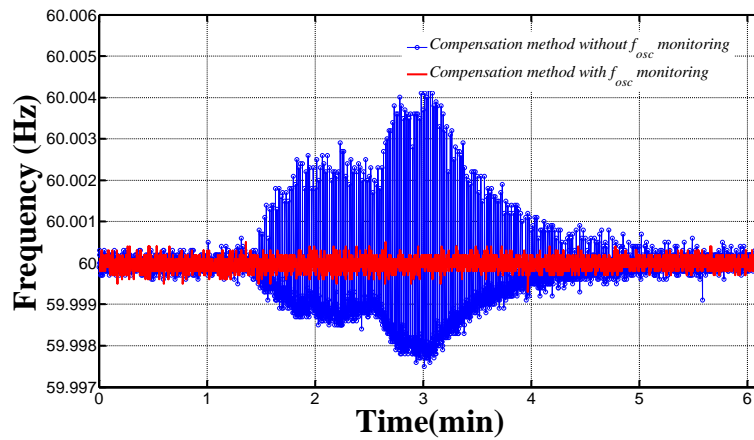


Figure 2.17. The curve of oscillator frequency drift



(a) Plot of angle results



(b) Plot of frequency result

Figure 2.18. Comparison of angle and frequency results

From Table 2.2, the variable sampling interval method significantly reduces both frequency and angle measurement errors. It can be seen that experiment result errors are 3.25×10^{-3} Hz for frequency and $1.15 \times 10^{-3^\circ}$ for angle, which are larger than the simulation result with 0.12×10^{-3} Hz and $0.15 \times 10^{-3^\circ}$. This can be explained by the hardware resolution limit and GPS signal accuracy because the actual PPS pulse only has an accuracy of up to 100 ns, which is equivalent to $2.2 \times 10^{-3^\circ}$ for 60 Hz power systems. The TVE (total vector error) in this laboratory experiment, as small as about 0.324% after implementing this adaptive variable sampling method, sufficiently complies with IEEE standard C37.118, which stipulates that TVE should be less than 1%. It evinces the efficacy of the proposed methods in terms of reducing sampling time error and improving the synchrophasor measurement accuracy.

To further investigate the advantage of f_{osc} monitoring, the proposed method is compared to the compensation method without f_{osc} monitoring. The f_{osc} starts to drift at 1.2 minutes as shown in Figure 2.17, which is caused by the variation of environmental temperature. According to the results shown in Figure 2.18, the drift of f_{osc} results in an 0.6° angle error and 10 mHz frequency error without f_{osc} monitoring while the impact of the f_{osc} drift on measurement accuracy of the proposed method is much smaller. It demonstrates that oscillator frequency drift will no longer adversely affect sampling accuracy for the new method.

As a practical issue, it needs to be mentioned that since the proposed method highly relies on high precision PPS from the GPS receiver as sampling triggering and timing reference for the on board oscillator frequency monitoring, the accuracy of phasor measurement will be reduced when acquisition of GPS signals is unstable or even lost due to uncontrollable and unpredictable factors in actual operation [52].

2.5 Conclusion

In this chapter, a PPS-disciplined synchronous sampling method is presented to control the SAR ADC, which results in better accuracy for real implementation of PMUs. The proposed method mainly includes two aspects:

- 1) To compensate the inevitable sampling time error caused by the remainder between sampling rate and oscillator frequency, a variable sampling interval control method is achieved by the alternate use of the two nearest integers based on the proposed criterion.
- 2) To cope with oscillator frequency drift, oscillator frequency is monitored in real time using

a PPS timing reference from GPS signal receivers. The sampling control is adaptively adjusted since the oscillator frequency is updated every second.

By applying this new method, the “saw tooth” angle error is eliminated. The DC offset and spikes in frequency error are also effectively removed. As oscillator frequency is monitored under the PPS reference and is updated each second, drift in oscillator frequency will not affect the accuracy of sampling control and phasor measurement. Thus, the sampling time error can be fully compensated. The computation burden of the proposed method is low and no extra hardware is added, making it easy for hardware implementation in real time. The simulations prove the effectiveness of the proposed methods at removing sampling time error and improving both angle and frequency measurement accuracy and laboratory testing explicitly demonstrates the satisfactory performance of the proposed methods in real PMU implementation.

Acknowledgment

This chapter is, in part, a reprint of the material in the paper: Wenxuan Yao, Lingwei Zhan, Yong Liu, Micah Till, Jiecheng Zhao, Ling Wu, Zhaosheng Teng, Yilu Liu, “A Novel Method for Phasor Measurement Unit Sampling Time Error Compensation”, IEEE Transactions on Smart Grid, vol. 9, no. 2, pp. 1063-1072, March

Chapter 3 Impact of GPS Signal Loss and Its Mitigation on Phasor Measurement Units

3.1 Background and motivation

By demodulating the GPS satellite signal, a GPS receiver can align its local time with UTC and then generate an ultra-high precision timing signal, e.g. PPS signal with theoretical 100 nanosecond accuracy. Each individual PMU unitizes the timing signal from the GPS receiver as a time reference to trigger the waveform sampling, which ensures the first sample in each second is aligned to the PPS for all the PMUs in different locations. To address data transmission delays from PMUs to the phasor data concentrators (PDCs) via the communication network, the phasor measurement data, typically calculated in a digital signal processor, are stamped with UTC time index before transmitted to a phasor data concentrator (PDC) as illustrated in Figure 3.1.

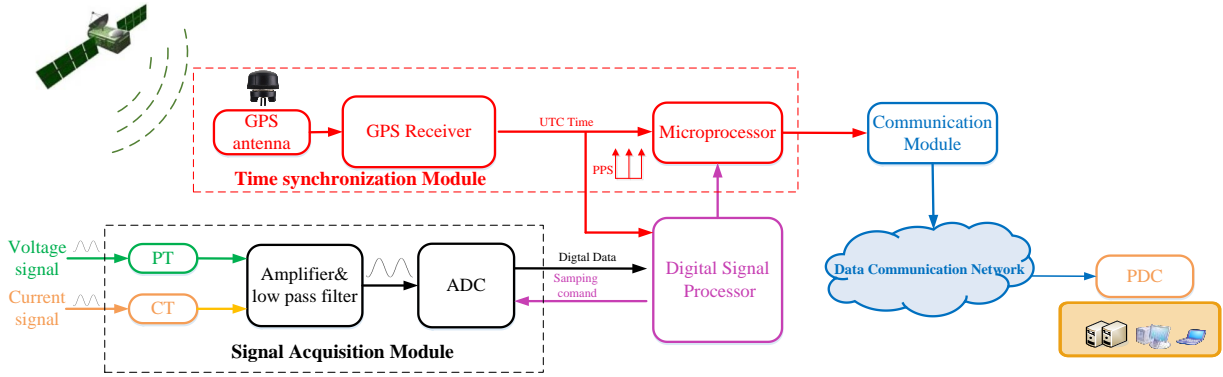


Figure 3.1. Illustration of PMU with GPS time synchronization

According to IEEE standard C37.118.2011, the total vector error (TVE) of phasor measurements should be less than 1%, which requires precise time synchronization such as that provided by GPS. A phase angle error of 0.01 radian will cause 1% TVE. Thus the minimum requirement for the time reference accuracy is $26 \mu\text{s}$ for a 60 Hz system and $\pm 31 \mu\text{s}$ for a 50 Hz system.

One of the critical issues for SMDs is the reliability of GPS signal. Various uncontrollable and unpredictable factors (e.g., atmospheric disturbances, failure of the GPS antenna, electromagnetic interference, weather change, GPS signal attack, or solar activity [19][53]) may cause GPS receivers to lose signal occasionally, even if their antennas are placed in a location with an unobstructed view of the satellites. This may consequently influence the quality of measurement data .

In IEEE standard C37.118.2 on synchrophasor data transfer for power systems, a flag in the data output is provided to indicate a loss of time synchronization and shall be set to “1” when loss of synchronization could cause the TVE to exceed the limit or within one minute of actual loss of synchronization .

As an increasing number of SMDs are deployed in power grids, the necessity to evaluate the unavailability and instability of GPS signals among these deployed devices via analysis of real measurement data arises. This chapter conducts an analysis on the historical data from phasor data concentrators (PDCs) and FNET/GridEye servers for the years 2008 to 2015 to find the presence of GSL in SMDs. To study the impact of GSL in SMDs, both analysis and experiments are performed. From the analysis and test results, the timing error caused by GSL introduces a significant angle drift and consequently leads to TVE exceeding IEEE standard. Although in the current stage, the GSL issue in PMU cannot be fully resolved, the impact of GSL can be effectively mitigated to an acceptable level via various methods. Therefore, two typical potential solutions to mitigate the impact of GSL on PMUs are discussed and compared.

3.2 Methodology for GSL prevalence analysis

To investigate GSL issues in PMUs, comprehensive statistical analysis on historical PMU data from PDCs and FNET/GridEye server (from Jan. 2010 to Dec. 2012) is performed. The PMU data are collocated from hundreds of commercial PMUs at 30Hz reporting rate in a PDC. According to the IEEE synchrophasor Data transfer standard C37.118.2, the availability information for GPS synchronization can be indicated by the 13th bit of the 'STAT' flag. '1' means with GPS synchronization whereas '0' means without GPS synchronization. This bit can be scanned to locate the GSL event and calculate the duration of each GSL event. GSL events at the different time period and locations are categorized for time and spatial analysis. Furthermore, the historical 10.7cm radio flux data [54] are loaded to explore the correlation between solar activity and GSL as illustrated in Figure 3.2.

Unlike typical PMU transfer format, the data frame of FNET/GridEye does not include STAT but record the strength of GPS signal[55]. To be more specific, an FDR updates the number of locked GPS satellites in their data frames to reflect the GPS signal strength (GSS). A GPS receiver can lock 4 to 12 satellites with a good GPS signal reception. When the number of satellites is “0”, it indicates that the FDR begins to lose GPS synchronization. Taking advantage of wide

deployed FDRs, the GSL issue can be investigated by loading historical data from FNET/GridEye Sever with more information of GSS compared with commercial PMUs. Furthermore, the daily pattern of GSS can be explored via processing the number of locked satellites (NLS) in FDR data frame [56].

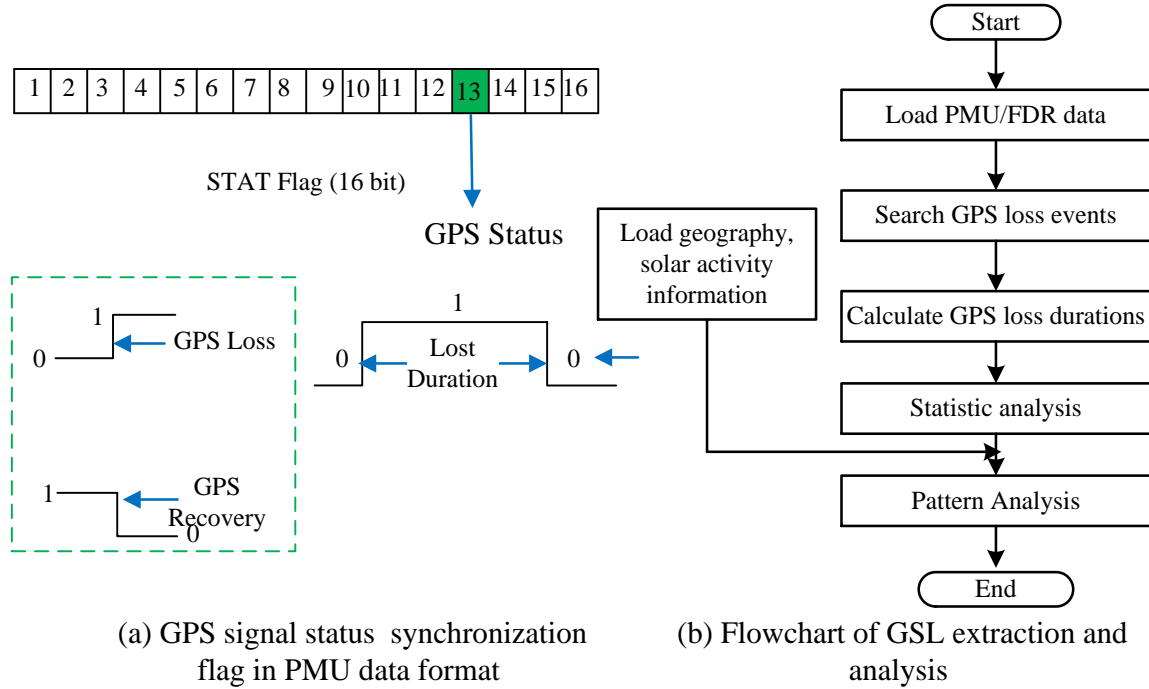
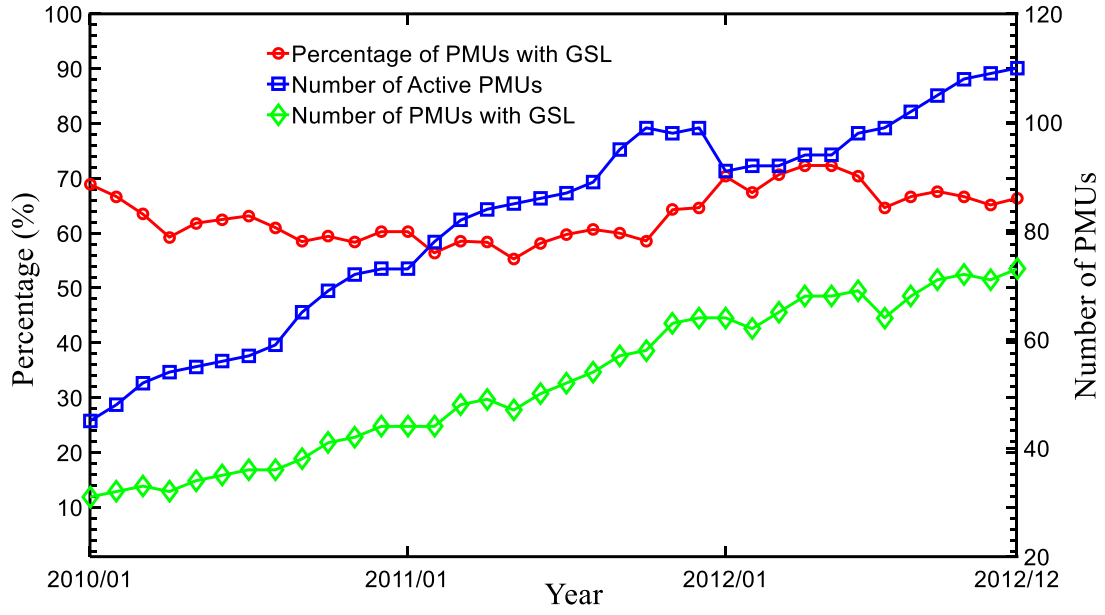


Figure 3.2. Methodology for PMU GSL prevalence analysis

3.3 Analysis results of GSL prevalence analysis in PMU

3.3.1 Presence of GSL in PMUs

According to the statistical analysis on the historical data in PDCs and FNET/GridEye server from 2010 to 2012, all PMUs and FDRs have ever experienced GSL event. The PMUs or FDRs that experienced GSL more than once per day on average are referred as frequent GSL units. It is illustrated in Figure 3.3 as PMUs and FDRs were increasing deployed in from 28 in Jan 2010 to 112 in Dec. 2012 and 26 in Jan 2010 to 133 in Dec, 2012 respectively, the number of GLS events grew at a relatively constant speed for both PMU and FDRs. Therefore, the percentage of GSL for PMUs and FDR are in the range of 59% to 75% and 60% to 70%, respectively, demonstrating that GSL is a widespread problem with a consistent probability of occurrence in PMUs.



(a)

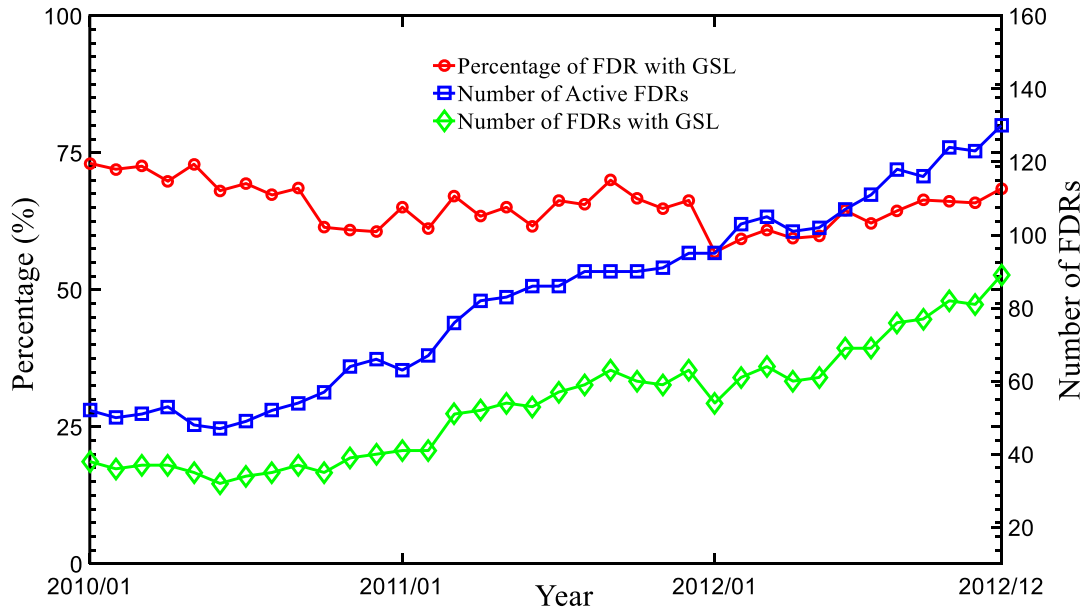


Figure 3.3. Presence of GSL in PMUs from 2010 to 2012
(a) Data from a PDC (b) Data from FNET/GridEye Sever

3.3.2 GSL event recovery time

A probability distribution of GSL recovery time can be obtained by statistically analyzing the duration of GSL. As illustrated in Figure 3.4, the trend of probability distribution curves for PMUs and FDRs are similar. The two curves both drop exponentially within a short time period, which indicates that majority of GSL event can be recoverable within 30 minutes.

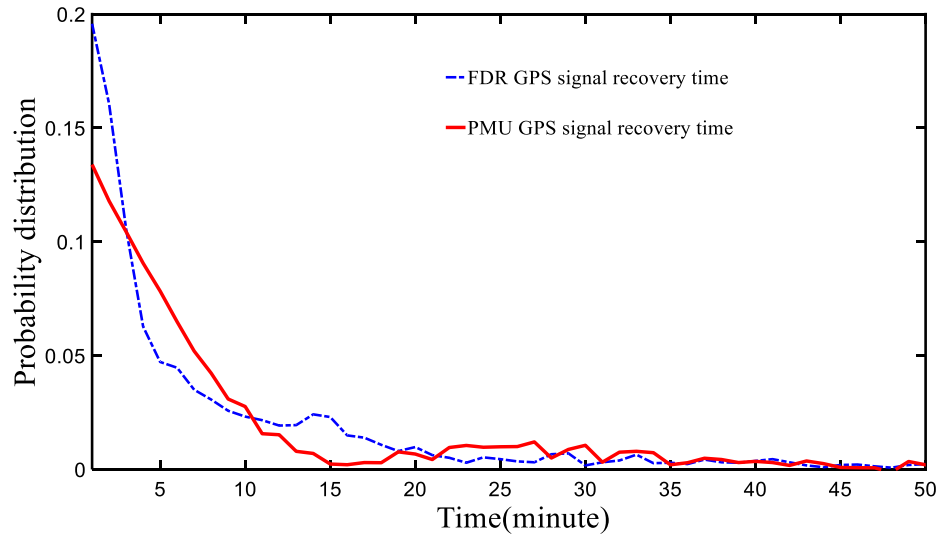


Figure 3.4. Probability distribution of GPS signal recovery time

3.3.3 Spatial-temporal analysis of GSL event

Theoretically, the satellite signal is affected by the geographic position of the antenna, which may influence the frequency of GSL event. To investigate the correlation between the GSL event and the geological locations, the GSL event of FDRs across North America are countered. According to the spatial distribution of GSL event illustrated in Figure 3.5, no significant geological pattern is found from historical data. To study the impact of solar activity on the GSL event, the number of GSL event per unit in FNET/GridEye and 10.7cm radio flux, an indicator of solar activity recorded from space weather prediction center, are plotted for data from the 2010 to 2012 as illustrated in Figure 3.6. From Figure 3.6, it can be seen no clear impact from solar activity on GSL can be detected. It is noted that the solar activity might influence some of GPS signal while GPS receivers only need to lock 1 or 2 satellites for synchronization, which eventually causes the uncorrelated correlation between the GSL event and solar activity. Figure 3.7 shows the monthly trends of detected GSL event, revealing that the GSL events evenly distribute each year

and no specific seasonal or monthly trend can be matched. Therefore, it can be concluded that GSL is a universal issue in PMUs with little correlation to time and location.

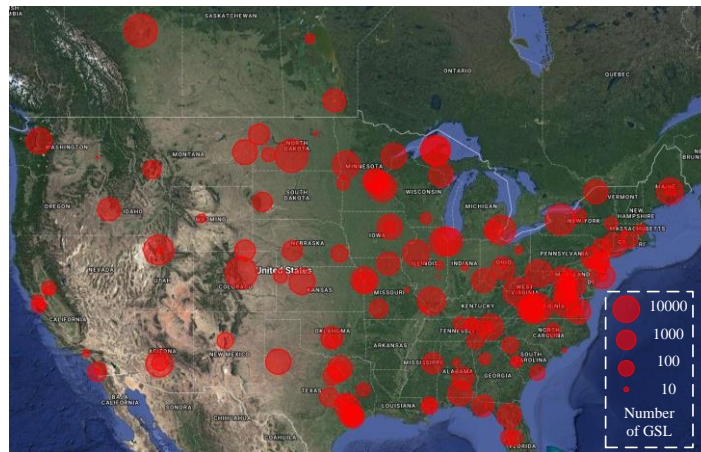


Figure 3.5. Spatial distribution of GSL in North America

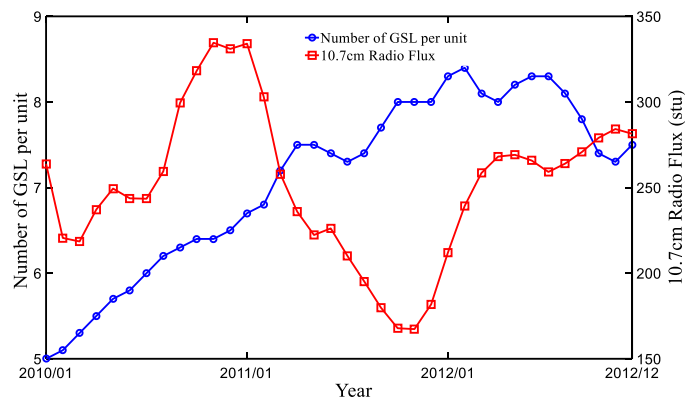


Figure 3.6. Correlation analysis of GSL and solar activity

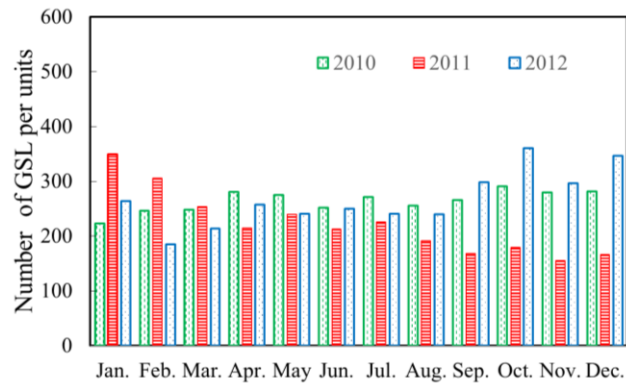


Figure 3.7. Monthly distribution of GSL in PMU

3.3.4 Daily pattern of GPS sign strength

Taking advantage of the NLS information in the FNET/GridEye data frame, the daily pattern of GSS can be explored to investigate the instability and unavailability of GPS signals. Generally, four typical GSS daily patterns have been discovered by statistically analyzing historical data. As illustrated in Figure 3.8, these four patterns include strong GSS (the NLS ranges from 6-12 GPS satellites), medium GSS (NLS mostly ranges from 2-6), weak GSS (NLS is mostly below 1 with frequent GSL), and variable GSS (NLS satellites varies randomly). Since all FDRs are installed indoor with directional GPS antennas rather than omnidirectional antennas, GPS signal receptions will be affected if obstructions block satellite broadcasts. The satellite signal may be blocked or reflected by buildings or other obstacles in certain times period of a day before received by GPS antenna, leading to the different daily pattern in Figure 3.8.

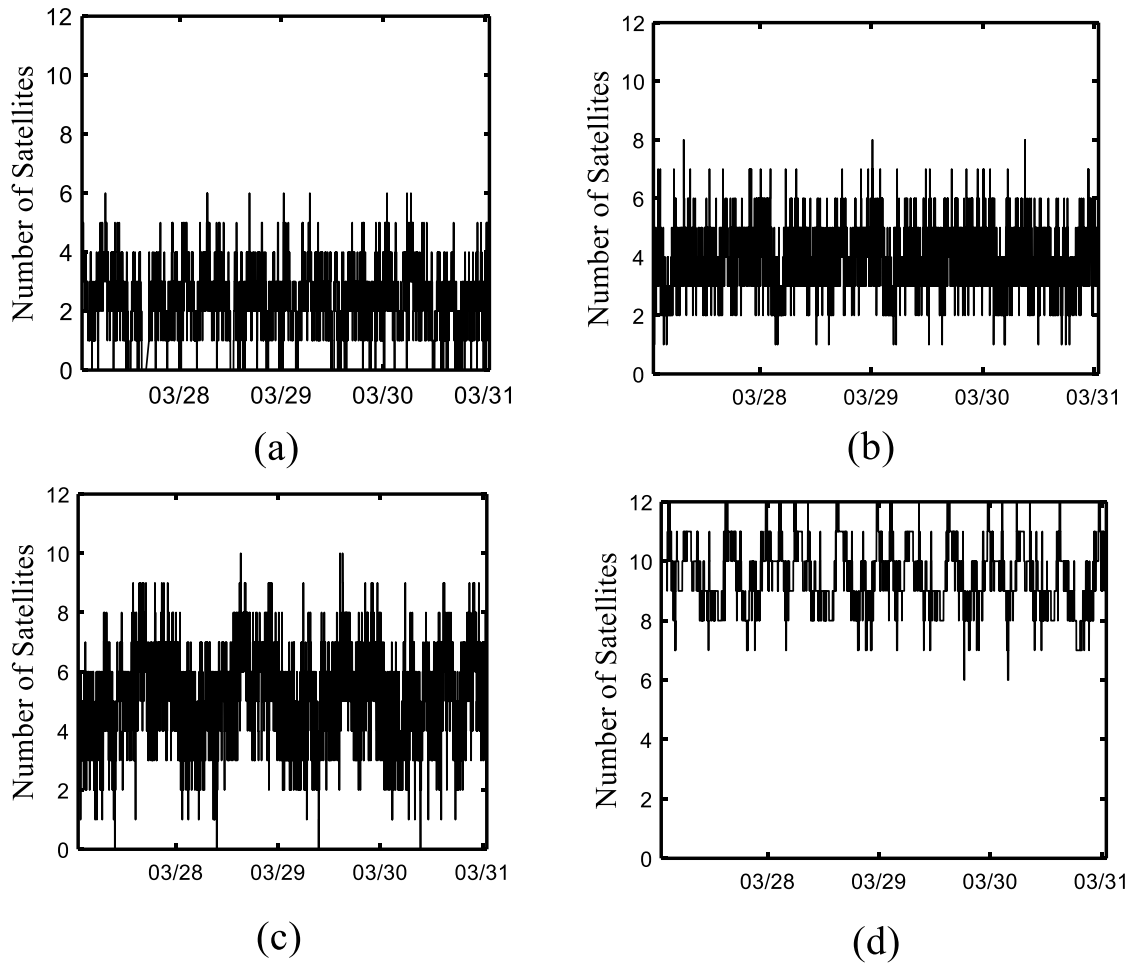


Figure 3.8. Daily pattern of GSS in FDR
(a) Weak GSS (b) Medium GSS (c) Variable GSS (d) Strong GSS

3.4 Impact analysis of GSL on PMU measurement

3.4.1 Analysis of timing error after losing GPS signal

Accurate time information from GPS receivers is essential for data synchronization in wide area deployment of SMDs. By demodulating the GPS signal, the GPS receiver can align its time with coordinated universal time (UTC) and then output a high precision pulse per second (PPS) signal for synchronization. The local receiver adjusts the phase of its oscillator to match the received signal. The delay caused by signal propagation and the Earth's rotation will be corrected by the local receiver. Other information, e.g., number of satellites locked, location coordinates, and satellite clock time, can be output in a millisecond level sub-frame after the PPS.

It should be noted that the error of PPS with stable GPS signal is typically less than 30 nanosecond, which is critical in order to realize accurate, stable, and synchronized measurement. Waveform sampling by an analog digital converter (ADC) in SMDs is triggered by the PPS. Although sampling between adjacent PPS signals is still controlled by the internal oscillator, the error caused by the oscillator can be cleared via PPS-trigger sampling each second. Once SMDs lose GPS time synchronization, they should rely on their internal crystal oscillators to provide the timing reference without GPS correction. Because of their accessibility and low cost, quartz-based crystals are used as the timing source in most measurement devices. However, there is an unintended and generally arbitrary frequency drift from the nominal frequency for crystals oscillators, which is caused by changes in temperature that alter the piezoelectric effect, problems with voltage regulators which controls the bias voltage to the oscillator, component aging, etc. For example, shifts in temperature can increase frequency drift by tens of PPM (part per million) even within the standard temperature range. The frequency drift of the oscillators will introduce a timing error in PMUs.

3.4.2 Impact of timing error on measurement

Assuming the timing error caused by frequency drift of the oscillators is t_{PPS} μ s, the angle error affected by this timing error within one second is

$$Error_{Angle} = 2\pi \times T_{PPS} \times 10^{-6} \times f_0 \quad (3.1)$$

where f_0 is the frequency of the power grid. Assuming the timing error is 0.2 μ s and power grid frequency is 60 Hz, the angle error is only 7.63 E-5 radians. However, the error would accumulate each second. Assuming the incremental error is constant for each second and there is no error in

magnitude measurement, the accumulated error over 10 minutes is 4.53×10^{-2} radians, which exceeds the 1% TVE limit of the IEEE standard.

According to the operation principle of synchronized measurement devices, the PPS timing error will only directly affect the first sampling each second. As a result, the measurement angle has the same DC offset each second. As the frequency can be defined as the derivation of angle in the typical frequency measurement algorithms, the frequency error caused by this timing error is

$$Error_{Frequency} = \frac{d(Error_{Angle})}{dt} \quad (3.2)$$

If the frequency of the power grid f_0 is in steady-state, there is no frequency measurement error caused by this timing error. Assuming f_0 ramps at a rate of 1 Hz/s, which is very unlikely large in the power system, the frequency estimation error caused by this timing error is only $0.1 \mu\text{Hz}$, which can still be ignored in power system applications. Thus, compared to the frequency, the angle measurement error is more sensitive to the timing error caused by frequency drift of oscillators without GPS signal correction.

3.5 Impact test of GSL in SMDs

3.5.1 PPS timing error test

The GPS receiver tested is the Motorola M12+ model [57] used in FDRs. In the ideal condition, the time interval between two adjacent PPS signals is one second. The actual PPS signals are evaluated by measuring the time interval between two adjacent PPS pulses. Thus, timing error “S1”, “S2” and “S3” are obtained by comparing the actual timing interval of PPS pulses and 1 second.

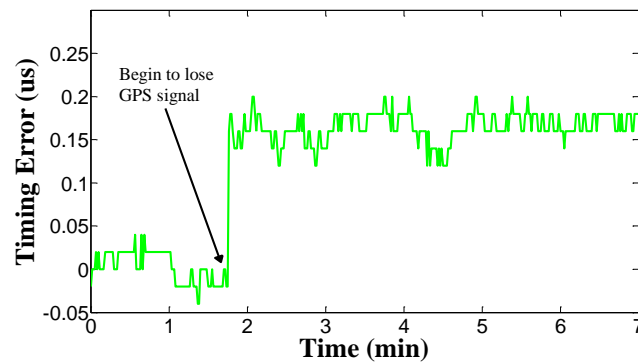


Figure 3.9. PPS error from a GPS receiver when GPS signal is lost

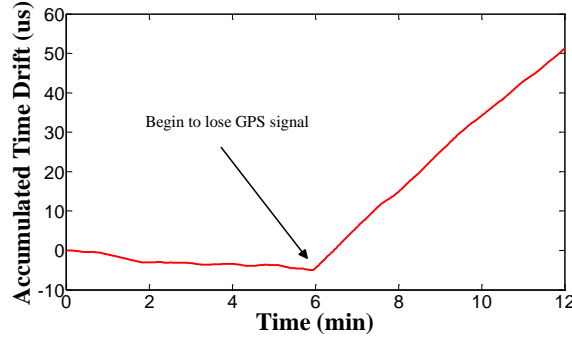


Figure 3.10. Accumulated time drift when GPS signal is lost

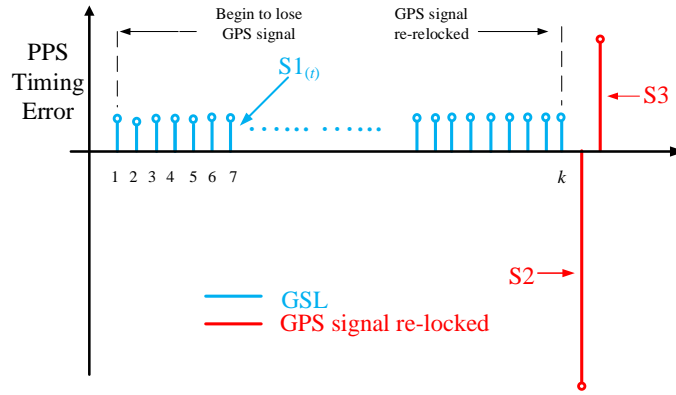


Figure 3.11. Pattern of the output PPS when GPS signal is lost

As illustrated in Figure 3.9, the PPS has an approximate $0.15 \mu\text{s}$ error when receivers lose GPS signal. The error accumulates and leads to the time drift shown in Figure 3.10. The drift nearly reaches $56 \mu\text{s}$ after GPS signal is lost for 6 minutes, which amounts to an angle error of $2.2\text{E-}2$ radians when frequency of signal is 60Hz. The pattern of the output PPS error after GSL is illustrated in Figure 3.11. The PPS timing error “S1” occurs when GPS signal is lost. When the GPS signal is re-locked, the PPS will undergo a two second transition with two spikes “S2” and “S3”, which compensates the total time drift during the period without GPS signal. Thus “S1”, “S2” and “S3” should satisfy the following equation

$$\sum_{t=1}^k S1_{(t)} + S3 = S2 \quad (3.3)$$

where k is the number of seconds of GSL. Table 3.1 gives some real measurements of “S1”, “S2”, and “S3”. The big spike “S2” can be as large as several hundred microseconds.

Table 3.1 Test result of timing error

Length of GSL	6 minutes	12minutes	24 minutes
Average S1	+0.15 μ s	+0.18 μ s	+0.17 μ s
S2	-56.25 μ s	-130.01 μ s	-245.18 μ s
S3	1.87 μ s	0.41 μ s	3.38 μ s

3.5.2 Test with a signal generator

As shown in Figure 3.12, a Doble F6150 Power System Simulator (equipped with GPS antenna) is used to generate simulated signals (60 Hz, 120V) for the FDRs. A photo of the test setup is presented in Figure 3.13.

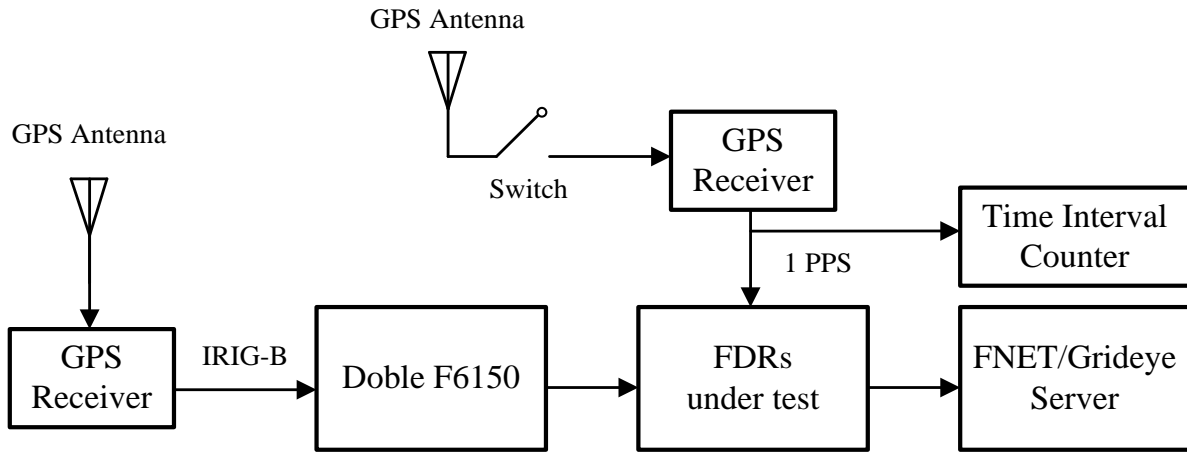


Figure 3.12. Block diagram of the test system

The Doble power source is required to obtain stable GPS signals throughout the test so it can act as an accurate and reliable reference for the evaluation. The GPS antennas of the FDRs under test are plugged into their devices for 20 minutes to obtain stable signals before being unplugged for 30 minutes to test the impact of GSL. The antennas are reconnected after this period to recover GPS signal for another 30 minutes.

The results of frequency, angle, and voltage magnitude are shown in Figure 3.14(a)-(c). It can be seen that the accuracy of frequency and voltage magnitude measurements are not noticeably affected by the GSL while the measurement error of the angle increases linearly with GSL duration. The angle drift is caused by the accumulating error of the initiating PPS imprecision that is

introduced once the GPS signal and the resulting time synchronization are lost. The measurement of frequency is not as sensitive as angle because frequency is not directly measured but calculated through derivation of angle.

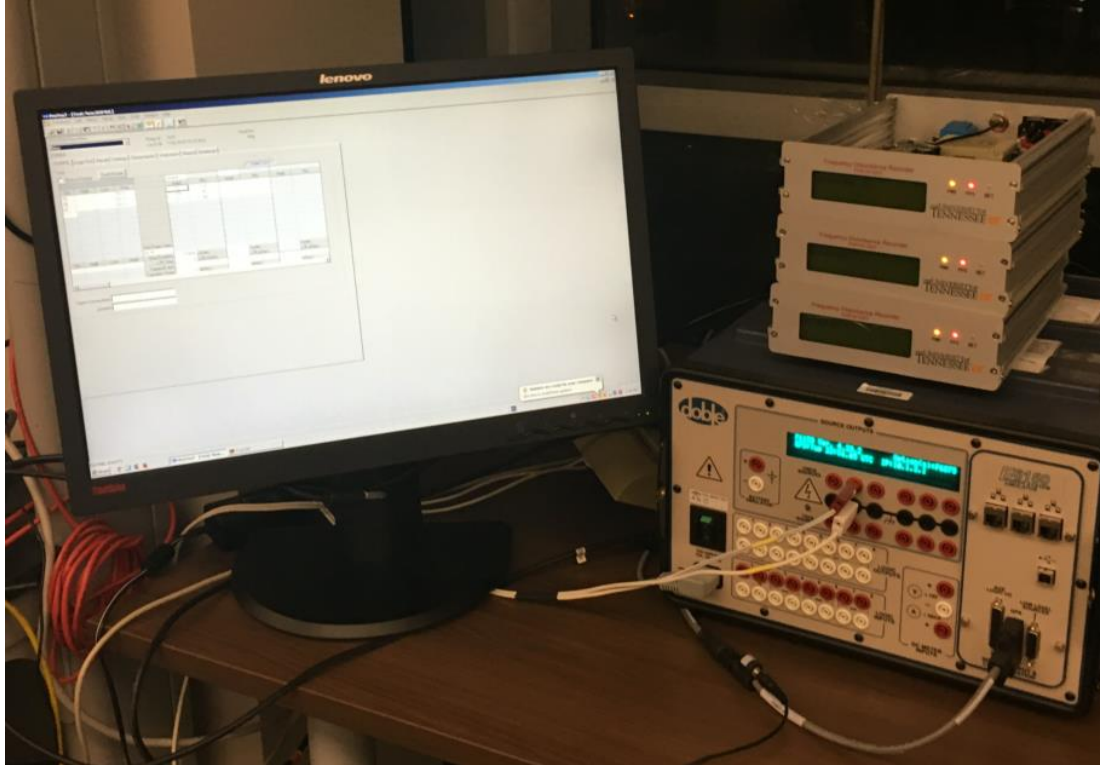
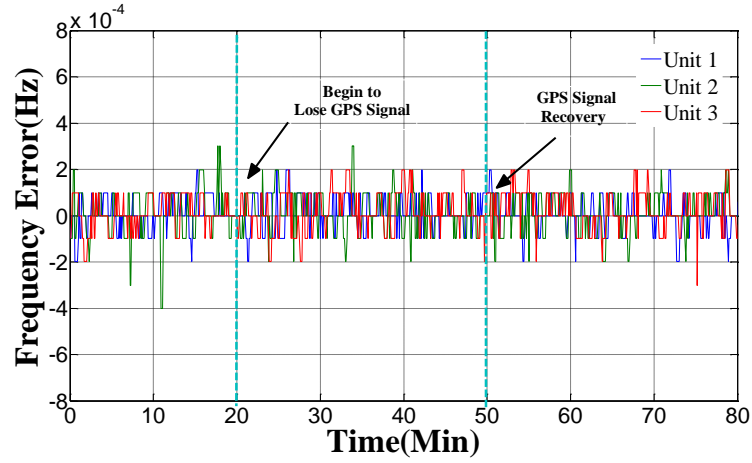
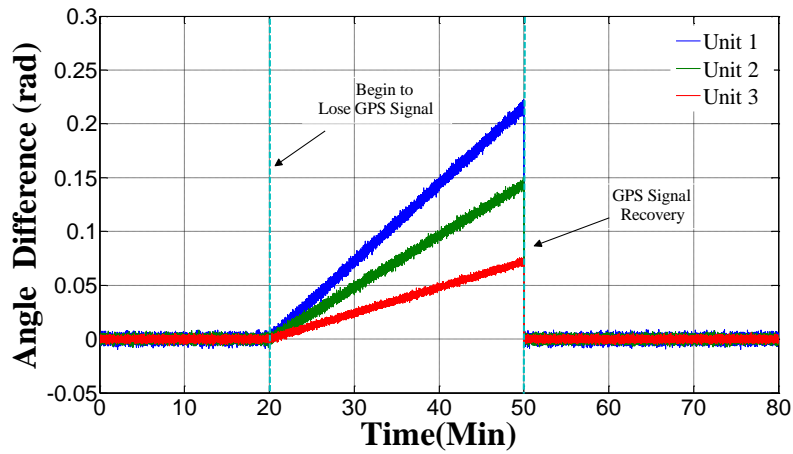


Figure 3.13. The test system setup

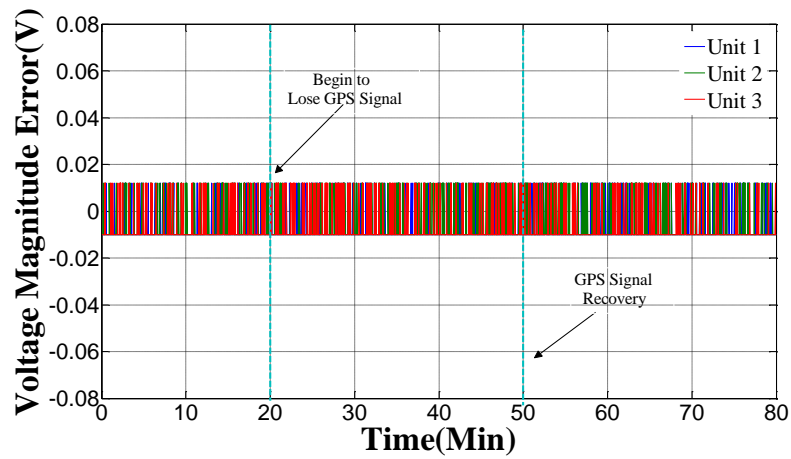
Another interesting phenomenon that should be noted is that the angle drift for each of the three tested FDRs are different. The slopes are 0.00233 rad/min for unit 1, 0.00481 rad/min for unit 2, and 0.00651 rad/min for unit 3, respectively. Considering that FDRs depend on their internal crystal oscillators after losing GPS signal, this indicates that the frequency drift of each crystal oscillator is different caused by difference in the degree of aging or operation temperature. As a result, angle drift speed is random for each individual FDR.



(a) Frequency

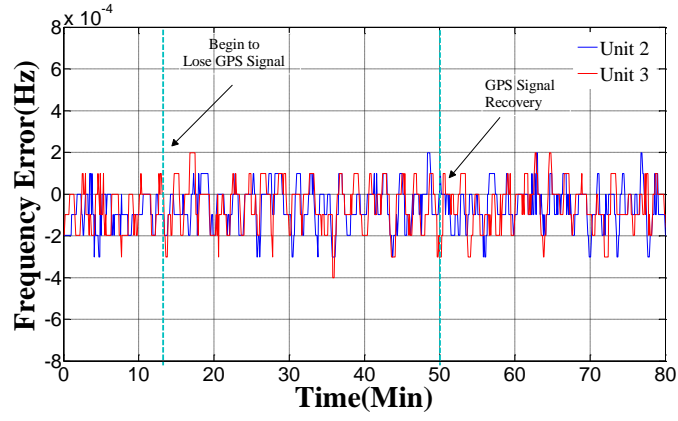


(b) Angle

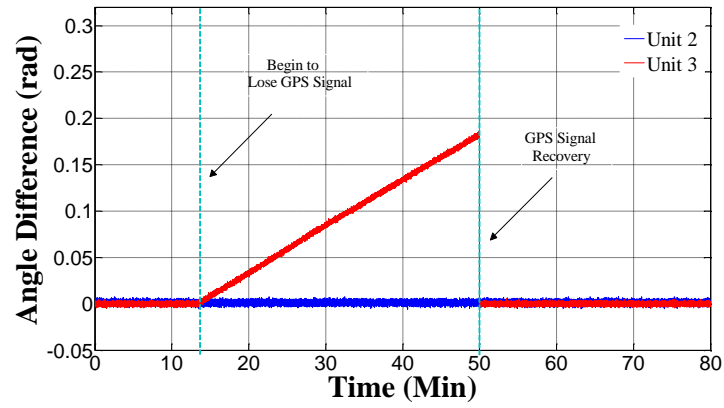


(c) Voltage Magnitude

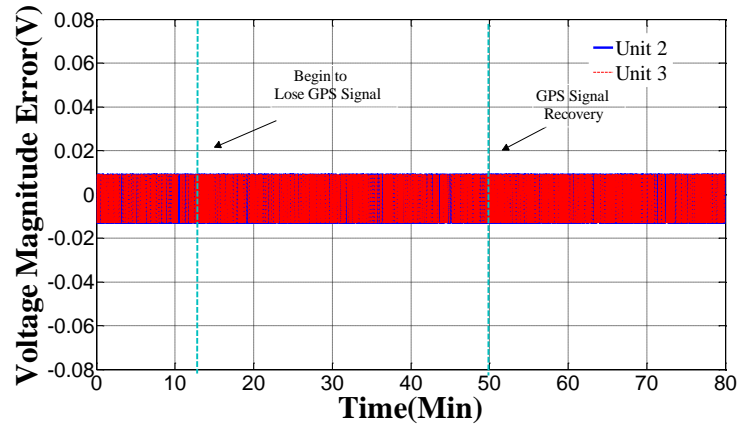
Figure 3.14. Test results with the signal generator



(a) Frequency



(b) Angle



(c) Voltage Magnitude

Figure 3.15. Test results with real power grid signals

3.5.3 Test with real power grid signals

To test FDR performance with actual power grid signals, three FDRs, unit 1, unit 2 and unit 3, are connected to real power grid signals simultaneously. The first FDR, unit 1, selected as the measurement reference, is connected to a GPS antenna for the duration of the entire procedure to guarantee measurement accuracy. The antenna of FDR unit 2 is also connected for the whole procedure for the sake of comparison. The antenna of FDR unit 3 is unplugged to simulate the effect of GSL for 35 minutes and then re-connected to re-lock the GPS signals. The results are shown in Figure 3.15(a)-(c) and are similar to the results seen using the signal generator. A significant angle drift can be observed when losing GPS signal while the impact on frequency and voltage magnitude are very small. There is a sharp angle drop when the units re-locks the GPS signal, seen in both Figure 3.15(b) and Fig. 12(b), which is caused by the spikes “S2” and “S3” of the output PPS in Figure 3.11.

The abnormal angle measurement in Figure 3.15(b) may trigger a false detection of a power system event or a protection action in some SMD measurement based power grid applications. For adaptive out-of-step relay protection, mechanical power can be estimated using a set of real time angle measurement and then equal-area criterion is used for stability analysis[22]. If GLS occurs, the accumulated angle measurement error will cause incorrect estimation of mechanical power, which is likely to result in inappropriate determination of swing stability and wrong operations of relay action [23][26]. Moreover, angle errors of 1.66×10^{-2} and 1×10^{-2} radian are able to cause failure of event location and oscillation detection for FNET/GridEye application on Eastern Interconnection system respectively. Furthermore, 1×10^{-2} radian angle error can lead to 10% error and the extreme error can be up to 45.87% for the dynamic line rating [13]. Since the accuracy of voltage magnitude measurement keep stable with GSL as shown in Figure 3.14(a) and Figure 3.15(a), the negative impact of GSL on the linear state estimation is also from phase angle drift [21].

3.6 Potential solutions for GPS signal loss on PMU

The above experimental results reveal the negative influence of GSL on the angle measurement accuracy. In this section, two potential solutions including an angle compensation method and a supplementary timing source method are discussed to mitigate the impact of GSL on PMU. Preliminary results demonstrate the effectiveness and accuracy of both solutions. The

limitation and drawback of these solutions are also discussed. FDR is used as a testbed to demonstrate the implementation of these potential solutions.

3.6.1 Angle Compensation Solution

As illustrated in Figure 3.15(b), the angle error increases linearly with GSL duration at random speed for each individual device. To compensate the angle drift, the critical step is to obtain the angle drift speed, which is determined by the real operation frequency of crystal oscillator. To real-time monitor the crystal oscillator, the timing signal from the GPS receiver can be used as a timing reference when the GPS signal is available. It is assumed that the frequency of the crystal oscillator does not change in a short period. As most GSL events in PMUs can be resolved within 30 minutes as illustrated in Figure 3.4, the angle compensation method mainly aims to rectify the angle measurement in this period of time.

Assuming a y -bit microprocessor operates at nominal frequency f_{osc} , the real monitored frequency of the oscillator F_{osc} is expressed as

$$F_{osc} = \frac{((W_k - W_{k-1}) + g \times 2^y)}{m} \quad (3.4)$$

where m is the value of phase-locked loop multiplier control register, g is the number of the timer overflows between two timing signal. The rising edge of the timing signal triggers an external interrupt to read the timer counter register (TCR) and thus W_{k-1} and W_k are the values of the TCR at the arrival of adjacent PPSs, respectively as illustrated in Figure 3.16. Using the latest calculated frequency of crystal oscillator F_{osc} before losing GPS signal, the timing error for the k th second of GSL is

$$Error_{PPS(k)} = \frac{W_k - W_{k-1} + g \times 2^y}{mf_{osc}} - 1 \quad (3.5)$$

The k th second angle drift after GSL is

$$Error_{Angle(k)} = \frac{2\pi \times Error_{PPS(k)}}{f_{grid(k)}} \quad (3.6)$$

where $f_{grid(k)}$ is the frequency of the power grid at k th second, which is not affected by the GSL illustrated in Figure 3.14. Therefore, the total angle drift in k seconds is

$$Angle_{drift(k)} = \sum_{t=0}^k Error_{Angle(t)} \quad (3.7)$$

Finally, the angle measurement can be compensated via the following compensation formula

$$Angle_{comp(k)} = Angle_{Measured(k)} - Angle_{drift(k)} \quad (3.8)$$

where $Angle_{Measured}$ is the raw angle measurement in PMUs and $Angle_{comp}$ is compensated angle measurement

The laboratory experiment is conducted for performance evaluation of the above compensation method. The angle measurements results are shown in Figure 3.17. It is clear that the angle drift is effectively compensated using the angle compensation method. The angle measurements with and without the angle compensation for different GSL duration are listed in Table 3.2, which demonstrate more than 90 % angle drift has been compensated. The TVE after implementing compensation method is 0.62%, which meets IEEE standard C37.118.2011, compared with 7.01% without angle compensation which exceeds the 1% limit in IEEE standard.

Table 3.2 Angle measurement result comparison using compensation method

Length of GSL	Without Angle compensation		With Angle Compensation	
	Angle(radian)	TVE%	Angle(radian)	TVE%
10 minute	4.12×10^{-2}	3.4	1.62×10^{-3}	0.03
30 minute	1.12×10^{-2}	7.01	9.51×10^{-3}	0.62

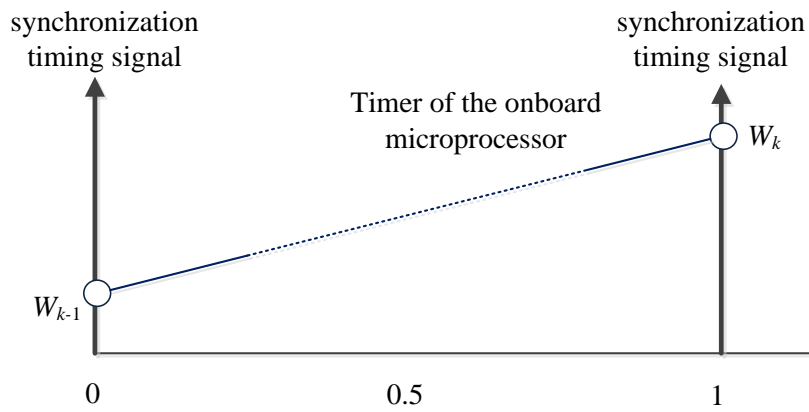


Figure 3.16. Monitoring of crystal oscillator frequency

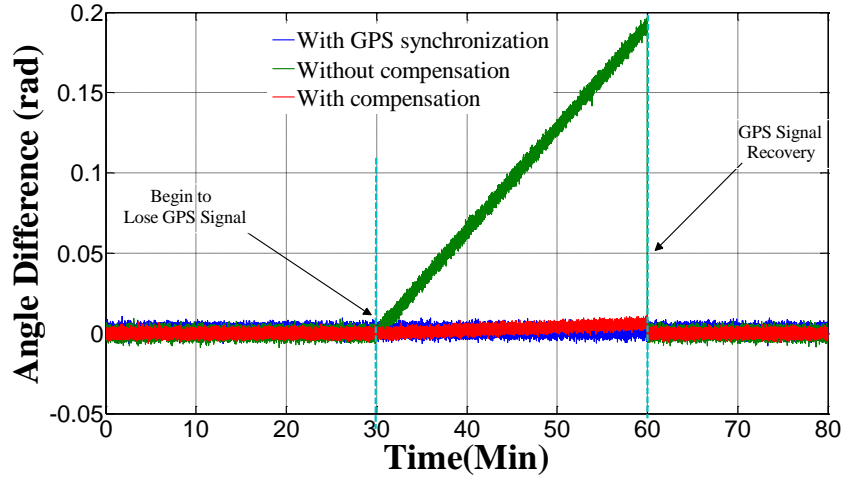


Figure 3.17. Angle measurement test result

3.6.2 Supplementary timing source solution

Equipping with an accurate secondary timing source (Atomic clock or e-Loran) or redundancy design of GPS receiver [58] in PMUs is another effective solution for GSL issue [56]. The most convincing test to verify the effectiveness of a supplementary timing source is to connect it to a PMU and compare the measurement accuracy with the GPS-based PMU. A commercial chip scale atomic clock (Microsemi Quantum SA.45s) [52] [59] and eLoran system (UrsaNav UN-152A)[60] are used as timing sources of FDRs to provide the timing signal instead of the GPS receiver for synchronization. To make a direct comparison, three FDRs will be involved in this test as illustrated in Figure 3.18. One is referred to as GPS-FDR., whose timing is provided by GPS while the other two are referred to as 'Atomic clock-FDR'. and 'eLoran-FDR' whose timing are provided by the atomic clock or eLoran respectively. All the FDRs are connected to the PMU calibration device Doble F6150, which generates stable and accurate 60 Hz waveform. Figure 3.19 shows angle measurement comparison between GPS-FDR, atomic clock-FDR, and eLoran-FDR. It can be seen that the angle errors of all FDRs are less than 1×10^{-3} radian, all of which sufficiently meet the IEEE standard (9.94×10^{-3} radian) and there is no noticeable difference of angle measurement between these FDRs. The comparison angle measurement errors are listed in Table 3.3. The measurement accuracy of these three FDRs is at the same level, which verifies that Atomic clock and e-Loran have the ability to provide equivalently accurate timing signal to maintain the PMU measurement accuracy.

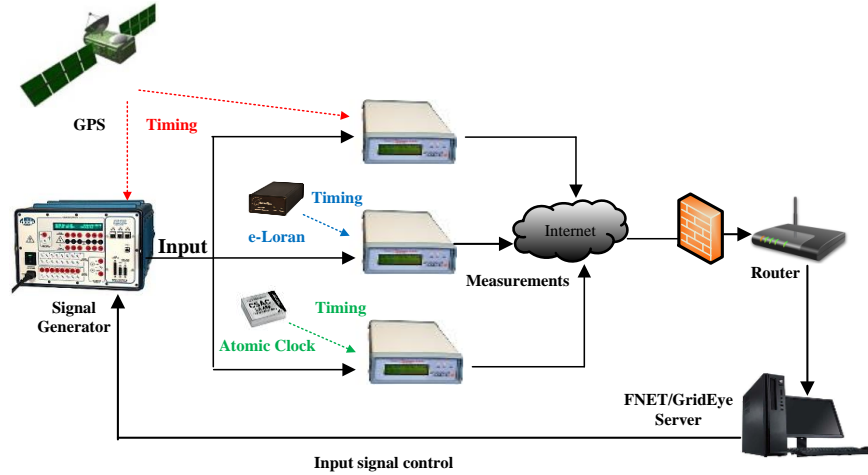


Figure 3.18. Test setup block for the supplementary timing source solution

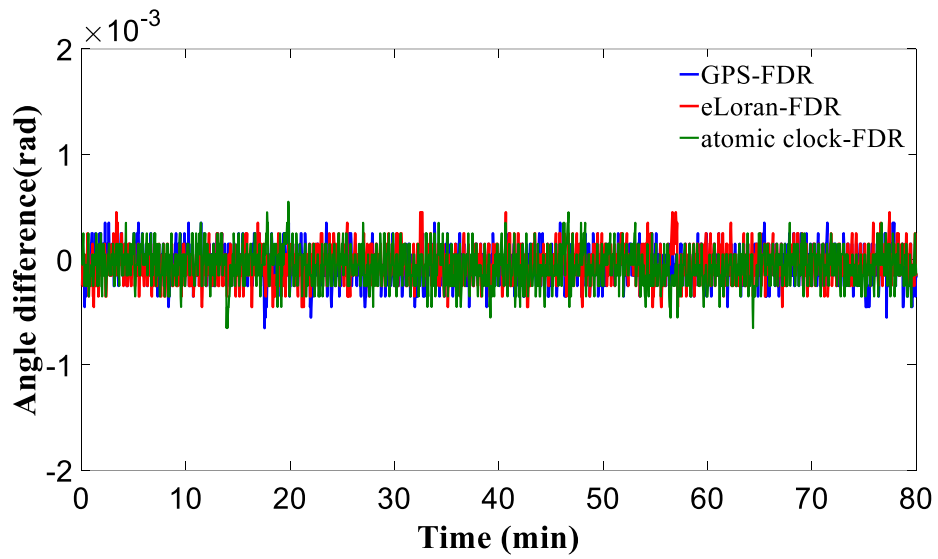


Figure 3.19. Angle measurement comparison for the supplementary timing source solution

Table 3.3 Angle measurement result comparison

	GPS-FDR	Atomic clock-FDR	eLoran -FDR
Angle Error (radian)	5.375×10^{-4}	5.499×10^{-4}	5.421×10^{-4}

3.6.3 Discussion

The advantage of the angle compensation method is that no extra hardware is needed to reduce the angle drift. However, the onboard oscillator frequency can only be measured when the GPS signal is available because the timing reference signal is no longer accurate after losing GPS signal. Therefore, the last measured oscillator frequency measurement before GSL is used for compensation, which resulting the angle drift not fully compensated and limiting the effective time of the compensation.

Supplementary timing source solutions are able to provide ultra-high timing accuracy to meet IEEE standards for a much longer period of time compared with previous angle compensation solution. However, those require additional hardware costs, which impedes their application in large volume production. It should be noted that since atomic clock itself does not have a timing start point, it requires an external timing source, such as a GPS module for disciplining[52]. That means an atomic clock can only be considered as a backup, rather than a replacement of a GPS timing source. It should also be noted that as a ground-based technology, the reliability and accuracy of eloran will be influenced by human activity and environments change [60].

3.7 Conclusion

In this chapter, the impact, prevalence and solution of GSL in the wide area monitoring system were studied. There are three main contributions in chapter as fellows: First, a large amount of historical PMU data was statistically analyzed to investigate the occurrence of GSL on PMU. The data analytical results reflect that GSL is a widespread issue in PMUs though most of the GSL events were resolved quickly. It is also found out there is no direct relationship between GSL and spatial location, time period and solar activity. Second, to assess the impact of GSL on PMUs, laboratory experiment on PMUs was performed to. The results show GSL will introduce a roughly linear angle drift with GSL duration and greatly impair the accuracy of angle measurement. Third, to mitigate the impact of GSL on PMUs, two potential solutions, the angle compensation and the supplementary timing source, are provided and compared. The angle compensation solution provides reduced, but not eliminated, angle drift during shorter GSL windows (30 minutes) without adding extra hardware while the supplementary timing source solution can maintain the same measurement accuracy level as GPS time synchronization for a long GSL period with additional hardware costs.

Acknowledgment

This chapter is, in part, a reprint of the material in the papers: Wenxuan Yao, Yong Liu, Dao Zhou, Zhuohong Pan, Jiecheng Zhao, Micah Till, Lin Zhu, Lingwei Zhan, Qiu Tang, Yilu Liu. “Impact of GPS Signal Loss and Its Mitigation in Power System Synchronized Measurement Devices” *IEEE Transactions on Smart Grid* , vol. 9, no. 2, pp. 1141-1149, March 2018, and Wenxuan Yao, Dao Zhou Lingwei Zhan Yong Liu, Yi Cui, Shutang You, Yilu Liu, “GPS Signal Loss in the Wide Area Monitoring System: Prevalence, Impact, and Solution”, *Electric Power Systems Research*, 2017, 147:254-262

Chapter 4 Phasor Measurement Integrated with Novel Sensors

4.1 Introduction

Traditional synchrophasor, usually installed in substations at the transmission level, must be connected physically with a bus or line through potential transformers (PTs) and current transformers (CTs), which requires high manufacturing, installation, and maintenance costs [29]. For example, the installation cost of one transmission-level synchrophasor was more than \$8,000 at the Tennessee Valley Authority (TVA) [61]. Such high cost obviously impedes large-scale deployment across the power grid.

Furthermore, in some remote areas, far from any substation, it is difficult to install and maintain a synchrophasor due to the lack of facilities. However, high voltage overhead transmission lines are indispensable components of the power grid and abnormal changes of parameters in any part of the transmission network may lead to serious damage or even interruption of power delivery [67]. Thus, there is a need to monitor the frequency and angle of overhead high voltage transmission lines in such areas to maintain reliable and stable operation across the entire grid. Therefore, portable and flexible phasor measurement devices are required.

Per electromagnetic theory, overhead transmission lines generate electric and magnetic fields simultaneously in their right-of-way corridors [24],[62]. Since the frequency of these two fields reflects the frequency of the transmission line, it is, then, feasible to obtain frequency characteristic of the transmission line by sensing these two fields. An electric or magnetic sensor can be used to translate the alternating field signal into an alternating current or voltage signal. Thus, an input signal can be obtained without a direct connection. Based on this principle, this chapter introduces two types of devices, one using each field type, an electric field sensor based non-contact synchronized measurement device (E-NCSMD) and a magnetic field sensor based non-contact synchronized measurement devices (M-NCSMD). Both E-NCSMD and M-NCSMD can perform frequency and angle measurement from ground-level of the overhead transmission line right-of-way corridor, which can work as supplementary of conventional synchrophasors for wide area monitoring of the transmission network.

4.2 Theoretical foundation

In this section, the theoretical foundation for electric and magnetic field sensors are discussed, respectively.

4.2.1 Acquisition of electric field signal

According to electromagnetic theory, a conductor produces an electric field in its surroundings [62][63]. The electric field in the vicinity of multi-conductor power lines can be evaluated by superimposing the contribution from each conductor [63]. For simplicity, consider three infinite and balanced transmission line with radius r , shown in Figure 4.1, according to the Gauss's law [68], the combined electric field E of observed point P at the ground panel can be expressed as

$$\mathbf{E} = \underbrace{\mathbf{p}_a \frac{\lambda_a}{2\pi\epsilon_0 d_a}}_{\mathbf{E}_a} + \underbrace{\mathbf{p}_b \frac{\lambda_b}{2\pi\epsilon_0 d_b}}_{\mathbf{E}_b} + \underbrace{\mathbf{p}_c \frac{\lambda_c}{2\pi\epsilon_0 d_c}}_{\mathbf{E}_c} \quad (4.1)$$

where λ_a , λ_b , and λ_c are the electric charge density of the infinite lines, respectively. d_a , d_b and d_c are the perpendicular distance between the conductors and the observed point. ϵ_0 is the permittivity of free space. \mathbf{p}_a , \mathbf{p}_b , and \mathbf{p}_c are the unit direction vectors for each transmission line which depends on the relative position between the conductors and the observed point.

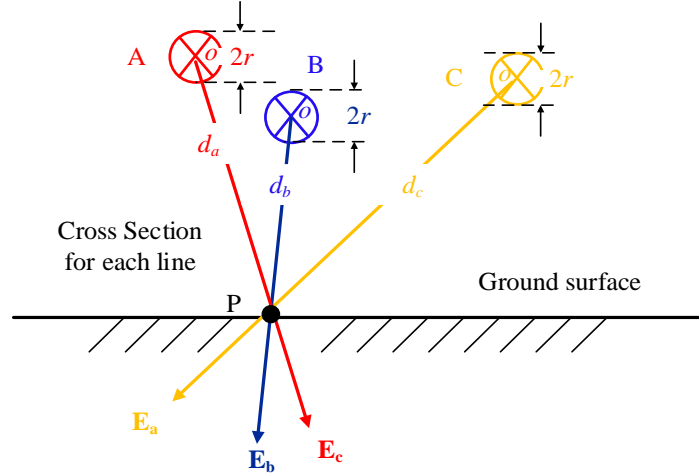


Figure 4.1. Electric field calculation of three straight power line conductors

For a balanced system, the voltage of the three transmission lines U_a , U_b and U_c are equal in frequency f , but displaced by 120° from one another, which can be expressed as

$$\begin{aligned}
U_a &= |V_p| \cos(2\pi ft + \beta) \\
U_b &= |V_p| \cos(2\pi ft + \beta + 120^\circ) \\
U_c &= |V_p| \cos(2\pi ft + 240^\circ)
\end{aligned} \tag{4.2}$$

where β is the initial angle.

The voltage for each transmission line can be calculated by integrating the electric field along the direction of the radius. Take line A as an example, according to the relationship between the voltage and electric field, the voltage can be expressed as

$$U_a = \int_r^{d_a} \frac{\lambda_a}{2\pi\epsilon_0 r} dr = \frac{\lambda_a}{2\pi\epsilon_0} \ln\left(\frac{d_a}{r}\right) \tag{4.3}$$

Substituting λ_a , λ_b , and λ_c into equation (4.1), the instantaneous strength of the electric field at point P can be expressed as

$$\mathbf{E} = \mathbf{p}_a \frac{U_a}{\ln\left(\frac{d_a}{r}\right) d_a} + \mathbf{p}_b \frac{U_b}{\ln\left(\frac{d_b}{r}\right) d_b} + \mathbf{p}_c \frac{U_c}{\ln\left(\frac{d_c}{r}\right) d_c} \tag{4.4}$$

Equation (4.4) indicates the frequency of the electric field at a fix point is equal to frequency of the conductor. The superposition principle can be applied to the angle and magnitude of the electric field vectors, which are determined by the relative position between the observed point and the transmission lines.

According to the IEEE 644-1994 standard [24], if the electric field is strong enough and is not overwhelmed by the environmental noise, it can be captured by a free-body meter as input signal for transmission line. Based on this idea, an electric field sensor is designed to replace traditional PTs and CTs for frequency and angle measurement. There are two parallel copper regions on the top layer and the bottom layer of printed circuit board to form a free-body meter. A small alternating electric potential will be induced between the two layers by the varying electric field, as shown in Figure 4.2. Ideally, the dimension of the copper is infinite to avoid edge effect. Practically, to balance the tradeoff between the edge effect and portability, the dimensions of the electric sensor are determined as shown in Table 4.1. This induced electric signal will be magnified by an amplifier circuit, formed with a voltage follower and an inverting negative feedback amplifier. To adapt the sensor for different electric field strengths, the gain ratios can be adjustable by changing the value of a variable resistor, as illustrated in Figure 4.2. A low pass filter is used

to block high frequency noise and isolate the low frequency component of the amplified signal V_{out1} . Then the filtered signal is fed into an ADC.

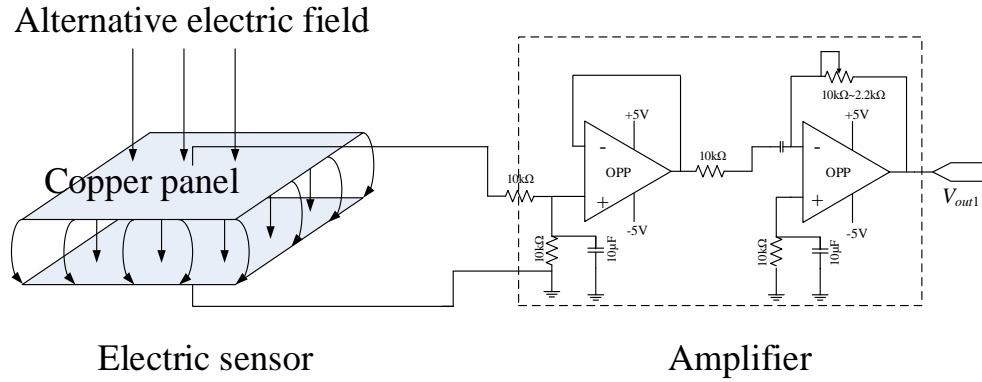


Figure 4.2. Illustration of electric field sensor and amplifier circuit

Table 4.1 Dimensions of Electric Field Sensor

Length	Wide	Distance
5.05cm	3.05cm	0.16cm

4.2.2 Acquisition of magnetic field signal

According to Ampere's Law, an AC current carrying conductor will produce a magnetic field in the surrounding atmosphere, as well as in nearby objects. The magnetic field is perpendicular to the electric field. Based on the Biot–Savart Law, the emanated magnetic field from the currents in the phase conductors are correlated with the electrical parameters of the currents [64]–[66]. Therefore, it is possible to work inversely to find out the phasor information of the conductors by measuring and analyzing the emanated magnetic field. The strength of the magnetic field is proportional to the magnitude of current and is inversely proportional to the distance to the conductor. Consider the three infinite power current lines with AC current I_a , I_b , and I_c in Figure 4.3. Based on Ampere's law [68], the magnetic field B at point Q can be expressed as

$$\mathbf{B} = \underbrace{\mathbf{q}_a \frac{I_a \mu}{2\pi l_a}}_{\mathbf{B}_a} + \underbrace{\mathbf{q}_b \frac{I_b \mu}{2\pi l_b}}_{\mathbf{B}_b} + \underbrace{\mathbf{q}_c \frac{I_c \mu}{2\pi l_c}}_{\mathbf{B}_c} \quad (4.5)$$

where μ is the magnetic permeability of the medium and \mathbf{q}_a , \mathbf{q}_b , and \mathbf{q}_c are the unit direction vectors for each transmission line. l_a , l_b and l_c are the perpendicular distance between the conductors and the observed point. According to Faraday's Law, an electromotive force will be

induced due to the changing of magnetic flux. For a balanced system, I_a , I_b and I_c have a frequency and magnitude at 120° angle separation as U_a , U_b , and U_c in (4.2). Suppose there is an N -turns coil at the point Q , then the induced electromotive force, EF , can be expressed as

$$EF = N \frac{d\Phi}{dt} \quad (4.6)$$

where Φ is the total magnetic flux, which can be expressed as

$$\Phi = S \times (\cos \gamma_a \times B_a + \cos \gamma_b \times B_b + \cos \gamma_c \times B_c) \quad (4.7)$$

where S is the area of the coil and γ_a , γ_b , and γ_c are the angles between the magnetic field lines and perpendicular to the coil surface, respectively.

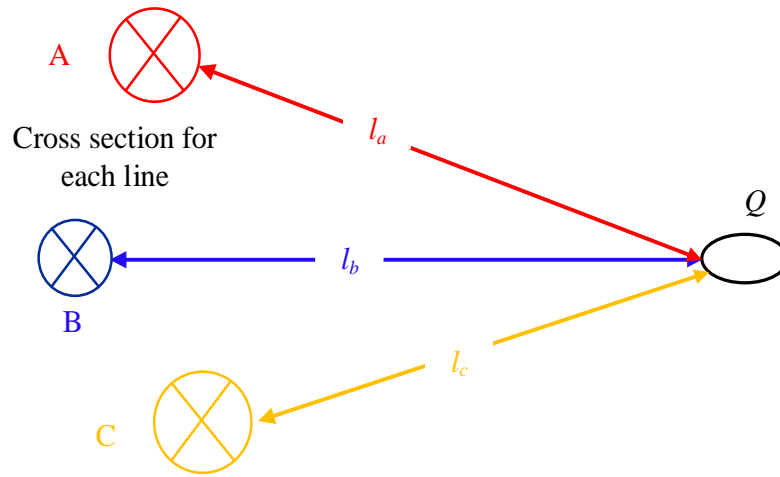


Figure 4.3. Magnetic field strength of three infinite straight conductors.

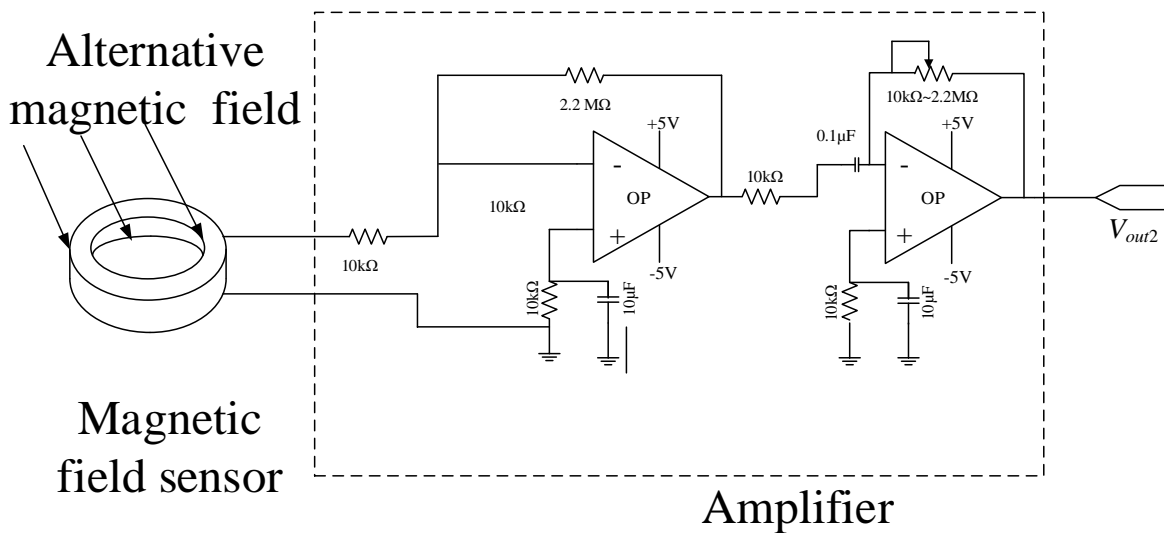


Figure 4.4. Illustration of magnetic field sensor and amplifier circuit

According to (4.6) and (4.7), the strength of the induced voltage signal, EF is proportional to the size of the coil and the number of turns. Requiring a compromise between signal strength and the portability of the non-contact measurement device, the dimensions of the magnetic field sensor are given in Table 4.2. Similar to the electric field sensor, a two stage amplifier circuit is used to amplify the induced voltage signal EF , as illustrated in Figure 4.4. The gain ratio of the second stage is flexible to accommodate different signal strengths.

Table 4.2 Dimensions of magnetic field sensor

Number of turns	Coil length	Coil diameter	
		Inner	External
1000	9cm	5cm	1cm

4.3 Device prototype development

The prototype development of E-NCSMD and M-NCSMD are discussed in this section. First, the hardware designs for these two types of non-contact SMD are introduced. Then, the single phase angle and frequency measurement algorithms adopted in E-NCSMD and M-NCSMD are presented.

The E-NCSMD and M-NCSMD are both developed on the Frequency Disturbance Recorders (FDR) platform. The non-contact sensors replace the potential transducer in FDRs for signal input. Besides the sensors, the E-NCSMD and M-NCSMD consist of a GPS receiver, a digital signal processor (DSP), microprocessor (MCU), data transceiver module, and solar battery module. The DSP is a TMS320LF2407 model, which is a 16 fix-point processor with the main core clock 30 MHz. The hardware design is shown in Figure 4.5. The electric field sensor and magnetic field sensor are used to acquire input signals for the E-NCSMD and M-NCSMD, respectively. A low-pass filter with a cut-off frequency of 150 Hz rejects high-frequency noise and harmonic inference. Since the error of PPS with a stable GPS signal is less than 30 nanoseconds, the rising edge of the PPS is used to trigger an interrupt in the DSP and consequently trigger the first sampling command to the ADC each second, as illustrated in Figure 4.6. The length of each synchronous sampling cycle is 1 second to match the PPS. From the second sample to last sample between adjacent PPS signals, the sampling interval is controlled by a timer in the DSP through the serial peripheral interface (SPI) bus. The DSP also performs phasor estimation and then transmits the measurements

to the MCU. The measurements are time-stamped in the MCU and sent out from the data transceiver. The total power consumption for both the E-NCSMD and M-NCSMD are less than 5 watts each, which can be provided by the solar battery module.

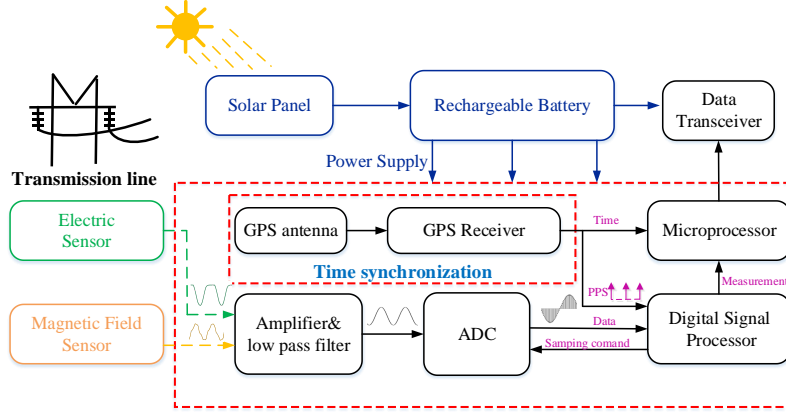


Figure 4.5. Hardware design of the E-NCSMD and M-NCSMD

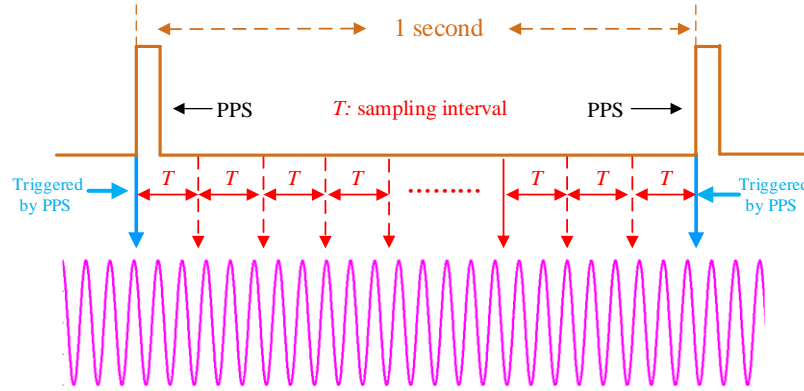


Figure 4.6. Illustration of synchronous sampling for phasor measurement

4.4 Performance evaluation

The aim of this section is to validate the accuracy and effectiveness of E-NCSMD and M-NCSMD in terms of angle and frequency measurement accuracy by means of laboratory and field tests. A comparison between proposed non-contact SMDs and FDRs are also conducted.

4.4.1 Laboratory experiment

It is generally accepted that electric and magnetic field strength in the right-of-way of 500kV transmission corridors is approximately in the range of $1 \mu\text{T}$ to $3 \mu\text{T}$ and 0.3 kV/m to 10 kV/m , respectively[69],[70]. Therefore, in this laboratory experiment, to simulate the condition at the edge

of a power line right-of-way, a $2\ \mu\text{T}$ magnetic field and $5\ \text{kV/m}$ electric field are generated via the magnetic source coil and electric source plate, respectively. The length and width of the source plates are $30.48\ \text{cm}$ and $15.25\ \text{cm}$, respectively. The distance between the two source plates is $2.4\ \text{cm}$.

The Doble F6150 power system simulator with GPS signal synchronization is used to generate AC power for the source plate and source coil. The system setting is shown in Figure 4.7. The experiment results of both kinds of NCSMDs are compared with an FDR, which can achieve frequency and angle accuracy of $0.5\ \text{mHz}$ and 0.02° [16].

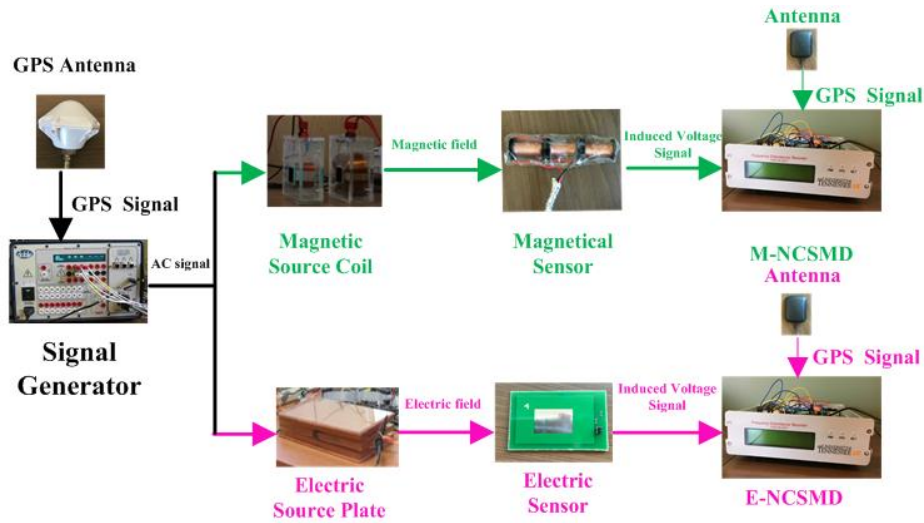


Figure 4.7. Laboratory experiment setup

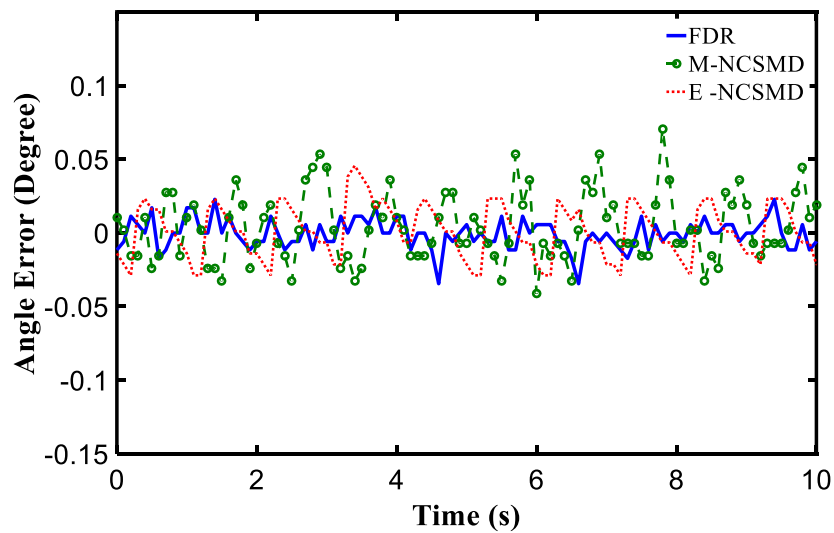


Figure 4.8. Angle measurement results

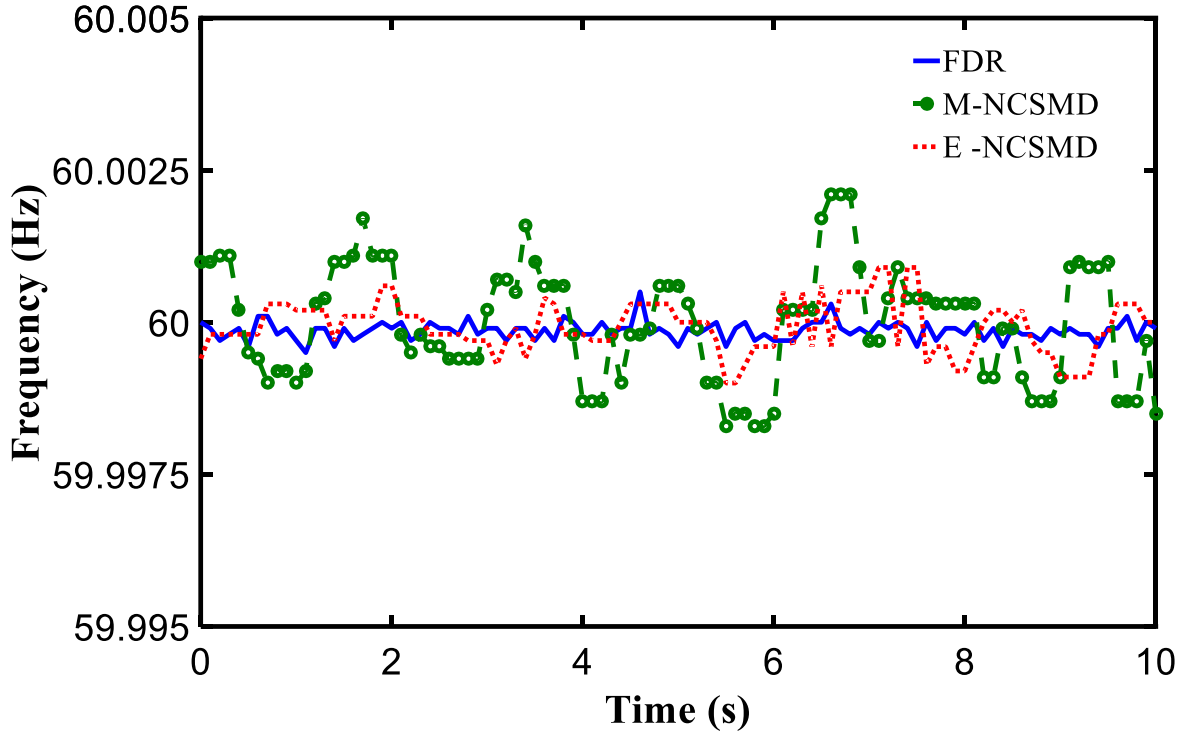


Figure 4.9. Frequency measurement results

The angle and frequency measurement results over an ideal sinusoidal 60 Hz signal from the Doble signal generator are shown in Figure 4.8 and Figure 4.9. According IEEE standard C37.118.1, the limits for frequency and angle measurement on the steady-state condition are 0.005 Hz and 0.57° respectively. The maximum errors of frequency and measurements are listed in Table 4.3. From Figure 4.8 and Table 4.3, the angle error for the E-NCSMD and M-NCSMD are within 0.04° and 0.07° while that of the FDR is 0.03° . The frequency measurement error of the E-NCSMD and M-NCSMD are within $1.82\text{E-}3$ Hz and $2.51\text{E-}3$, respectively, while that of the FDR is $0.78\text{E-}3$ Hz, as seen listed in Table 4.3.

Table 4.3 Maximum error for frequency (Hz) and angle ($^\circ$)

Maximum Error	FDR	E-NCSMD	M-NCSMD
Frequency	5.78E-4	1.82E-3	2.51E-3
Angle	2.88E-2	3.56E-2	7.25E-2

Table 4.4 Standard deviation of frequency error (Hz)

Input signal Frequency(Hz)	FDR	E-NCSMD	M-NCSMD
59.90	3.25E-4	8.25E-4	1.82E-3
59.98	2.33E-4	9.33E-4	1.98E-3
60.00	1.89E-4	3.89E-4	5.98E-4
60.02	3.60E-4	9.60E-4	1.96E-3
60.10	5.28E-4	9.28E-4	1.92E-3

Table 4.5 Standard deviation of angle error (°)

Input signal Frequency(Hz)	FDR	E-NCSMD	M-NCSMD
59.90	1.75E-2	1.88E-2	3.41E-2
59.98	1.54E-2	1.76E-2	2.87E-2
60.00	9.51E-3	2.58E-2	3.25E-2
60.02	1.81E-2	2.57E-2	3.61E-2
60.10	1.91E-2	2.61E-2	3.65E-2

By varying the output frequency of the signal generator, the performance of the E-NCSMD and M-NCSMD can be evaluated under different conditions. The standard deviation (STD) is used to evaluate the frequency and angle error under fixed-frequency conditions. The comparison of frequency and angle results are listed in Table 4.4 and Table 4.5. The standard deviation of the frequency measurement result for the E-NCSMD and M-NCSMD is within 9.60 E-4 Hz and 1.96 E-3 Hz, compared to 5.28E-4 Hz for the FDR. For the angle measurement, the STD for the E-NCSMD and M-NCSMD are within 2.61 E-2° and 3.65 E-2°, compared with 1.91 E-2° for the FDR. The results demonstrate that the E-NCSMD and M-NCSMD are able to achieve almost the same accuracy in frequency and angle measurement as the FDR under steady-state conditions. The total vector error of E-NCSMD and M-NCSMD, as small as about 0.03% and 0.04% respectively, sufficiently complies with IEEE standard C37.118.1, which requires that TVE should be less than 1%.

4.4.2 Field experiment

To further verify the accuracy and effectiveness of frequency and angle monitoring of non-contact SMDs in a field environment, the E-NCSMD and M-NCSMD are tested under 500 kV transmission line in Knoxville, Tennessee. An FDR installed in the same city at distribution level acts as reference for the comparison. Figure 4.10 shows the setup of this field experiment. All the devices are required to sustain stable GPS signals for time synchronization throughout the test so the measurement results can be compared via identical GPS based timestamp. The computers in Figure 4.10 is installed with FNET/Grideye sever client to receive the measurement data from NCSMD via TCP/IP.

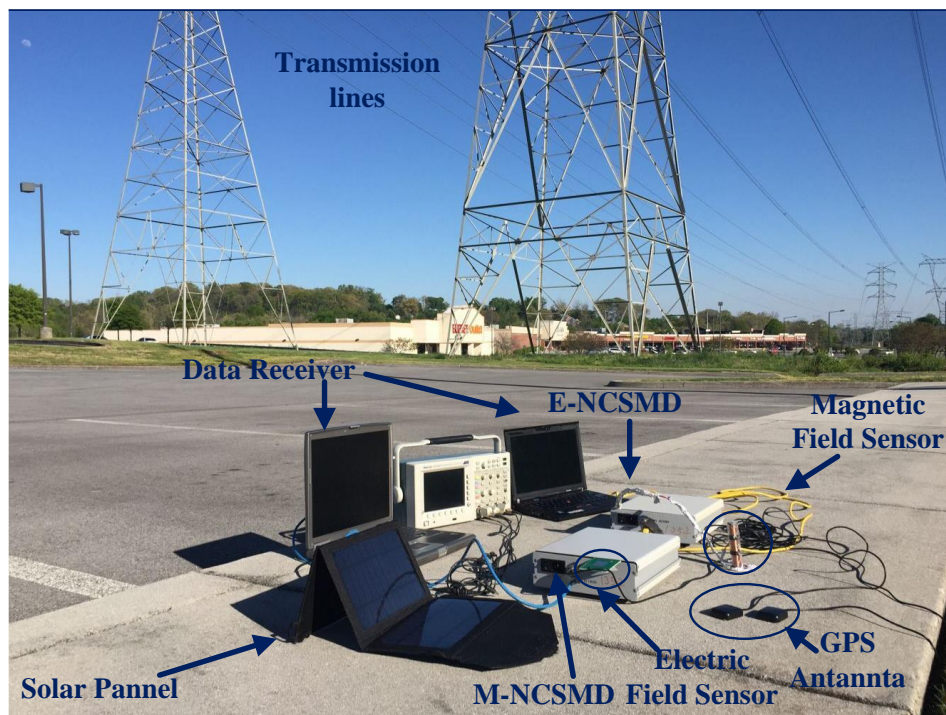


Figure 4.10. Field experiment setup

The waveforms captured by different sensors are illustrated in Figure 4.11. There is an obvious of phase difference between the signal captured by the electric field sensor and magnetic sensor. This is mainly due to the involvement of both inductive and capacitive components in amplifier and analog filters with different time constants, possible phase lag or advance may be introduced. However, this initial angle difference can be considered as constant and thus can be cancelled out. Furthermore, compared with conventional PT, obvious distortion of the signal from the non-contact sensors can be seen. Applying Fast Fourier Transform (FFT) to the signals in Figure 4.11

yields the results of harmonic components analysis shown in Figure 4.12. For the electric sensor, the dominant harmonics components are the 2nd, 3rd, and 4th order. For the magnetic sensor, the 3rd, 5th, and 8th harmonics are the major components. Ref.[50] [71] provide simulation experiments for frequency and angle accuracy under harmonic distortion using RDFT with different window length. The simulation results show that the error for frequency and angle measurements under 10% THD harmonic components within $1.23\text{E-}3$ Hz and $7.21\text{E-}2^\circ$ using a six-cycle RDFT. Since a six-cycle RDFT can achieve satisfactory accuracy under harmonic distortion, it is used in NCSMDs for frequency and angle calculation. Furthermore, there is also DC offset in the signal from the electric field sensor, causing clipping of the signal. The DC offset can be removed since the serial capacitor in the low pass filter can block DC component in the signal. The DC offset for the waveform is reduced from 0.13 to 0.04 p.u.

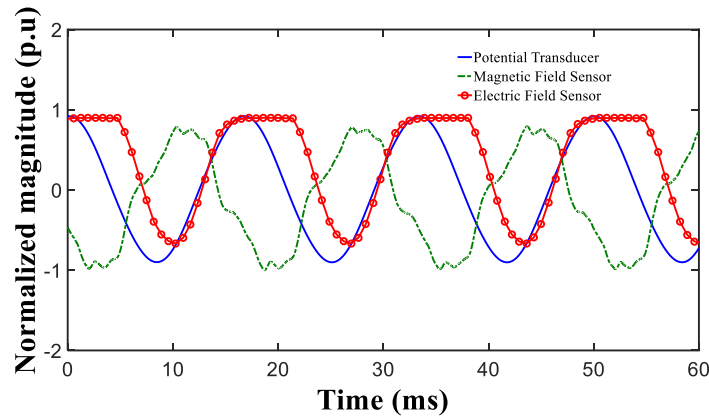


Figure 4.11. Waveforms captured by three types of sensors

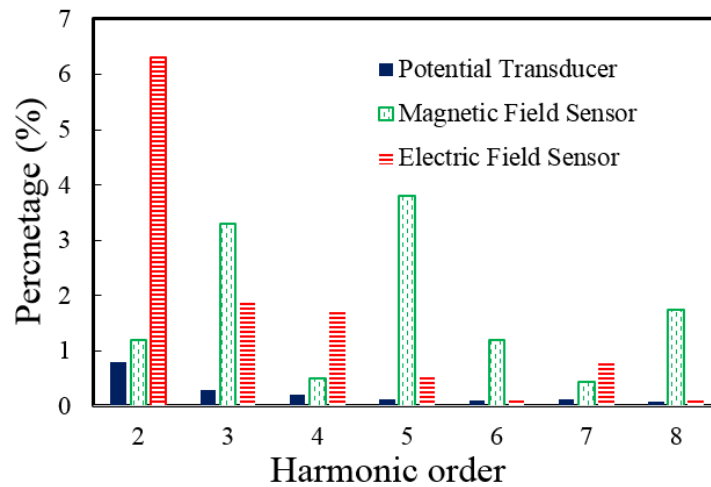


Figure 4.12. Harmonic component analysis

Angle and frequency measurement results for a 250-second window are plotted in Figure 4.13 and Figure 4.14, respectively, at a reporting rate of 10 Hz. The E-NCSMD and M-NCSMD are able to achieve the same accuracy as the FDR except for some small spikes in the frequency result. After compensating by a constant value, phase difference between the FDR and NCSMD are within 0.5° as shown Figure 4.13. The E-NCSMD and M-NCSMD are both able to efficiently capture the trends of frequency and angle change over time. The correlation coefficient of the frequency result between the E-NCSMD and M-NCSMD to the FDR are 0.9760 and 0.9736, respectively. After calibrating the constant time delay, the angle measurement errors are within 0.1° for both the E-NCSMD and M-NCSMD. The non-contact devices and FDR's measurement data have similar distributions in terms of angle and frequency, as shown in Figure 4.15 and Figure 4.16, which demonstrates that frequency and angle measurements of the non-contact devices fall into the same accuracy category as the FDR measurements. The error of frequency and angle measurement of the non-contact SMDs can be obtained using the FDR results as a reference. The maximum and STD of frequency and angle error are listed in Table 4.6. The total vector error of E-NCSMD and M-NCSMD for power grid signal are 0.04% and 0.05% respectively, which sufficiently meets 1% requirement in IEEE synchrophasor standard C37.118.1 and are even more accurate than some commercial phasor measurement units.

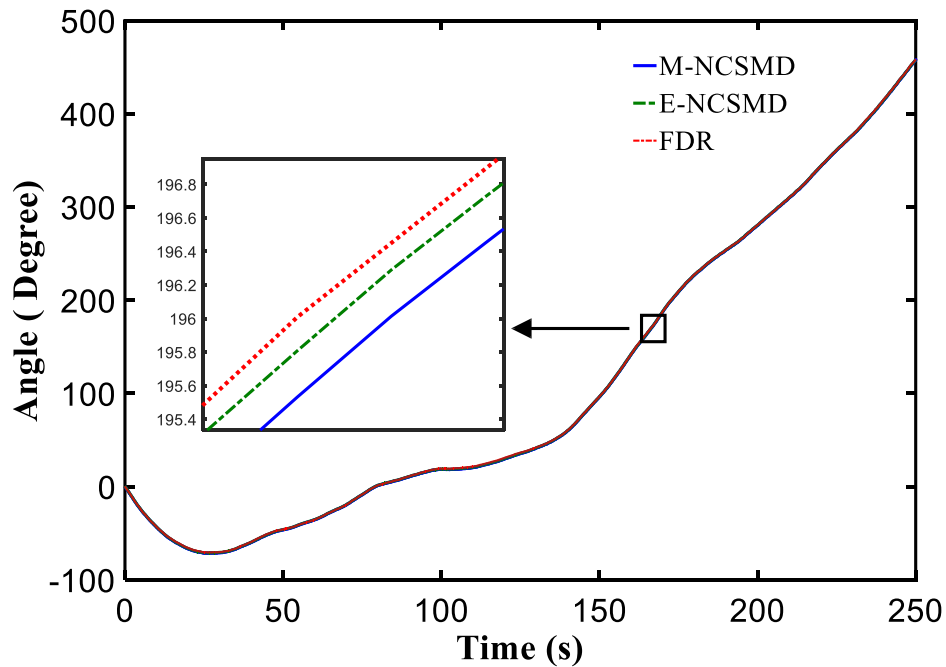


Figure 4.13. Angle measurement results

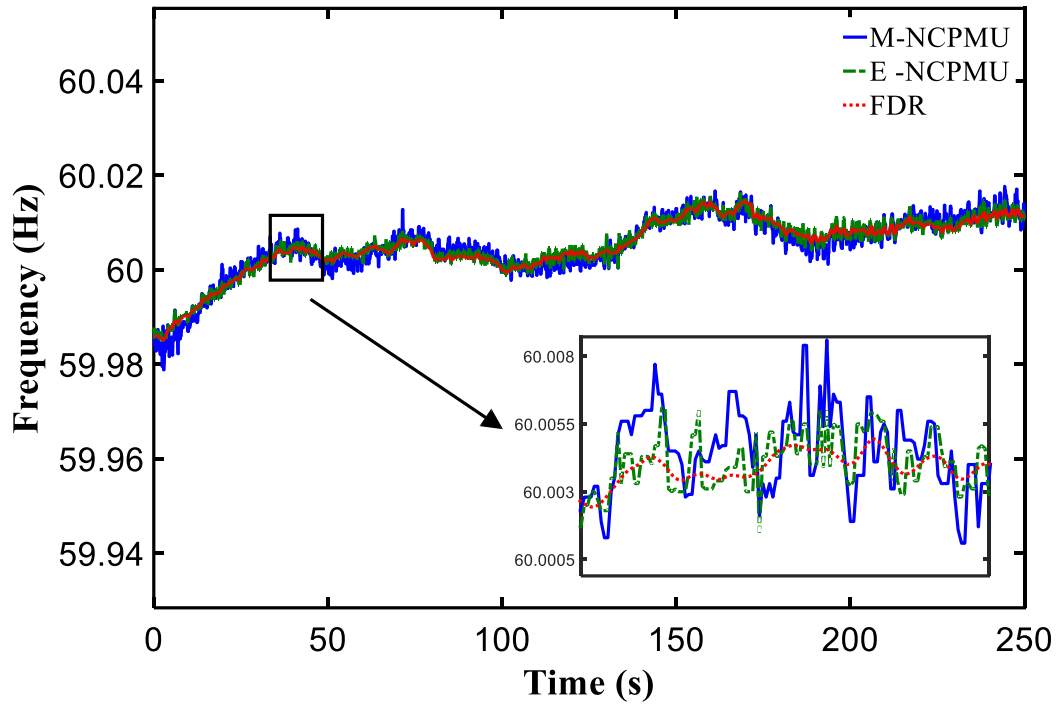


Figure 4.14. Frequency measurement results

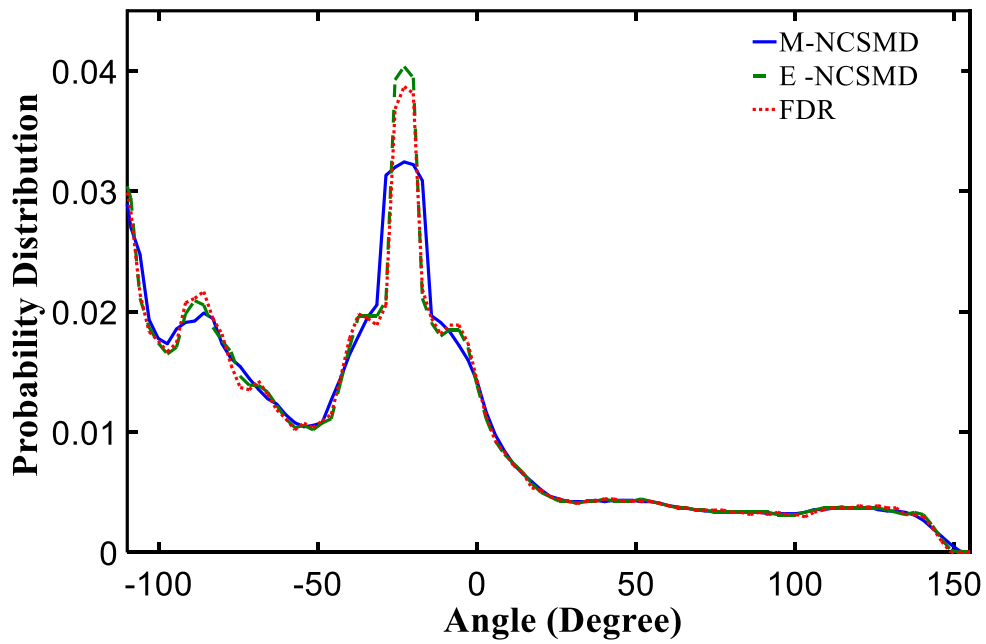


Figure 4.15. Distribution of angle measurement

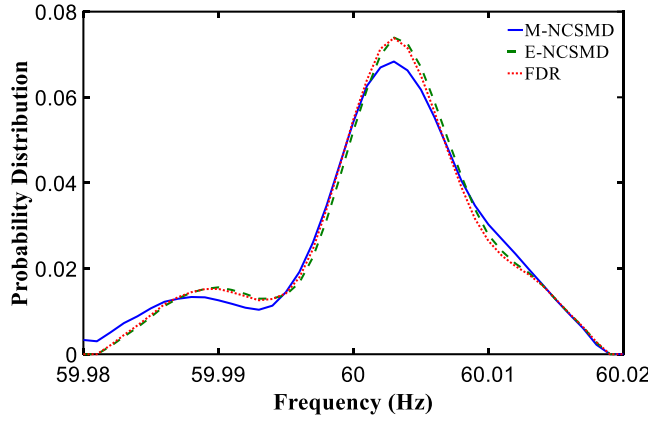


Figure 4.16. Distribution of frequency measurement

Table 4.6 Measurement error

Error	M-NCSMD		E-NCSMD	
	Max	STD	Max	STD
Frequency (Hz)	8.21E-3	7.55E-4	6.31E-3	1.78E-3
Angle (°)	9.78E-2	5.9E-2	8.00E-2	1.61E-2

The main challenge for these non-contact SMDs is to realize non-contact measurement with efficient, compact, and low cost field sensors without impairing the phasor measurement accuracy. Overall, the field test is successful and shows promising results, which demonstrates the non-contact frequency and angle measurement for overhead transmission line are feasible. The non-contact SMD has the advantage of portability, easy installation and low-cost compared with conventional synchrophasors. Nevertheless, at the current stage, the M-NCSMD and E-NCSMD have weakness in the robustness and are more sensitive to the environmental noise and interference compared with traditional CT/PT based synchrophasors. Therefore, to improve the robustness and reliability, a more effective filter is needed for noise reduction in the future for M-NCSMD and E-NCSMD.

4.5 Optical sensor based PMU

4.5.1 Motivation

Due to their high accuracy, PMUs are often used to benchmark the results of critical power

system monitoring functions, e.g., state estimation and stability assessment [72]. As all measurement signals are read from instrument transformers, e.g., potential transformers (PTs) or current transformers (CTs), the performance of these instrument transformers significantly impacts the quality of phasor measurement data [8].

For instance, traditional transformers introduce large instrumentation errors due to inherent deficiencies including temperature and electromagnetic interference (EMI) sensitivity, saturation magnetization and nonlinear induction, etc. Furthermore, as most PMUs are installed at high-voltage substations, the traditional CTs and PTs with oil or sulfur hexafluoride (SF_6) gas requirements for insulation would complicate installation process and bring high maintenance cost [73]. As an increasing number of PMUs are deployed, the necessity to address these issues arises.

Optical sensors technology has proved to be technically mature to the point that they are preferred over their electronic counterparts in numerous applications across the industry[74]. Based on the principle of electrostriction and ampere's law[31], the optical sensors can realize high fidelity of voltage and current signal acquisition by intensity modulation using a non-coherent light source(LED) passing through fiber optic cables without being distorted by any saturation effects. Compared with conventional transformers, optical sensors have advantages in linearity over dynamic range, seismic performance, noise immunity, increased safety, reduced weight and space, and low installation and maintenance costs[31]. Optical sensors enable a high reliability, wide dynamic range sensor for PMUs. In this chapter, the optical sensor technology is incorporated into PMUs. The accuracy of phasor measurements including frequency, angle and amplitude of an optical sensor based PMU is examined via experiment tests.

4.5.2 Performance evaluation of optical sensor based PMU

Frequency disturbance recorder (FDR), which is a member of the PMU family, is used as the testbed in this chapter. FDR originally uses PT to step down power grid signal for phasor measurement, which can achieve measurement accuracy of $5\text{E-}4$ Hz for frequency, $1\text{E-}3$ radian for angle, and $5\text{E-}2$ V for amplitude. To verify the effectiveness of the optical sensor, one FDR is modified to connect to an optical sensor, referred to as OPS-FDR. The power grid signal is sensed by an optical sensor head connected with optical fibers. A smart controller is used to generate a beam of light for optical fibers and realize the optical-electric signal conversion using a photodetector [31]. The OPS-FDR uses output analog signal from the smart controller instead of PT to perform phasor calculation. Another traditional FDR with PT, referred to as a PT-FDR, is

simultaneously running for comparison. The photo of the experimental setup is shown in Figure 4.17. It is noted that both FDRs are required to receive stable GPS signals for time synchronization throughout the tests, thus measurement data transmitted to FNET/GridEye server can be aligned together for accuracy comparison based on unified GPS time stamp.

A Fluke 5080A calibrator, with frequency resolution 6 E-3 Hz is used to generate simulated signals for both PT-FDR and OPS-FDR. By changing the output frequency of the Fluke 5080A calibrator, the performance can be evaluated under different conditions. Standard deviations (STD) of frequency measurement errors are given in Table 4.7. Frequency errors of both FDRs are less than 1 E-3 Hz , which meet the IEEE standard. Furthermore, measurement accuracy of the two FDRs is very close to each other, which means optical sensor can provide equivalently accurate analog signal for synchronized frequency measurement [9]. The error of OPS-FDR is as small as about 8 E-3 Hz , which may be explained by the hardware resolution limit posed by a 14-bit ADC used in FDRs.

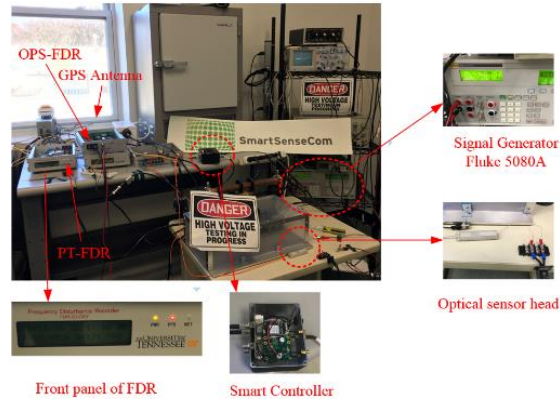
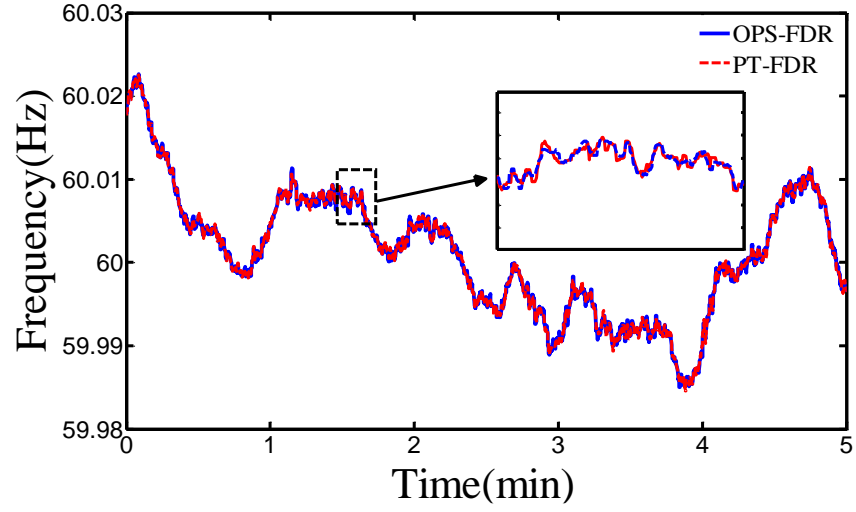
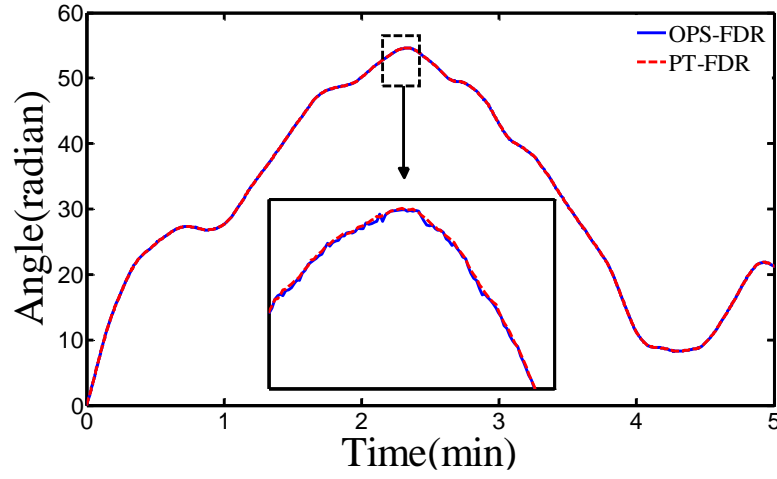


Figure 4.17. Experiment setup

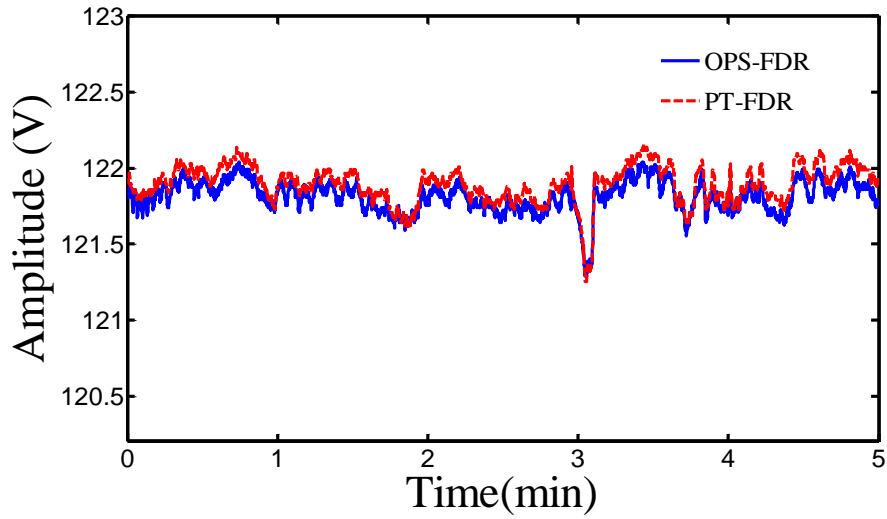
To further the accuracy and effectiveness of optical sensor for phasor measurement, OPS-FDR is tested using real ambient power grid signal. The results of frequency, angle, and voltage magnitude measurements are shown in Figure 4.18(a)-(c). It can be seen in Figure 4.18 that OPS-FDR has the ability to synchronously capture the trends of power grid frequency, angle and amplitude over time as PT-FDR. The error of phasor measurement of OPS-FDR can be obtained using PT-FDR results as a reference. Maximum and STD of frequency, angle and amplitude error are listed in Table 4.7. STD of OPS-FDR are 9.03 E-4 Hz for frequency, 6.38 E-3 radian for angle and 6.73 E-2 V for amplitude, respectively. Total vector error (TVE) of OPS-FDR is as small as 0.31%, which is sufficient to fulfill the 1% requirement of IEEE synchrophasor standard.



(a) Frequency



(b) Angle



(c) Voltage Magnitude

Figure 4.18. Test results with real power grid signals

Table 4.7 Frequency errors of PT-FDR and OPS-FDR (Hz)

Frequency (Hz)	PT-FDR	OPS-FDR
59.95	7.79E-4	7.01E-4
59.98	6.64E-4	6.82E-4
60.00	5.58E-4	6.73E-4
60.02	6.71E-4	6.79E-4
60.15	8.82E-4	8.86E-4

Table 4.8 Accuracy of OPS-FDR with power grid signal

Frequency (Hz)	Angle (rad)	Amplitude (V)	TVE(%)
9.03 E-4	6.38 E-3	6.73 E-2	3.1 E-1

4.6 Conclusion

In this chapter, the design and implementation of two types of non-contact synchronized measurement devices, M-NCSMD and E-NCSMD, were presented. Laboratory and field experiments verified the effectiveness and accuracy of the angle and frequency measurements from both devices. Unlike traditional SMD, the proposed devices are portable and flexible, greatly broadening the synchrophasor family. Furthermore, these devices can reduce manufacturing and installation costs dramatically, facilitating wide application of future wide area phasor monitoring of the transmission line network. Further work includes further improving the reliability and accuracy of both devices under noisy conditions via more advanced sensor integration, magnitude measurement realization, dynamic performance evaluation, waterproof design, wireless communication, lightning protection, and field tests in hostile weather and locations.

In this chapter, optical sensor was successfully implemented on a synchronized phasor measurement unit and its performance was evaluated and verified using experiments. It was demonstrated that optical sensor based PMU is capable to achieve stable and accurate phasor measurement. With further reduced manufacturing cost, optical sensors can be used for wide applications in future PMUs for measuring signal acquisition.

Acknowledgment

This chapter is, in part, a reprint of the material in the papers: Wenxuan Yao, Yingchen Zhang, Yong Liu, Micah Till, Yilu Liu, “Pioneer Design of Noncontact Synchronized Measurement Devices Using Electric and Magnetic Field Sensors”. *IEEE Transactions on Smart Grid*, accepted, in press and Wenxuan Yao, Wenxuan Yao, David Wells, Daniel King, Andrew Herron, Thomas King, Yilu Liu, “Utilization of Optical Sensors for Phasor Measurement Units”, *Electric Power Systems Research*, 2018, 156:12-14

Chapter 5 Power Grid Monitoring on Mobile Platform

5.1 Introduction

Phasor measurement units (PMUs) have been increasingly deployed as essential elements of wide area monitoring system, providing an innovative technology for real-time monitoring of the operational state of entire power systems and significantly improving power grid dynamic observability.

However, traditional PMUs have several limitations, especially on the conditions of distribution level power grid, e.g., microgrids. First, most of PMUs are installed in substations at the transmission level with three-phase connection, posing high requirements for installation and maintenance[75]. Second, the manufacturing and installation costs of current PMUs are too high. For example, current commercialized PMUs are sold as dedicated devices at prices between 6,000 USD and 15,000 USD per unit, depending on the specifications[76]. The high cost will reduce end-users', e.g., individual households, incentives of having phasor monitoring devices at their energy home system and consequently impede the wide deployment across the power grid, especially in distribution level power grid. Third, in some remote areas, far from any substation or microgrid operated in either grid connected mode or islanded mode, it is difficult to install and maintain a PMU due to the lack of facilities and high installation cost [77]. Fourth, as most of the current PMU cannot save the measurement data locally, the long distance between the measurement point and the data servers, e.g., phasor concentrator centers (PDCs), will lead to potential threats in data missing due to failure of data communication or cyber-attack[30]. However, it is critical to continually monitor the phasor state in such areas to intercept any potential problem before it reaches the point of no return e.g., a generation trip [33] or islanding process [34].

To overcome the aforementioned issues, one potential solution is to realize the power grid phasor measurement with the integration of a low cost mobile device (MD), e.g., personal smartphone, at single phase distribution level power grid. Current smartphones can achieve high computation speeds to execute real-time measurement algorithm. Implementing the phasor measurement on MDs will facilitate widespread deployment with advantages in the aspects of low cost, data visualization and analytics function, upgrade flexibility and built-in communication channels[77].

Development of phasor measurement MD, however, is challenging due to the requirements of accurate time synchronization, high-resolution sensing, and real-time data calculation.

First, one fundamental question is to realize the high accurate time synchronization for sampling control on the MD. Taking advantage of WI-FI accessibility in MD, synchronized power grid frequency measurement was developed based Network Time Protocol (NTP) timing signal [78][79]. Theoretically, the NTP can achieve timing accuracy in the order of 0.1 milliseconds, which is sufficient for phasor measurement. Unfortunately, practical accuracy of NTP time is only up to 15 milliseconds due to the uncertainty of network delay or network instability, corresponding to an unacceptable angle error of 330° in a 60 Hz system. A 200 Hz Primary Synchronization Signal (PSS) in the 4G Long Term Evolution (LTE) cellular signal is harvested for time synchronization [80]. However, the slope of the rising edge of the PSS pulse is flat and can be affected by the strength of the signal, which influences the reliability of synchronization. To meet the requirements in IEEE standard C37.118.1, a more accurate and stable time synchronization strategy needs to be explored on the MD utilizing GPS signal.

Second, power grid phasor can be measured using a recursive Discrete Fourier Transform (RDFT) method first proposed by A.G. Phadke and J. S. Thorp [72]. However, significant errors will arise due to the spectral leakage issue of RDFT on the off-nominal conditions [81]. To address this issue, a least square estimation and resample calculation are used for frequency accuracy enhancement. Moreover, the systematic errors of the single-phase angle measurement are reduced by perform quasi-positive-sequence DFT and DC offset compensation using measured frequency. The algorithm is then implemented in the MD for phasor estimation.

Therefore, this chapter introduces the development of single-phase power grid phasor measurement on a MD integrated with GPS time synchronization, enabling its plug-and-play feature and minimizing manufacturing cost and installation effort. The effectiveness and accuracy of the proposed device are verified via experiment result. The proposed device can work in tandem with conventional synchrophasor measurement devices to supplement existing wide area power grid phasor monitoring. The outcome of this chapter provides a potential solution to make the phasor measurement device below 300 USD per unit, which is promising for wide deployment of phasor measurement in household installation. Furthermore, as an advanced power grid situational awareness tool, it also can be future used as grid-edge device for smart energy management or load

control in distribution level, helping to interpret the power grid operation status and take proactive measures to monitor power grid disturbance and outage.

5.2 Phasor measurement on mobile device

In this section, the overview of hardware and software designs for phasor measurement on Android™-based mobile device are presented.

5.2.1 Overview of hardware design

The hardware design of whole system is shown in Figure 5.1. It mainly includes, a data acquisition board (DAQB) for synchronized sampling, a voltage regulator for DC power supply, and an Android™-based smartphone for phasor estimation. In our prototype development, the Nexus S smartphone installed with android operation system (OS) version 4.4 and equipped with 1 GHz CPU and a 512 MB memory is used. The DAQB utilizes PPS signal from a GPS receiver for sampling synchronization.

For the signal input channel, a Current-type Microminiature Voltage Transformer (CMVT) is used to scales down the single phase voltage of the power grid V_{in} to fit the input ranges of the Analog to Digital Converter (ADC) as illustrated in as shown in Figure 5.2. The magnitude of output voltage V_{out} can be expressed as

$$V_{out} = TR \times V_{in} \times \frac{R_2}{R_1} \quad (5.1)$$

where TR is turn ratio between the primary and secondary windings. R_3 and C_1 forms a low-pass anti-aliasing filter with cutoff frequency $\frac{1}{2\pi R_3 C_1}$ for rejecting high-frequencies noise.

The single-phase power grid signal is fed into a potential transformer for signal isolation and condition. Then it is amplified and filtered by a low-pass filter with a cut-off frequency of 1000 Hz for rejecting high-frequency interference. Because the sample intervals of a successive approximation register (SAR) ADC can be directly controlled by the timer in microprocessor while sigma-delta ADC cannot, SAR ADCs are widely used in PMUs for synchronized sampling. The DAQB uses 16-bit SAR ADC LTC1609 for sampling. An Arduino board with a microprocessor ATmega328 with main clock 16 MHz is used in DAQB for receiving both PPS and UTC signals from a GPS receiver, controlling ADC sampling and sending the raw digital data along with UTC time to the smartphone. The rising edges of the PPS will be detected through an external interrupt

in the microprocessor. A sampling command will be sent in this interrupt to initiate a synchronization cycle per second. The bidirectional data communication between the microprocessor and the mobile device is realized by a USB host controller MAX3421E [82]. The microprocessor behaves as USB master when communicating with the USB host controller. The smartphone, as USB slave, passively receives sampled digital data and UTC time index and performs the phasor estimation using the received data.

The PCB of the data acquisition board is shown in Figure 5.3 and the prototype of the smartphone based device can be seen in Figure 5.4. The shell of the data acquisition board is built using 3D-printer.

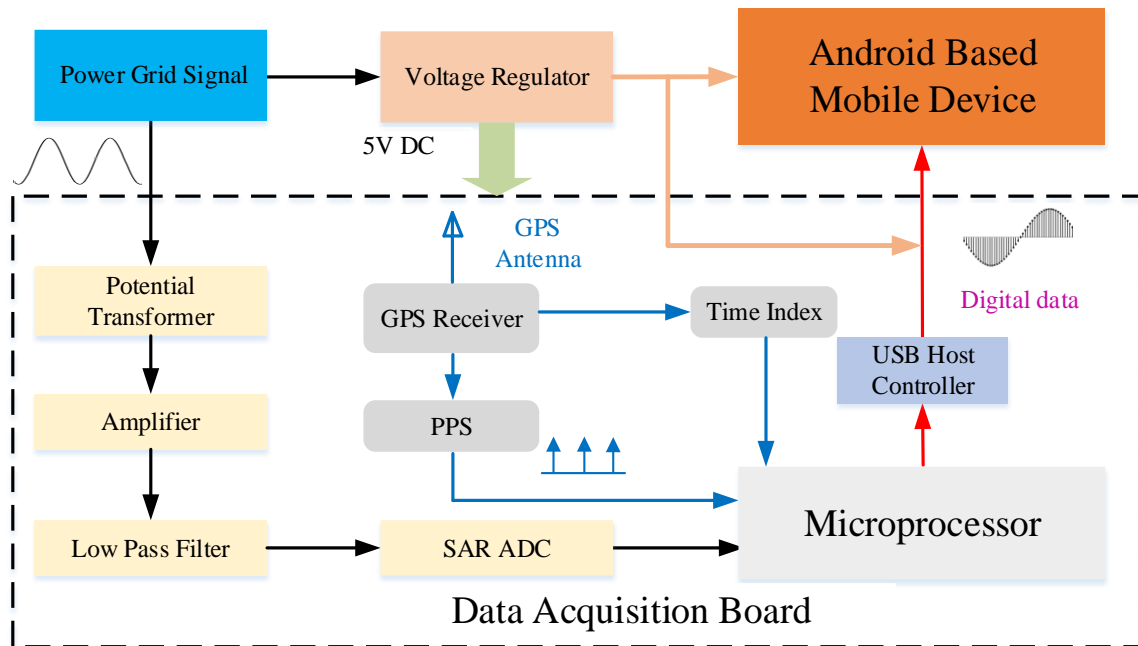


Figure 5.1. Hardware design of the proposed mobile device

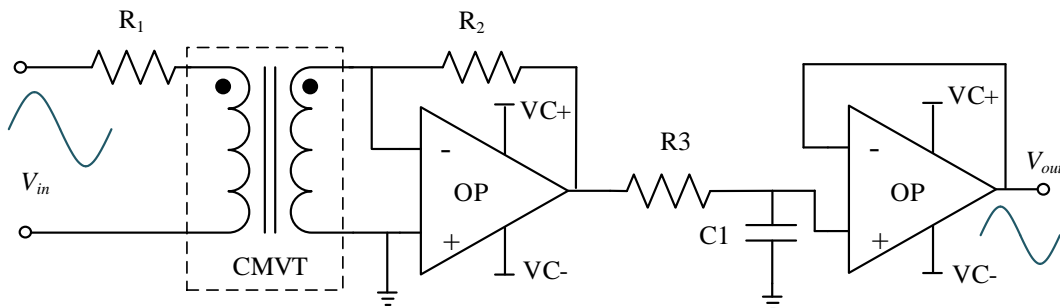


Figure 5.2. Arduino Uno board

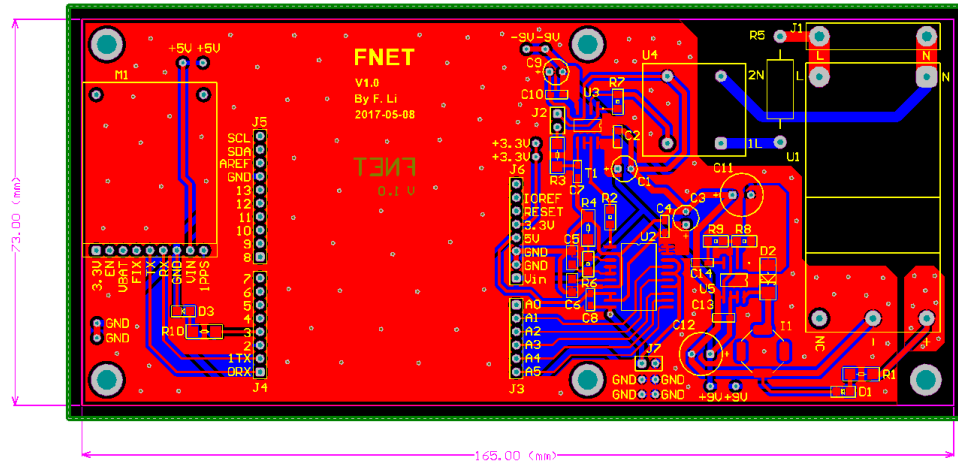


Figure 5.3. PCB of data acquisition board



Figure 5.4. Prototype of data acquisition board

5.2.2 Overview of software design

The software designs for DAQB and Android smartphone are illustrated in Figure 5.5. For the DAQB, the analog to digital conversion is triggered by PPS and the sampling interval within two adjacent PPS is controlled by a Timer Period Register (TPR) in the microprocessor. To compensate the sampling time error caused by the division remainder of timer parameter and system clock drifts, a self-adaptive sampling strategy is proposed and discussed in details in Section I[17]. Each sampling cycle, the microprocessor send a sampling command and read sampled data from ADC LTC1609. The microprocessor also continuously sends latest sampled data per 0.1 seconds to the smartphone in one data package via USB communication. To avoid any data loss, there are two arrays working alternately for sampled data receiving and sending.

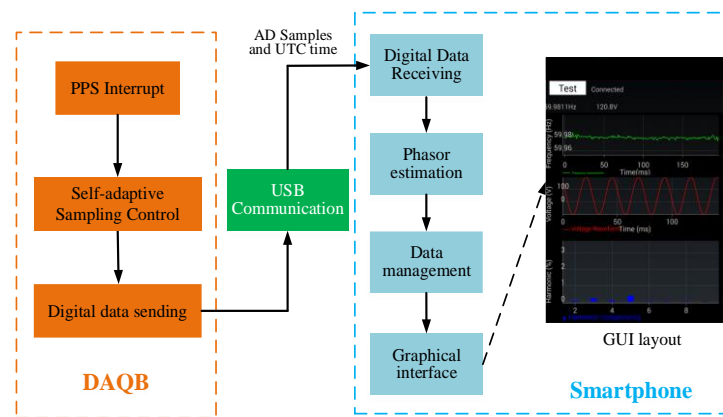


Figure 5.5. Illustration of software designs of the mobile device

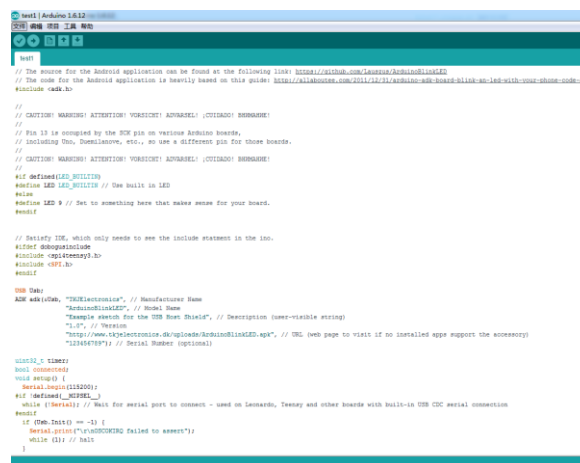


Figure 5.6. Arduino development environment

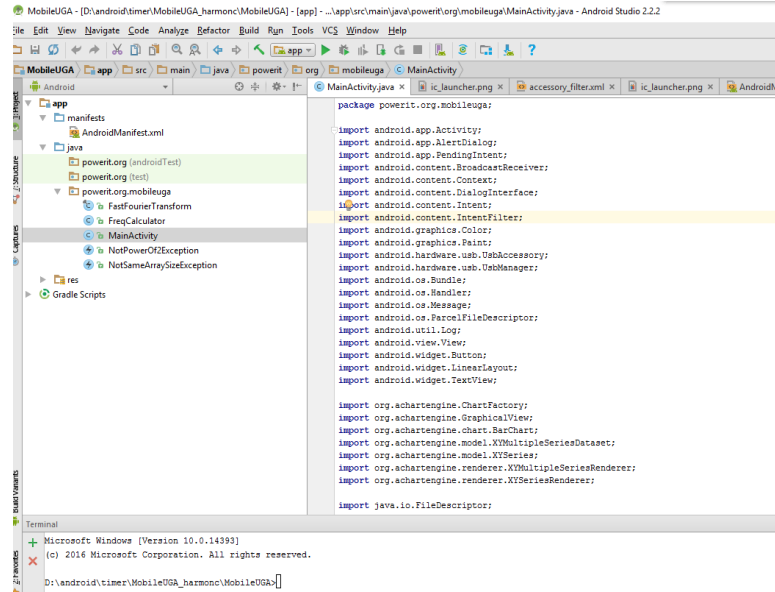


Figure 5.7. Software development on Android Studio

The APP is developed on the android studio platform as illustrated in Figure 5.6. The software developed at android based smartphone is shown in Figure 5.7.

For the smartphone, a phasor estimation application is developed in android OS including a digital data receiving component, a phasor estimation component, a Graphical User Interface (GUI) component and a data management component. Once installing the application, the USB accessory connection status is continually monitored, acting as “plug-and-play” mode, which means when the smartphone is connected to the DAQB with a successful “handshake”, the whole application will start to run automatically. After initialization, the data receiving component starts to receive digital sampled data from the DAQB and then phasor estimation component calculates phasor parameters including frequency, angle, and amplitude. The measurements stamped by UTC time indexes from GPS receiver are save to a database on the local memory of the smartphone for data backup and then uploaded to remote data server via wireless network in data management component. Finally the latest phasor measurement results and real-time waveform are visually displayed at the smartphone screen via executing the GUI component.

5.2.3 GUI design on mobile platform

The power quality measurement results and its real-time waveform are displayed on the screen for user interaction.

For the Graphical User Interface (GUI), we wanted something clean and simple. We built the GUI using the Android Studio IDE using the Java language. A way was needed to plot and graph our data in real-time so the external library, AChartEngine, and its existing APIs were utilized to allow this. The more difficult portion of the coding was implementing the algorithms and having the application receive this data and display it in real-time. Below is a figure that shows what our data and application look when functioning and reading data. The screenshot is shown in Figure 5.7. After pushing the test bottom, the smartphone will send sampling command to Arduino board and smartphone will start power quality measurement. It will show the value of frequency and amplitude for the power grid signal. Moreover, the app has three charts to display the frequency measurement, raw waveform, and harmonic distortion using different colors. The harmonic calculated results are shown using a bar chart. The height of each bar reflects the percentage of harmonic components from 2nd to 5th order. The harmonic results are refreshed every 2 seconds while frequency measurements are updates 5 times every second.

Here it can be seen that we are displaying the frequency, voltage sinusoidal, and the harmonic components. These graphs will change with time and will be displayed accordingly. Measurement Algorithm

5.2.4 Phasor calculation

Given N data points of signal $\{x_i\}$ per cycle $i \in [1 N]$ obtained from the DAQB, the phasor $\bar{X}_{(0)}$ of the signal $\{x_i\}$ can be expressed as

$$\bar{X}_{(0)} = \frac{1}{\sqrt{2}}(X_0^c + j \cdot X_0^s) \quad (5.2)$$

where j is the imaginary unit. $X_{(0)}^c$ and $X_{(0)}^s$ are the real and imaginary parts respectively, which can be calculated via a full cycle DFT

$$X_{(0)}^c = \frac{2}{N} \sum_{i=1}^N x_i \cos\left(\frac{2\pi i}{N}\right) \quad (5.3)$$

$$X_{(0)}^s = \frac{2}{N} \sum_{i=1}^N x_i \sin\left(\frac{2\pi i}{N}\right) \quad (5.4)$$

To reduce computational overload, for the successive \bar{X}_{i+1} phasor for of incoming data x_{i+1} ($i > 0$), the recursive DFT can be applied according to following forms:

$$\bar{X}_{(i+1)} = \bar{X}_i + j \frac{\sqrt{2}}{N} (x_{i+1} - x_{i+1-N}) \exp(-j \frac{2\pi i}{N}) \quad (5.5)$$

Thus, the new real and imaginary components can be expressed as

$$X_{(i+1)}^c = X_i^c + \frac{2}{N} (x_{i+1} - x_{i+1-N}) \cos\left(\frac{2\pi i}{N}\right) \quad (5.6)$$

$$X_{(i+1)}^s = X_i^s + \frac{2}{N} (x_{i+1} - x_{i+1-N}) \sin\left(\frac{2\pi i}{N}\right) \quad (5.7)$$

It can be seen from (4) to (6), only a few multiplication, addition and subtraction operations are needed to compute the new phasor after initialization.

The amplitude A_i and angle θ_i of the i th phasor can be obtained by

$$A_i = (X_{(i)}^c)^2 + X_{(i)}^s)^2)^{\frac{1}{2}} \quad (5.8)$$

$$\theta_i = \tan^{-1}\left(\frac{X_{(i)}^c}{X_{(i)}^s}\right) \quad (5.9)$$

The frequency can be computed by estimating the change of rate of the angle dataset for the points in the truncated window. Assuming the angle varies following a polynomial function with respect to the sampling number, m th sample in the angle dataset can be expressed as

$$\theta_{(m)} = \sum_{i=1}^p \alpha_i m^{i-1} \quad (5.10)$$

where α_i are the coefficients for the $(p-1)$ th order polynomial function. Converting equation (10) into matrix form, it can be expressed as

$$\boldsymbol{\theta} = \boldsymbol{\alpha} \mathbf{M} \quad (5.11)$$

where angle column matrix $\boldsymbol{\theta} = [\theta_1 \cdots \theta_m \cdots \theta_M]$. $\boldsymbol{\alpha} = [\alpha_1 \cdots \alpha_m \cdots \alpha_M]$ is unknown coefficient column matrix, representing the characteristic of angle change. M is the length of angle dataset for frequency calculation. \mathbf{M} is a prior knowledge matrix with size of $M \times p$ whose element is satisfying $m_{i,j} = i^{j-1}$. It is noted in (5.11) that the matrix \mathbf{M} is constant and each element in $\boldsymbol{\theta}$ can be obtained from (5.9). To obtain the unknown $\boldsymbol{\alpha}$, a least-square method (LSM) is adopted to approximate best fit for a dataset $\boldsymbol{\theta}$ by solving the following pseudo-inverse equation

$$\boldsymbol{\alpha} = [\mathbf{M}^T \mathbf{M}]^{-1} \mathbf{M}^T \boldsymbol{\theta} \quad (5.12)$$

Therefore, the first calculated frequency delta $\Delta f_{(1)}$ can be obtained as

$$\Delta f_{(1)} = \frac{1}{2\pi} N f_0 \left(\sum_{i=1}^p (i-1) \alpha_i m^{i-2} \right) \quad (5.13)$$

where f_0 is the nominal frequency. Therefore the first estimated frequency f_1 can be computed by

$$f_1 = f_0 + \Delta f_{(1)} \quad (5.14)$$

5.2.5 Frequency accuracy enhancement

To enhance the performance of frequency measurement under off-nominal condition, f_1 will be regarded as the nominal frequency of the re-sampling process. Since the sampling rate of ADC in MES is fixed, in order to keep constant sampling number per cycle that angle increments at the speed of $2\pi/N$, the input signal is resampled via interpolation as illustrated in Figure 5.8. Defining the origin samples x_i and x_{i+1} are

$$x_i = AP \sin \varphi \quad (5.15)$$

$$x_{i+1} = AP \sin(\varphi + \delta) \quad (5.16)$$

where AP is the amplitude of the input signal; φ is an instantaneous angle for x_i . δ is angle difference between two samples at the frequency f_1 , satisfying $\delta = 2\pi f_1/(N f_0)$. When $f_1 = f_0$, the δ is equal to $2\pi/N$. To correct δ to be $2\pi/N$ when $f_1 \neq f_0$, a resample process is performed.

Assuming the re-sample point xs_i is between samples x_i and x_{i+1} , the value of the xs_i can be expressed as

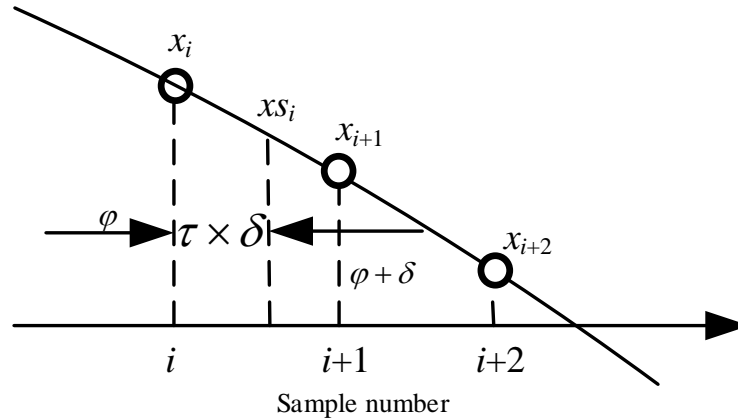


Figure 5.8. Illustration of re-sampling procedure

where τ is the fractional number between 0 and 1 representing relative distance of resampled point xs_i to x_i and x_{i+1} , which can be obtained by

$$\tau = i \times \frac{f_0}{f_1} - Fl\left(i \times \frac{f_0}{f_1}\right) \quad (5.17)$$

where $Fl()$ denotes the function that rounds a non-integer down to the nearest integer.

Expanding(5.15) to (5.16) using trigonometric identifies, xs_i can be calculated as

$$xs_i = x_i \cos \tau \delta + (x_{i+1} - x_i \cos \delta) \frac{\sin \tau \delta}{\sin \delta} \quad (5.18)$$

Applying above recursive DFT algorithm on resample data $\{xs_i\}$, the second calculated frequency measurement f_2 is

$$f_2 = f_1 + \Delta f_2 \quad (5.19)$$

where Δf_2 is the second frequency delta. The f_2 will be output as final calculated frequency in the MES.

5.2.6 Single-phase angle accuracy enhancement

Unlike conventional PMUs, which use three phase input signal on transmission level, the smartphone performs phasor measurement using single-phase signal. It is reported in Ref.[37] that a systematic angle error is introduced under off-nominal conditions for single phase angle measurement. The two components for angle errors consist of a fixed DC offset and a sinusoidal variation. The fixed DC offset, OF , which is constantly proportional to the frequency excursion, can be effectively compensated after the frequency delta Δf_2 is obtained

$$OF = \frac{(N-1)\pi\Delta f_2}{Nf_0} \quad (5.20)$$

To reduce the sinusoidal variation of angle measurement, another two phase signals are generated in simulation from the single-phase signal under an assumption of a balance system. The recursive DFT is then applied to the positive sequence calculated from simulated three-phase signals. Simulation results in [37] demonstrated that attenuation effect on sinusoidal angle measurement is less than 0.1% with 50 mHz frequency deviation.

5.2.7 Harmonic distortion calculation

Because of the asynchronous sampling, the spectral lines deviate by an unknown displacement from the exact peaks corresponding to the harmonic components. Thus, the spectral lines do not correspond exactly to the harmonic components, known as picket fence effect. Figure 5.9 depicts the magnitude spectrum of a cosine signal under asynchronous sampling. We consider the sampled

harmonic signal with constant window length N

$$x(nT_s) = x(t)|_{t=nT_s} = \sum_{h=1}^H A_h \sin(2\pi f_h nT_s + \varphi_h) \quad (5.21)$$

For simplicity, the influences of interharmonics are neglected, The DFT of the windowed samples $x(n)w_{Ka-p}(n)$ with length N_i can be written as follows:

$$X(k) = \sum_{h=1}^H \frac{A_h}{2j} \left[e^{j\varphi_h} W_{K-p}(k - k_h) - e^{-j\varphi_h} W_{K-p}(k + k_h) \right] \quad (5.22)$$

The second term in (5.22) represents the imaginary part of the spectrum. The complex spectrum of the h th spectral line representing the h th harmonic can be obtained

$$X(\xi_h) = \frac{A_h}{2j} e^{j\varphi_h} W_c(\xi_h - k_h), \quad \text{for } \xi_h = 0, 1, \dots, N_i - 1 \quad (5.23)$$

Assuming the two peak spectral lines corresponding to the h th harmonic are located at l_{h1} and l_{h2} ($l_{h2} = l_{h1} + 1$, $l_{h1} < k_h < l_{h2}$). We define $y_1 = |X(l_{h1})|$ and $y_2 = |X(l_{h2})|$.

$$y_1 = |X(l_{h1})| = |A_h| \cdot |W_c(2\pi(l_{h1} - k_h)/N_i)| \quad (5.24)$$

$$y_2 = |X(l_{h2})| = |A_h| \cdot |W_c(2\pi(l_{h2} - k_h)/N_i)| \quad (5.25)$$

The ratio of the two magnitudes y_1 and y_2 can be used for interpolated algorithm.

Since $0 \leq k_h - l_{h1} \leq 1$, we define a symmetrical coefficient τ as

$$\tau = k_h - l_{h1} - 0.5, \quad \text{for } -0.5 \leq \tau \leq 0.5 \quad (5.26)$$

y_1 and y_2 are both an even and symmetrical on τ , which can be expressed as

$$y_1 = |X(l_{h1})| = |A_h| \cdot |W_{Ka-p}(2\pi(-\tau + 0.5)/N_i)| \quad (5.27)$$

$$y_2 = |X(l_{h2})| = |A_h| \cdot |W_{Ka-p}(2\pi(-\tau - 0.5)/N_i)| \quad (5.28)$$

A coefficient ν as a function of τ can then be defined as

$$\nu = (y_2 - y_1)/(y_2 + y_1) \quad (5.29)$$

Substituting (5.27) and (5.28) in (5.29), ν can be expressed as

$$\nu = g(\tau) = \frac{|W_{Ka-p}(2\pi(-\tau + 0.5)/N_i)| - |W_{Ka-p}(2\pi(-\tau - 0.5)/N_i)|}{|W_{Ka-p}(2\pi(-\tau - 0.5)/N_i)| + |W_{Ka-p}(2\pi(-\tau + 0.5)/N_i)|} \quad (5.30)$$

A polynomial fitting procedure based on the least-square curve-fitting method is used in this

chapter. Suppose that the data points are (ν_i, τ_i) , where $i = 0, 1, \dots, L-1$, the number of the pairs of experimental data L , the independent variable ν_i , and the dependent variable τ_i . The fitting polynomial $\tau = g^{-1}(\nu)$ has the deviation (error) from each data point. According to the least squares method, the best fitting polynomial should satisfy

$$\min \|\gamma\|_2^2 = \min \sum_{i=0}^{L-1} [g^{-1}(\nu) - \tau_i]^2 \quad (5.31)$$

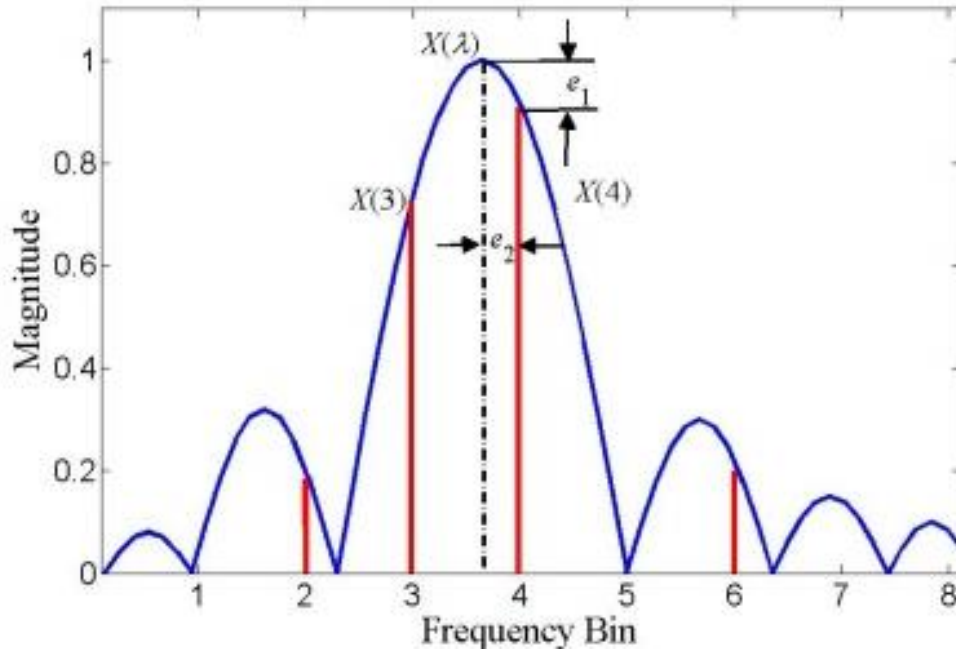


Figure 5.9. Spectral leakage and picket fence effects of FFT due to asynchronous sampling

The polynomial $g^{-1}(\nu)$ with the order J is expressed as

$$\tau = g^{-1}(\nu) \approx a_1\nu + a_2\nu^2 + a_3\nu^3 + \dots + a_J\nu^J \quad (5.32)$$

Then, the polynomial $g^{-1}(\nu)$ should also satisfy:

$$F = \min \sum_{i=0}^{L-1} \left(\sum_{j=0}^{J-1} a_j \nu_i^j - \tau_i \right)^2 \quad (5.33)$$

where F is the sum of the square of deviations. Taking the derivative of F with respect to a_j and setting them to zero gives the following equation:

$$\frac{\partial F}{\partial a_j} = 2 \sum_{i=0}^{L-1} \left(\sum_{j=0}^{J-1} a_j \nu_i^j - \tau_i \right) \nu_i^j = 0 \quad (5.34)$$

then the coefficients a_j can be determined by fixed equation in the form of (5.34). The order J of

the polynomial $\tau = g^{-1}(\nu)$ should be determined according to the accuracy requirement. The order J of the polynomial should be determined according to the accuracy requirement. Simulation results show increasing J until 5 or 7 has a significant effect on the resolution and for J larger than 7, the influence is not noticeable and just leads to a larger amount of calculations [38].

Based on the preceding equations, the interpolation processing can be summarized as the two following steps in Matlab:

1) Take L numbers ($L > 100$) of τ in the range from -0.5 to 0.5, thus the value of ν can be obtained from (5.29)

2) Call MATLAB function polyfit (ν_i, τ_i, J) to compute the inverse-fitting, and the coefficients of the polynomial $g^{-1}(\nu)$ can be obtained.

The parameters f_h , A_h , and ϕ_h of the signal can be obtained by using the following formulae after the τ is determine by two maximum spectral lines and the fitting polynomial $g^{-1}(\nu)$

$$f_h = (\tau + l_{h1} + 0.5) f_s / N_i \quad (5.35)$$

$$A_h = \frac{2(y_1 + y_2)}{\left| W_{Ka-p} \left(2\pi(-\tau + 0.5)/N_i \right) \right| + \left| W_{Ka-p} \left(2\pi(-\tau - 0.5)/N_i \right) \right|} \quad (5.36)$$

$$\phi_h = \arg \left[X(l_{h1} + 1) \right] - \arg \left[W_{Ka-p} \left(\frac{2\pi((- \tau - 0.5))}{N_i} \right) \right] \quad (5.37)$$

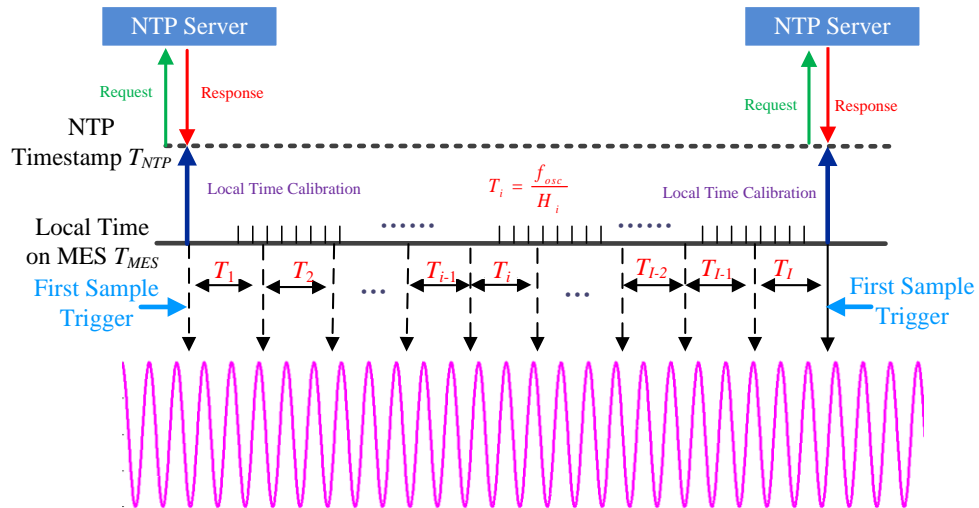


Figure 5.10. NTP based synchronized sampling control technology

5.3 Time synchronization on mobile platform

5.3.1 NTP based time synchronization

Ideal the local timestamp on MES should be identical with NTP time stamp. However, the local time of a MES is likely to drift due to the variation of operation frequency of oscillator influenced by various factors including the change of environmental temperature and aging. Therefore, NTP is used to local time synchronization on MES as illustrated in Figure 5.10. Defining that the synchronization cycle is configured to be m seconds, a timer on MES is used to trigger the first sample each synchronization cycle via the USB connection. To eliminate the accumulative timing error due to the local time drifts, the received NTP time stamp, acted as a reference, is continuously compared with the local time stamp [83]. When the difference between the latest NTP timestamps T'_{NTP} and the local timestamp T'_{MES} is larger than threshold of NTP time error ε satisfying

$$|T'_{NTP} - T'_{MES}| > \varepsilon \quad (5.38)$$

The control parameter (CP) for the local timer on MES will be adjusted as follows

$$CP = m \cdot \frac{T_{MES} - T'_{MES}}{T_{NTP} - T'_{NTP}} \quad (5.39)$$

where T_{NTP} and T_{MES} are the previous NTP and local timestamps, respectively. Meanwhile, the local time is updated from T'_{MES} to T'_{NTP} and is used to as timestamp to tag each frequency measurement.

5.3.2 GPS based time synchronization

Theoretically, the NTP can achieve timing accuracy in the order of 0.1 milliseconds, which is sufficient for phasor measurement. Unfortunately, practical accuracy of NTP time is only up to 15 milliseconds due to the uncertainty of network delay or network instability, corresponding to an unacceptable angle error of 330° in a 60 Hz system. Since the precision of the Pulse-Per-Second (PPS) signal retrieved from GPS receivers in a dedicated pin is in nanoseconds with non-accumulative error [84], the DAQB uses it as a reference to initiate waveform sampling, guaranteeing that the first samples for different units in each synchronization period are all aligned to the PPS signal.

5.3.3 Sampling interval control

For any sampling interval between two adjacent PPS signals, the sampling interval is controlled by the timer in the microprocessor, which suffers from the sampling time errors caused by the

division remainder and oscillator frequency drift in practical implementation. In this section, a PPS disciplined self-adaptive sampling control technology on DAQB is used to remove these sampling time errors [17].

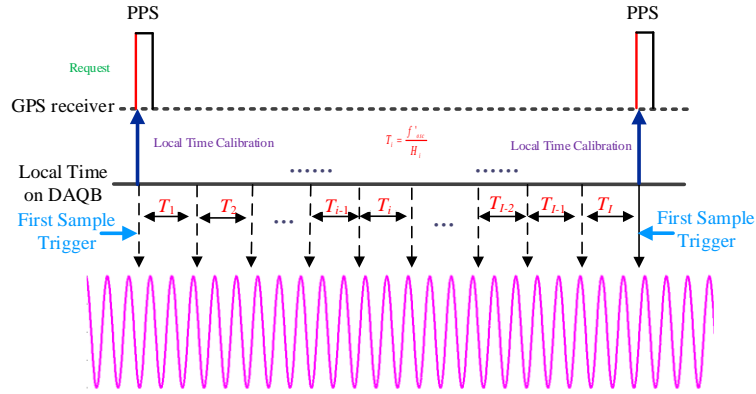


Figure 5.11. Illustration of synchronized sampling control strategy

Due to the change of environmental temperature and aging, the actually output frequency of onboard oscillator in DAQB is likely to drift from its nominal, which means the f_{osc} is not a constant. If f_{osc} is still considered as constant parameter, it will degrade the precision of sampling time control and greatly impair the sampling performance. When f_{osc} is drifting, it is necessary to take adjustments to maintain the sampling accuracy.

To cope with issue, the most straightforward method is to measure actual f_{osc} . Since the PPS signal can achieve an accuracy at nanosecond, besides the common use for triggering sampling, it can be acted as an accurate reference to measure the oscillator frequency f_{osc} . Another timer is set up to count the number of pulse from the onboard oscillator between two rising edges from adjacent PPS signals. The real f_{osc} (denoted as f'_{osc}) equals to the number of counter. Replacing f_{osc} by f'_{osc} , the sampling control can be self-adjusted according to working conditions of oscillator. Compared with the widely-used oscillator calibration method, mainly via temperature indicator, the utilization of PPS signal for oscillator frequency monitoring does not add any extra hardware and has the advantage for low cost. Moreover, the control parameters in the self-adaptive sampling method is adjusted corresponding to the f'_{osc} updated every second, thus eliminating the adverse impact of temperature and aging sensitivity of oscillator on the synchronized sampling control.

5.4 Performance evaluation

5.4.1 Experiment setup

In this section, experiments over both signal generator and real power grid were conducted to evaluate the accuracy of proposed MD for phasor measurement. The test setup is shown in Figure 5.12. In the first test (signals from a signal generator), a Doble F6150 power system simulator with frequency and angle accuracy of 0.5 part-per-million and 0.1° respectively is used to provide input signal. In the second test, the signals are from (120V/60Hz) distribution level power grid. Since the “true” phasor value of the real power grid are unknown, an FDR with frequency and angle accuracy of 0.001Hz and 0.02° is set up as a reference for accuracy evaluation. The Doble F6150, FDR, and proposed MD are all synchronized by GPS signal throughout the tests. The RDFT algorithm is used for phasor estimation. It is assumed that real power grid frequency generally keeps constant in the RDFT windows (0.1 seconds when $N=144$), a 2nd order polynomial function is sufficient to represent the characteristic of angle change. Therefore p in (5.10) is set to be 3 in the smartphone for frequency estimation.

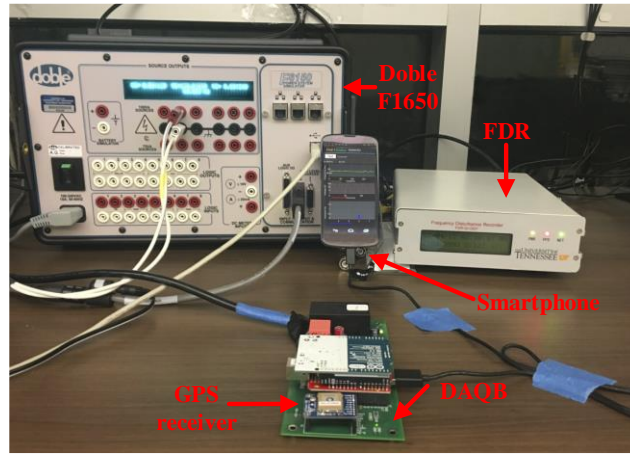
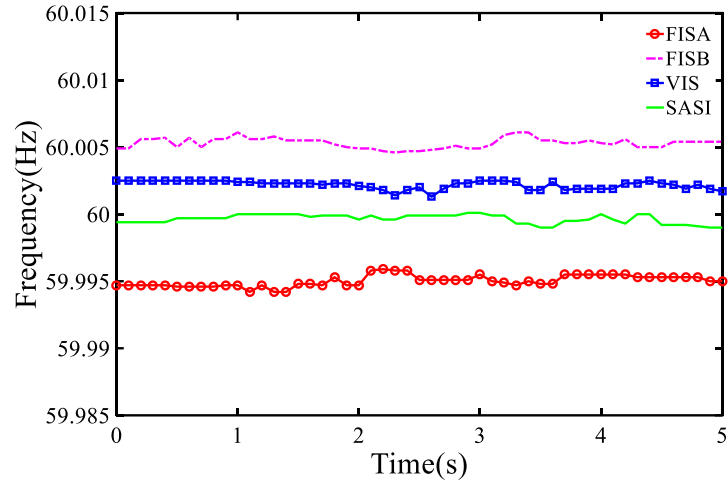


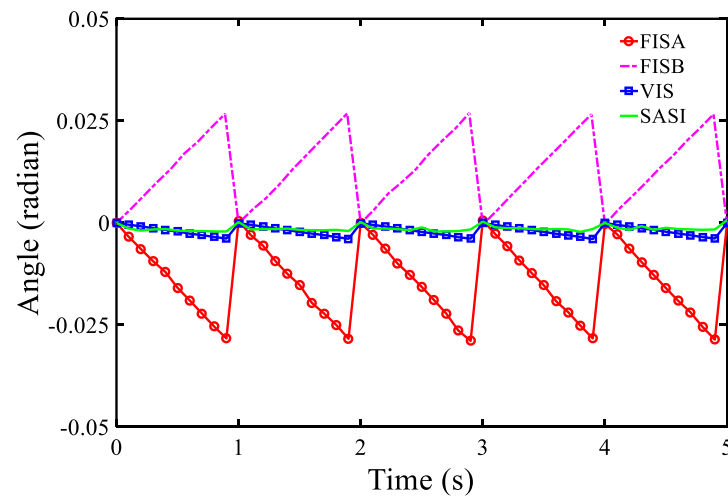
Figure 5.12. Experiment Setup

5.4.2 Signals from Doble F6150

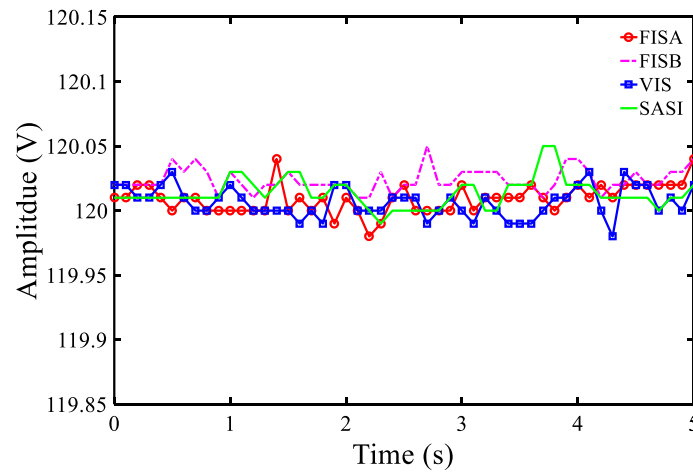
To verify the effectiveness the proposed sampling method, four different sampling control methods, including the conventional fixed sampling interval with timer period register= H_A (FSIA), the fixed sampling interval with timer period register= H_B (FSIA), the variable sampling interval (VSI) and self-adaptive sampling interval (SASI), are implemented in the DAQB for comparison.



(a) Angle results



(b) Frequency result



(c) Amplitude result

Figure 5.13. Measurement result for input signals from Doble F1650

The angle, frequency and amplitude measurement results over sinusoidal 60 Hz AC signals from the Doble F6150 are shown in Figure 5.13(a)-(c). From Figure 5.13(a), the “saw tooth” angle errors of the FSIA and FSIB are effectively eliminated using the VIS and SASI. From Figure 5.13(b), the DC offset in frequency measurement are also removed using the VIS and SASI. Compared with VIS, the angle measurements of SASI are smoother and frequency measurements are closer to 60 Hz, demonstrating the performance improvements by monitoring oscillator frequency.

The root mean square errors (RMSE) for each parameter and TVE are listed in Table 5.1. Since the result of RMSE considers both bias and variance, the SASI is obviously improved with respect to both angle and frequency error compared with other three methods. The frequency and angle of SASI are $4.51\text{E-}4$ Hz and $9.4\text{E-}4$ radian, respectively, which sufficiently complies the IEEE synchrophasors standard C37.118.1 that requires the frequency and angle measurement errors smaller than $5\text{E-}3$ Hz and $1\text{E-}2$ radian respectively. The errors of amplitude measurements are within $5\text{E-}2$ V for all methods, thus concluding that the amplitude is not sensitive to the sampling interval. It also can be seen that the total vector error of SASI is 0.025%, sufficiently meeting 1% requirement in IEEE standard.

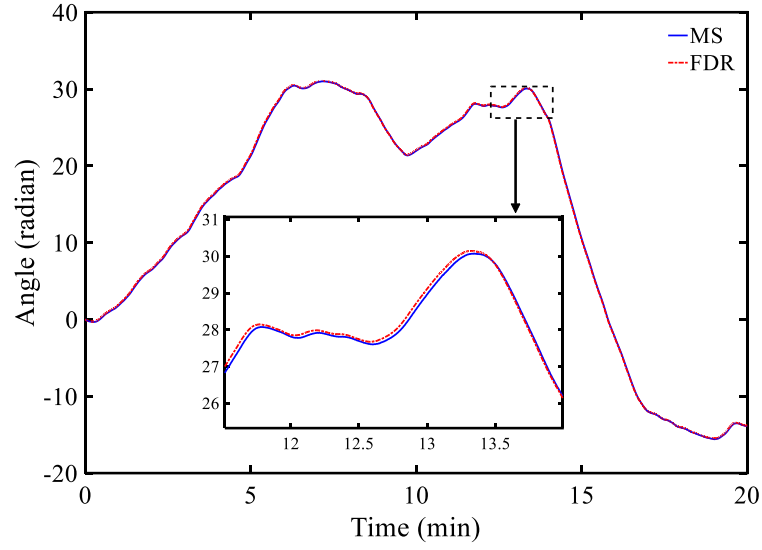
By adopting a RDFT for complexity reduction, this phasor estimation APP consumes less than 20 % of the CPU load in the idle state, which will not significantly influence the overall performance the smartphone.

Table 5.1 Measurement error comparison

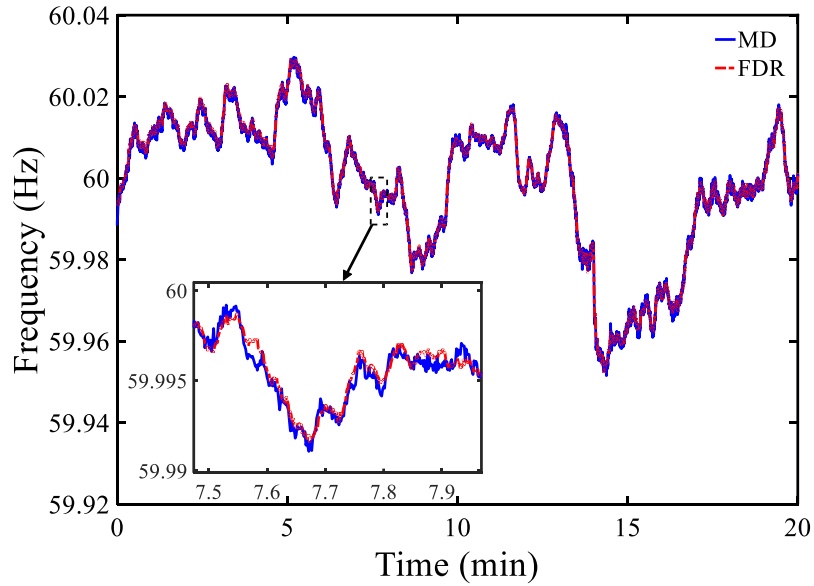
	FISA	FISB	VIS	SASI
Frequency (Hz)	5.31E-3	5.34E-3	2.13E-3	4.51E-4
Angle (radian)	1.69E-2	1.61E-2	1.31E-3	9.40 E-4
Amplitude (V)	1.26E-2	1.23E-2	1.01E-2	8.81 E-3
TVE (%)	1.83E-0	1.89E-0	1.52E-1	2.57E-2

5.4.3 Signals from power grid

To further verify effectiveness of the proposed MD for phasor measurement, the developed prototype are tested using single-phase power grid signals at distribution level. To be compatible with the FDR for comparison, the reporting rate of the MD is set to be 10 Hz as same as FDR. All measurements are time-stamped with the GPS time index. During the test, the FDR has the issue of data missing (overall 1.12%) due to random failure of network connection while the MD keeps complete data in database since it can write data in local memory for backup besides send it to the server via network.



(a) Angle results



(b) Frequency result

Figure 5.14. Measurement result for input signal from distribution level power grid

The 20-minute continuous angle and frequency measurement results for power grid signal are plotted in Figure 5.14(a)-(b). The MD is capable to efficiently capture the trends of frequency and angle change over time, verifying that MD can achieve the same accuracy level as FDR. The difference of frequency and angle are as small as $2\text{E-}3$ Hz and $1\text{E-}2$ radian, which are posed by the

different hardware selections e.g., PT, analog filters, ADC and GPS receiver [85][86]. Compared with the FDRs, the MD has advantages of portability, flexibility, data save capability and low cost.

5.5 Power grid disturbance event detection

5.5.1 Event detection mechanism

Since neither the current PMUs nor FDRs are capable of saving measurement data locally and performing in-memory computing, they have to send measurement data to the PDC or FNET/Grideye server via internet for event detection, which complicates the communication infrastructure and leads to time delay for data aggregation from different locations [87][88].

Fortunately, this issue can be resolved in the MD since the each individual smartphone is capable of running real-time detection task. Therefore, a distributed event trigger is implemented in the smartphone as illustrated in Figure 5.15.

When the smartphone obtains a dataset of frequency measurement from phasor estimation component, an n -point median filter is applied to remove isolated spike and outlier as

$$f_{median}^i = median(F^i) \quad (5.40)$$

where $F^i = \{f_{i+1}, f_{i+1}, \dots, f_{i+n}\}$ is the i th frame. Then the trigger calculates the rate change of frequency (rf) thin a sliding window. If two consecutive rf_i and rf_{i+1} exceeds an event threshold, the trigger will judge the statement whether the following df_{i+10} and df_{i+50} are smaller than the post-event threshold in order to eliminate the adverse impact of power system oscillation on the event trigger. If the statement is true, the smartphone device sets the event trigger flag as '1', otherwise keeping it as '0', and sends it to the server. It is noted that the event and post-event thresholds varies in different synchronous power systems due to their unique frequency response characteristics[87][89].

The data server concurrently receives trigger flags from distributed smartphones via different data channels. Upon received flags, the servers holds a major voting process to make use of information from distributed smartphones deployed at different locations within a grid interconnection. The voting score (VS) is the sum of the received trigger flags, which can be expressed as

$$VS = \sum Trigger_flag \quad (5.41)$$

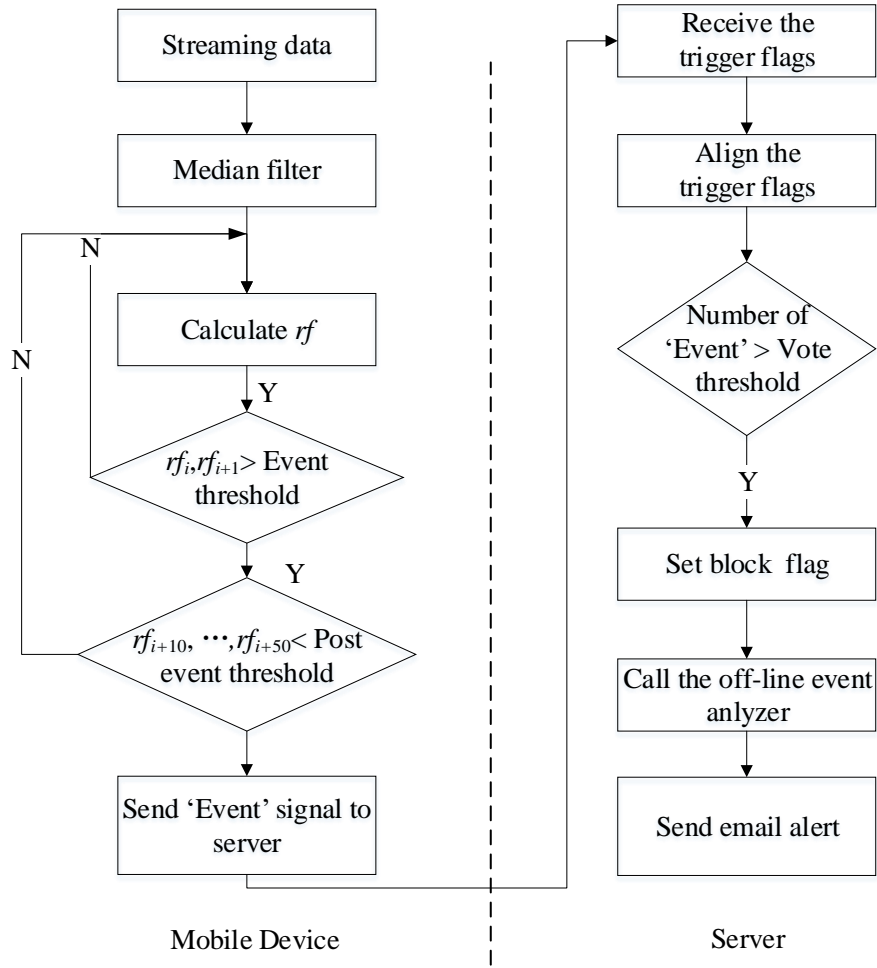


Figure 5.15. The flowchart of the distributed event trigger

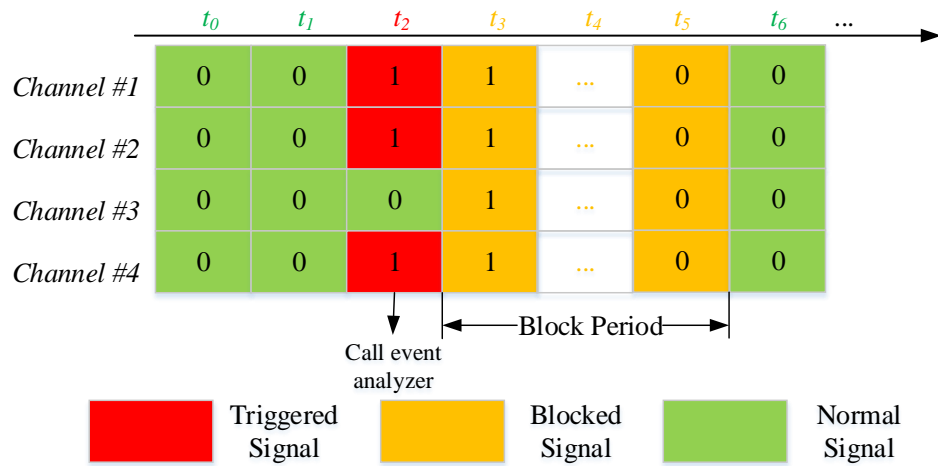
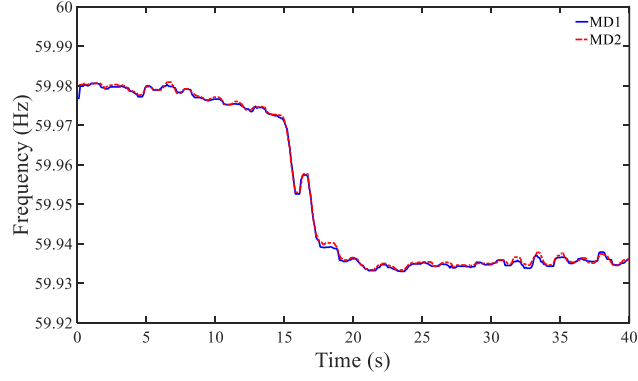
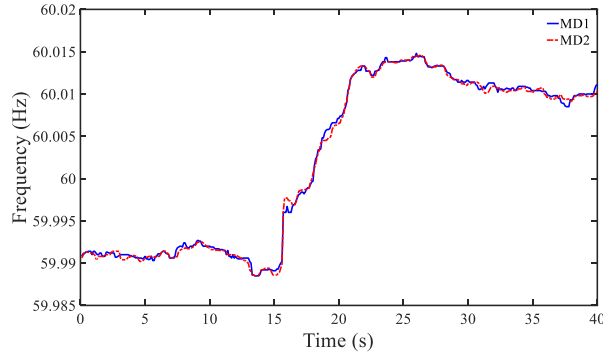


Figure 5.16. The illustration of major voting process for event trigger



(a) Generation trip



(b) Load shedding

Figure 5.17. Frequency plots during power system disturbance events

If VS exceeds the voting threshold, the server will confirm trigger results as a disturbance event and call an off-line event analyzer to extract the event data for event analysis such as event localization and send email alerts to subscribers. To prevent multiple alerts at a short time, a Block Period is defined to block the event signals within a short period. If an ‘event’ is triggered at t_n , any ‘event’ signal appears within the next $block$ seconds are blocked. An example of the voting process is illustrated in Figure 5.16. In this example, the server receives trigger flags from 4 devices via channel 1# to channel 4#. Assuming the voting threshold is 2 for this example, at t_2 , VS exceeds the threshold. As a result, event trigger confirms a disturbance event and calls an off-line event analyzer. Meanwhile the following event signals from t_3 to t_5 are blocked.

5.5.2 Detected event

To further verify the feasibility of the proposed MD for event detection, two MDs were running in Eastern Interconnections (EI), the United States, for power system event detection. Figure 5.17

shows the frequency plots of two detected events. Figure 5.17 (a) is the frequency plot of 1000MW generation trip happened at 20:46:02 UTC, Feb, 3rd 2017 near G G Allen power plant (SERC) in Belmont, NC. During this event, the real power grid frequency drops more than 0.05 Hz. Figure 5.17 (b) shows the frequency plot of load shedding at 08:30:13 UTC, April, 11th, 2017, where the frequency experiences a sudden increase recorded in both MDs. Running a single-phase distribution level, the MDs are able to detect the power system disturbance event and capture the transient dynamic of power system during an event, which provides useful information to monitor the operation state of the power grid.

5.6 Conclusion

This chapter has presented single-phase power grid phasor measurement on the Android mobile device with GPS synchronization. The prototypes of the proposed MDs was developed and the whole design can be generalized to any smartphones for phasor measurement. Experiments verified the accuracy of the proposed MDs. A real application of power system event detection was presented using the proposed MDs, demonstrating the effectiveness of phasor measurement on MDs. Compared traditional PMUs, the proposed system lowers both manufacturing and installation costs. Moreover, it has the advantages of convenience and flexibility, greatly broadening the current PMU family, which will facilitate the large-scale deployment of the phasor monitoring system. The main contribution of this chapter includes

- 1) A single-phase phasor measurement on the mobile device, including a DAQB for data sampling and a smartphone for data process and management, is first realized using GPS synchronization.
- 2) The phasor measurement algorithm with low computational overload is implemented on the smartphone. The accuracy of amplitudes, frequency, and angle measurement are verified via experiments.
- 3) GPS based synchronization technology is adopted in the DAQB. A self-adaptive sampling interval control method is used to compensate sampling time error caused by division remainder and system clock drifts.
- 4) A practical application of power system event detection is developed using the proposed MD. The real disturbance event of power system can be effectively detected and its dynamic characteristic can be well-captured.

Further work will focus on system simplification, waterproof design, dynamic performance evaluation according to the IEEE standard and integration more measurement functions, e.g., power quality monitoring on the MDs.

Acknowledgment

This chapter is, in part, a reprint of the material in the papers: W. Yao, H. Lu, M. Till, W. Gao, Y. Liu, Synchronized Wireless Measurement of Power System Frequency using Mobile Embedded Systems, *IEEE Transactions on Industrial Electronics*, vol. 65, no. 3, pp. 2775-2784, March 2018.

Chapter 6 Source Location Identification of Electric Network Frequency Signals

6.1 Introduction

The electric network frequency (ENF), which typically fluctuates around its a nominal value (50 or 60 Hz) and faithfully reflects the balance between generation and load, has becoming an emerging forensic tool for recorded media authentication[90]. The ENF criterion was first proposed by Grigoras[91] and since then copious research has been conducted, mainly focusing on techniques for ENF extraction from multimedia recordings or the use of ENF as a signature to ascertain the time, location and authenticity of recordings [92]-[95].

However, there are significant fundamental questions remaining, prominently: what are the limitations of ENF location identification? Can the ENF signal from a given location be regarded as unique in order to verify the place a recoding was taken? The answers to these two questions could potentially pave the way for the usage of ENF-based applications and provide direction to future research for recording authentication.

It is well known that power grid frequency in different interconnections is determined by the overall balance between generation and load[96]. Thus, the ENF signals recorded across different interconnections can be distinguished using a feather extraction method and machine learning system [97]. For the ENF within an interconnection, most existing research assumes that the signals across an interconnected power grid are identical [98]. However, in a real power system, it is likely that there are some minor variations in ENF signals recorded at different locations. A power system disturbance such as a generator trip may have an effect on the whole grid which prorogates with measurable time coefficients. In references [99][100], the location estimation within an interconnection is realized based on correlation coefficient (CC) on different locations. However, it needs availability of concurrent ENF signals to obtain the CC. It is known that in the United States Eastern Interconnection (EI), these frequency changes propagate throughout the grid at a speed of approximately 500 miles per second. Moreover, the various electromechanical propagation speeds for the effects of changes in local loads to other locations mean that some slight variation or transient differences may be uniquely reflected in local ENF signals. Furthermore, due to nonlinear load and recurrent local disturbance, environmental noises such as fluctuation and

variation of ENF may result some long-term signatures in the ambient ENF data in different locations. It is hypothesized that these signatures, if successfully extracted, might be potentially used for ENF location identification within an interconnection, which will significantly broaden the scope of ENF related applications. Following this, the objective of this chapter is to develop a machine learning implementation to identify the characteristics of ENF from different locations and classify ENF signals by their geographic source. To verify this hypothesis, this chapter explores the possibility of retrieving signatures from ENF signal using real power grid frequency measurements recorded within a single interconnection.

In this chapter, a reference database is first established for distribution-level ENF using the FNET/GridEye system. Second, this chapter proposes a new approach which combines both signature extraction and machine learning. An L-level Daubechies wavelet is used to remove the common component from an ENF signal and a Fourier transform is used to extract the local signatures. To determine the source location of the ENF, a feed-forward artificial neural network (F-ANN) is applied to the extracted signature. These experiments use FNET/GridEye frequency measurements from the EI at multiple geographic scales (500 miles, 200 miles, and 2 miles) to evaluate identification performance. The accuracy of ENF location identification is given and the factors which influence identification accuracy are discussed. The outcomes of this work are beneficial for authentication of digital multimedia and preventing cyber attacks on critical infrastructure, e.g., power systems, by detecting if real data have been tampered with or wholly replaced by fake data.

6.2 ENF reference database

Establishing an ENF reference database is a prerequisite for the application of multimedia recording authentication using an ENF criterion. To apply the multimedia recording authentication, an ENF signal embedded in a multimedia recording is extracted and then matched against a pre-established ENF reference database. For the multimedia recording ENF extraction, either time or frequency domain methods, such as the zero-crossing method, spectrogram and subspace-based signal processing techniques, wavelet or short-time Fourier transform (STFT) are used.

Phasor measurement units (PMUs), invented in the 1980s and installed in high-voltage transmission-level substations, are able to provide Global Positioning System (GPS) time synchronized frequency measurements, which can be used as a data source for the ENF database. However, frequency measurements at the transmission level do not observe the local distribution-

level characteristics, e.g., small load changes, leading to inapplicability of the ENF identification on a granular geographic scale.

Originally developed in 2003, the Frequency Monitoring Network (FNET/GridEye) system is a wide area phasor measurement system at the distribution-level. Precise frequency measurements (at an accuracy of 0.0005 Hz) obtained by Frequency Disturbance Recorders (FDRs), members of the PMU family, are time-stamped using GPS synchronization[107][107].

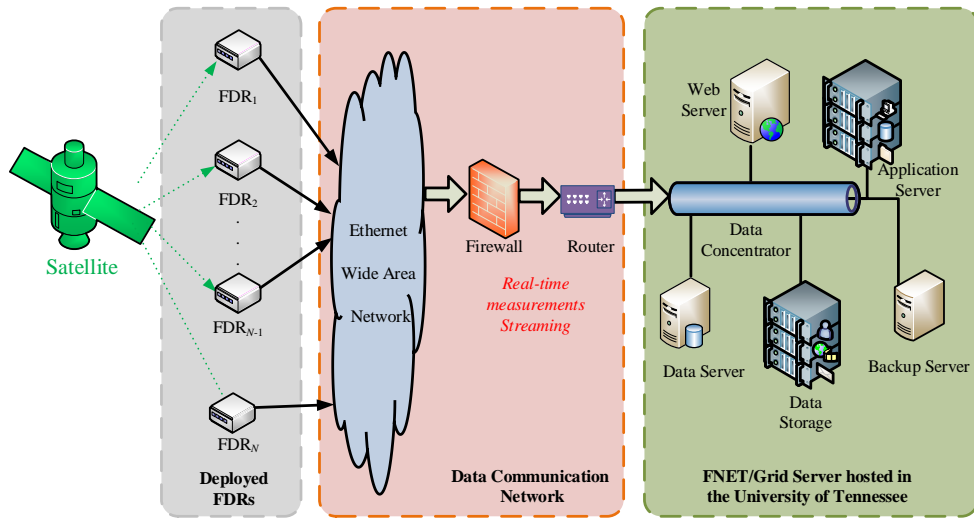


Figure 6.1. The framework of FNET/GridEye system

The ENF reference database can be established using the data aggregated on FNET/GridEye servers. The architecture of the ENF database, as illustrated in Figure 6.1, consists mainly of three components: frequency sensors, Internet-based communication infrastructure, and data servers. FDRs act as frequency sensors recording the instantaneous ENF every 0.1 seconds and transmitting them to a data center at the University of Tennessee, Knoxville(UTK) for storage and analysis. Then FNET/Grیده system provides data storage and application functions (e.g., disturbance detection, oscillation detection, post-disturbance analysis, and web services) [101]. Internet-based communication infrastructure provides communication channels between FDRs and FNET/GridEye servers. Earlier studies show that frequency measurements collected via the FNET/GridEye system are able to match the frequency extracted from digital recordings using the iterative oscillation error correction method and STFT [102], [103]. Figure 6.2 demonstrates the effectiveness of the FNET/GridEye system as an ENF reference database.

6.3 Methodology

6.3.1 Signature extraction

Due to hardware failure, e.g., GPS signal loss, spoofing, or network interruption[55], [56], [104], FDR frequently suffer from invalid and missing data. To avoid bad training of the recognition model using pre-collected frequency measurements from the database, the continuity and validity of data are checked prior to signature extraction from ENF signal. Since each measurement is synchronized with a GPS time index, a discontinuous index implies missing data. In order to adequately train the F-ANN for ENF identification in this study, a minimum length of 15-minutes of uninterrupted frequency data (9000 continuous data points) are required. If sufficient data is not available for a given unit in a certain time window, any data from that window belonging to that unit is not excluded. Frequency measurement spikes are identified using a median filter. Spikes that exceed a preset threshold are replaced by values from median filter results. The advantage of this spike identification method from [105] is that it only eliminates isolated spikes while keeping all other raw data intact, preserving as much detailed frequency information as possible.

Since local frequency affects are of interest, it is essential to remove the common frequency component from each signal in the interconnection in order to extract local signatures from ENF signals. Figure 6.3 shows concurrent frequency measurements recorded from three FDRs at different locations in the EI. It can be observed that all three frequency curves are highly correlated with a common component. Variations from this component can be seen more clearly in the callout window.

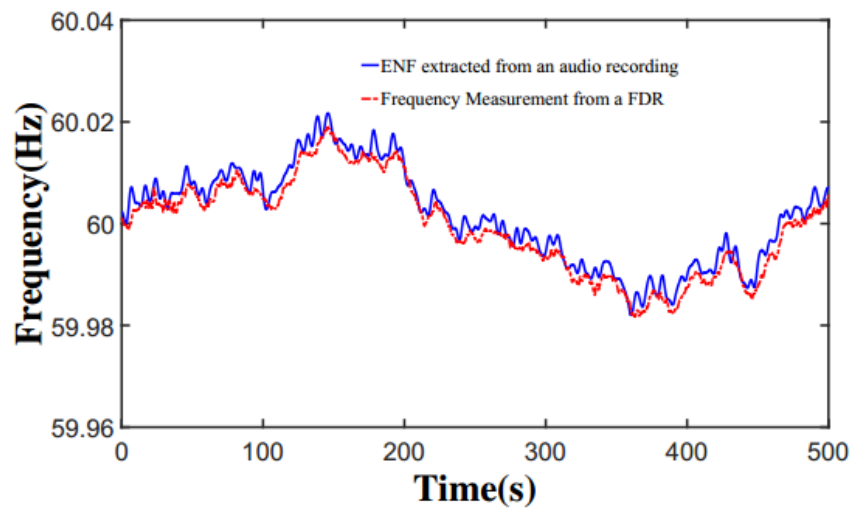


Figure 6.2. Plot of FDR measurement and ENF extracted from an audio recording

One approach to remove the common component is to subtract the median frequency for all units in the interconnection from the original signal. The median frequency, which can be obtained using the median filter method, is chosen to approximate grid frequency due to its robustness with a large number of units running concurrently [104]. The median frequency method is straightforward and effective in removal of the common component.

However, the performance of the extraction method is significantly influenced by the number of FDRs with available data. In the case where there is only one or two FDRs identified with available data, median frequency cannot precisely represent the common component. Therefore, in this chapter, an L -level Daubechies wavelet-based extraction method is applied instead, where each level provides an approximation to the original signal and the detailed variations at a specific level of resolution. Assuming the ENF signals $ENF_1...ENF_n$ are absolutely and square integrable, the wavelet transform of $ENF_n(t)$ can be expressed as

$$Wf(v, \lambda) = \frac{1}{\sqrt{v}} \int_{-\infty}^{+\infty} ENF_n(t) \Psi^* \left(\frac{t - \lambda}{v} \right) dt \quad (6.1)$$

where v and λ are defined as the dilation and timetranslation parameters respectively. The mother function Ψ^* is a Daubechies wavelet satisfying admissibility condition [105].

As illustrated in Figure 6.4 the lower time variance of the lower time-frequency band (the approximation) is considered to be the common component of the frequency measurements and the variances of the high-pass band (e.g., Detail 1 and Detail 2) can potentially be used for local signatures extraction. Although the wavelet-based method introduces greater computational complexity than the median frequency method, it is more flexible and can obtain local signatures without relying on the availability of concurrent ENF signals.

Figure 6.5 shows the signatures extracted from three FDRs using the wavelet-based method of Detail 1. It can be seen that the signatures from ENF signal are chaotic and stochastic in the time domain. It is assumed that the local signatures may have specific patterns in the frequency domain. Therefore, the fast Fourier transform with a window length of 600 data points (1 minute of data) and a 10 second moving window is performed to obtain the input spectrum for F-ANN as illustrated in Figure 6.6. It can be observed that each of the signatures has a distinct spectral distribution attributed to local factors that can be used as input samples when training the F-ANN for source location identification.

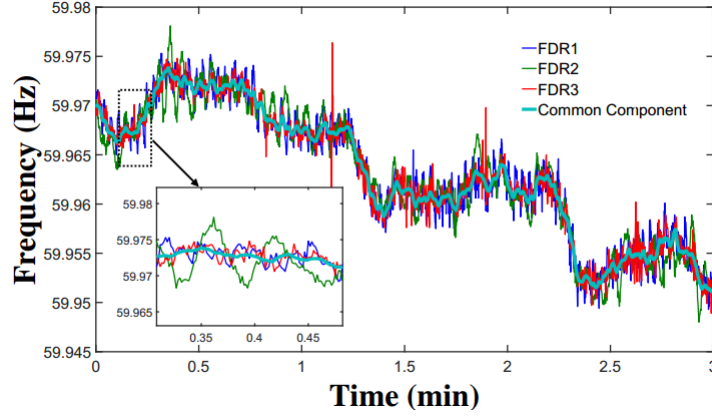


Figure 6.3. The plot of frequency measurements recorded on difference locations in EI

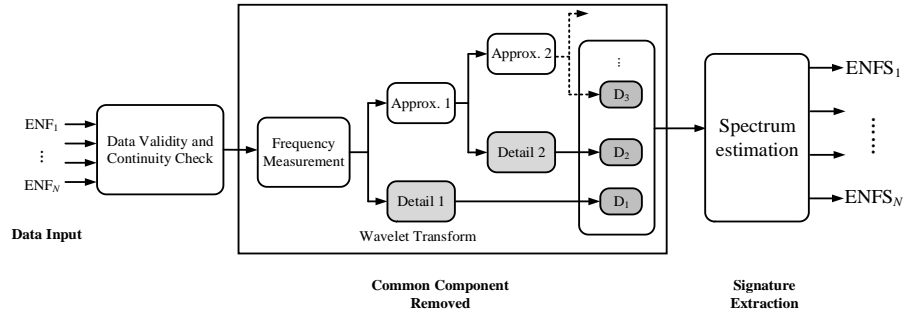


Figure 6.4. Flowchart of the signature extraction from raw ENF signal

6.3.2 Location identification

The spectrum data $ENFS_1 \dots ENFS_n$ of frequency measurements in the database recorded from different locations and time periods is used to train the three-layer F-ANN. The structure of the F-ANN is illustrated in Figure 6.7. The input vector is the absolute value of 1 minute ENF spectrum at a resolution of 0.0166 Hz. An FDR outputs 600 frequency measurements per minute. The length of the input vector is 300 since the FFT spectrum is symmetrical. The target vector is the column vector of a size equal to the number of FDR locations. Each target vector has “0”s in all rows except one. The position of the unique “1” element in each column indicates the location of the corresponding input vector. For example, a “1” in the n th row of a target vector indicates that the corresponding input vector originated from a unit with index n . The transfer function *tansig* for the hidden layer is defined as

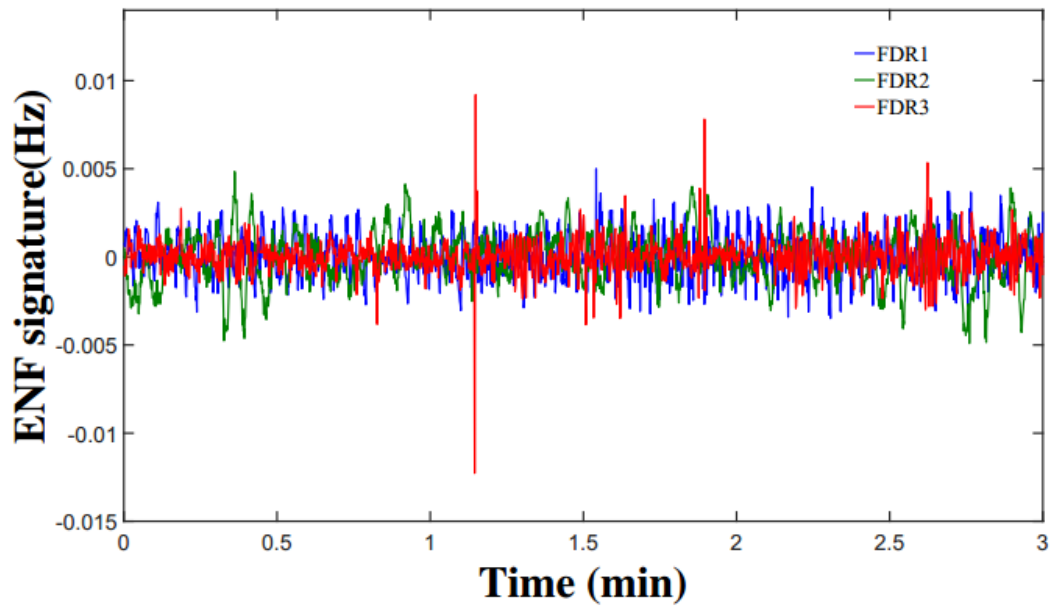


Figure 6.5. Signature extraction from ENF signal using wavelet transform

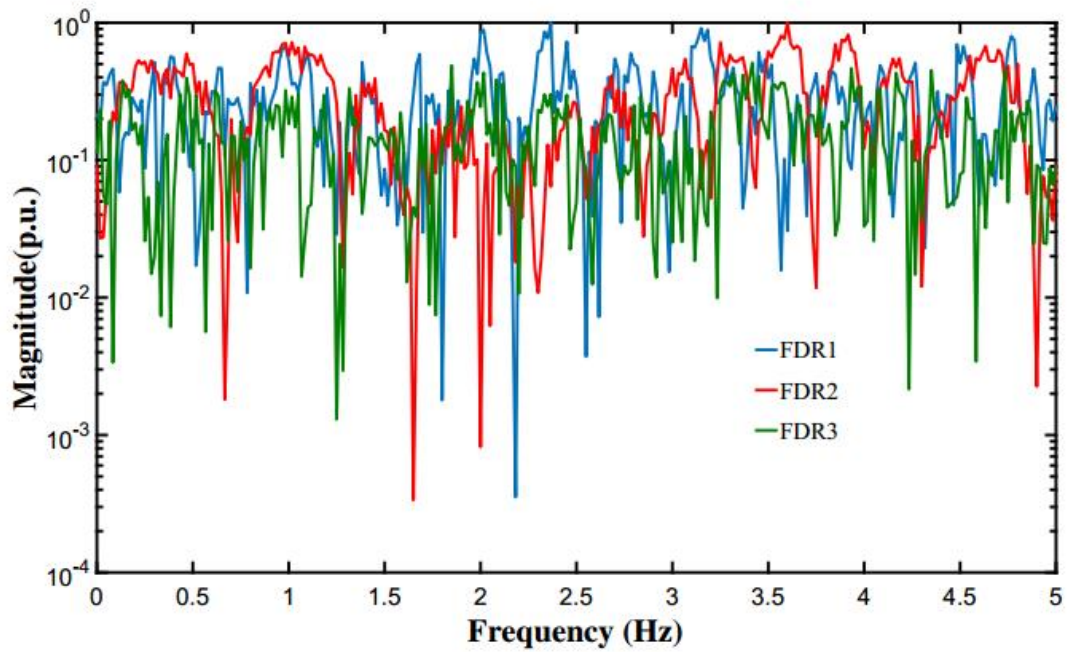


Figure 6.6. Spectrum distribution of extracted signature from raw ENF signal

$$\text{tansig}(x) = \frac{2}{1 + e^{-2x}} - 1 \quad (6.2)$$

In the final layer, a *softmax* function is used to normalize the output to (0,1] while preserving ordering. This function is defined as

$$\text{softmax}(z_n) = \frac{e^{y_n}}{\sum_{n=1}^N e^{y_n}} \quad \text{for } n = 1, \dots, N \quad (6.3)$$

where y_n is the output from the hidden layer and N is the number of locations. The purpose of the *softmax* function is to approximate a unitary target vector $z_n \subseteq (0; 1]$. The most likely location of the input vector is determined at the maximum value of the output vector. For the training process, these input vectors are provided alongside target vectors.

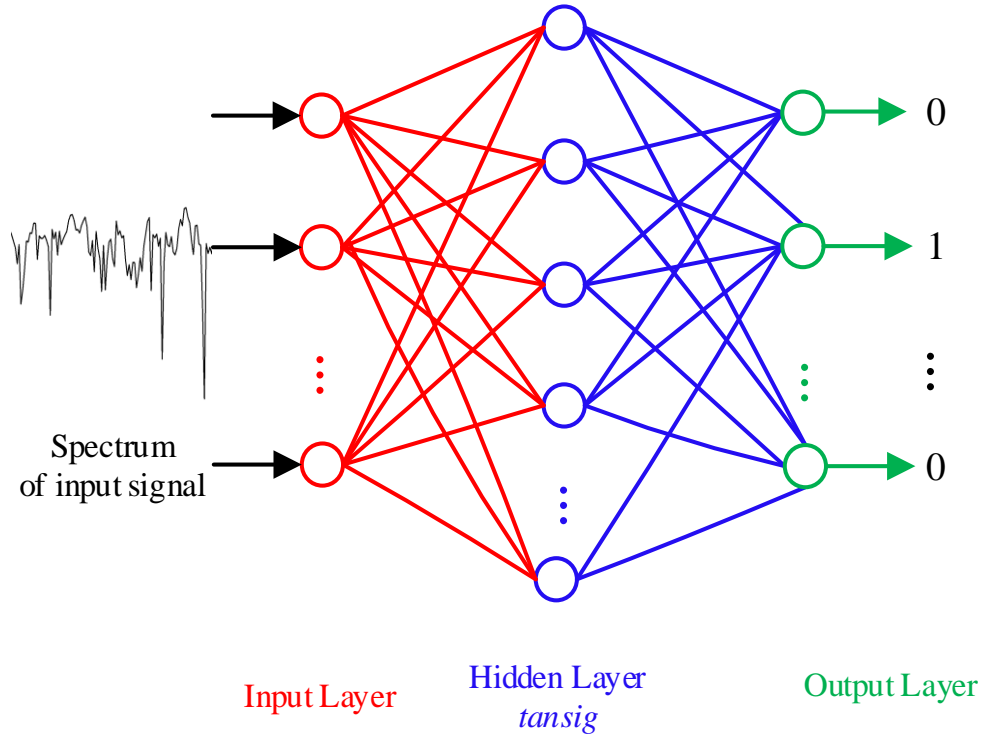


Figure 6.7. Structure of the F-ANN

ENF signals Training vectors are randomly assigned to training, validation, or test sets, satisfying 70% for training, 15% for validation, and 15% for testing. Once the F-ANN is trained, it will be used to identify the location of ENF signals from an unknown source recorded outside the time window covered by training data as illustrated in Figure 6.8.

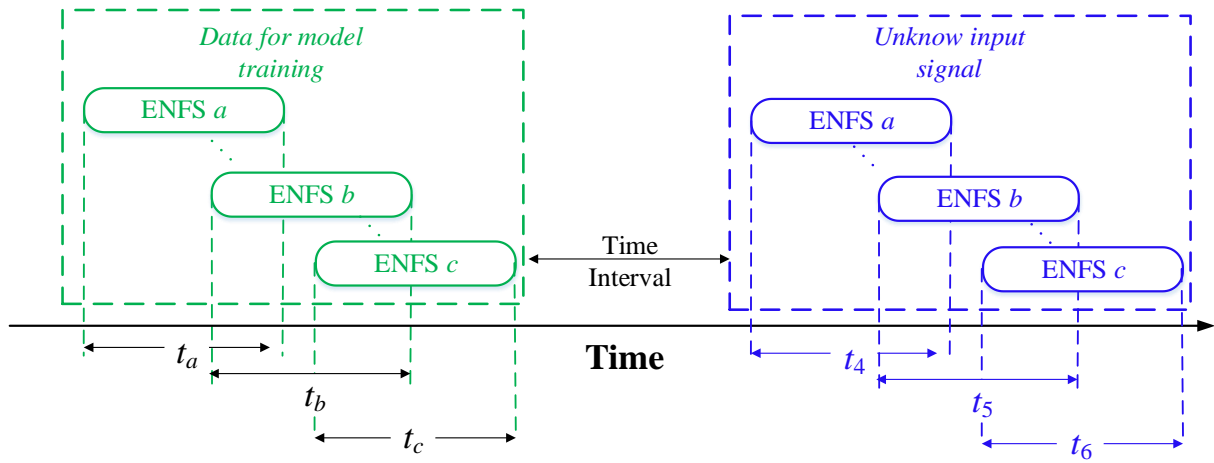


Figure 6.8. Illustration of location identification of extracted signatures from

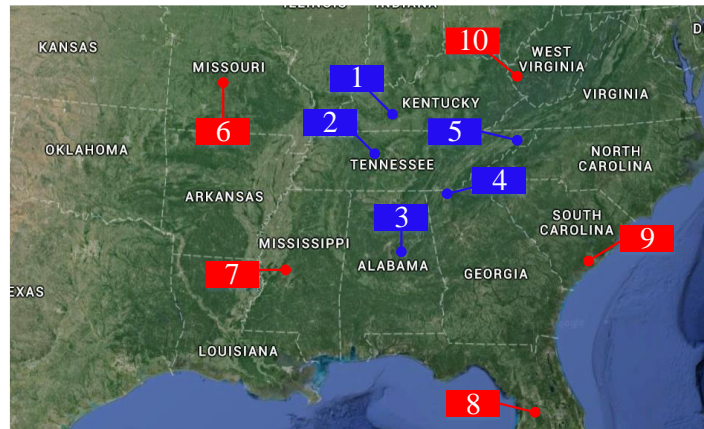


Figure 6.9. Map of FDR locations for Case I and Case II

Red labels: Case I. Blue labels: Case II

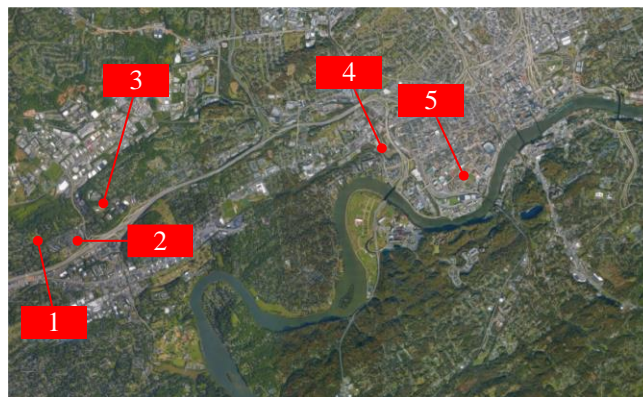


Figure 6.10. Map of FDR locations for Case III

6.4 Performance evaluation

Taking advantage of the widespread deployment of FDRs, an experiment is carried out to test the performance of the proposed approach for location identification. Frequency measurement data from are obtained from the FNET/Grideye. Historical data from each of locations is used to train the FANN and then an signal of unknown origin (from one of the training unit locations for the purpose of this analysis) is identified using the F-ANN. Three geographic scales, Case I (500 miles), Case II (200 miles) and Case III (2 miles), are tested. Five FDRs are randomly selected for each case. For case I, FDRs in difference EI states (Missouri, Tennessee, South Carolina, West Virginia, and Florida) with a minimum distance of approximate 500 miles between any two units, are selected as mapped in Figure 6.9. For Case II, FDRs deployed in states of Alabama, Tennessee, Kentucky and Georgia at distance of approximate a minimum distance 200 miles between units are selected and mapped in Figure 6.9. For the Case III, five locations of in the city of Knoxville, Tennessee, are selected as shown in Figure 6.10.

6.4.1 Model training

A 3-layer F-ANN is trained using historical data by the backpropagation algorithm for location identification of given signals. The number of neurons greatly influences the identification accuracy and training time. After some trial and error, it was found in this study that the optimally number of neurons in the hidden layer is 50. Further increasing the number of neurons will not substantially improve accuracy, but does lead to longer training times. For example, the training time of 5 units for the number of neuron 50, 100, and 150 are 1.2s, 2.6s and, 5.6s respectively. As discussed in Section III, the FFT spectrum of the extracted signature serves as an input vector for training. Each of these input vectors is assigned a corresponding target vector, which defines the location where the signal originated. In each case, the target vector is a five element column vector. For fair comparison, a 30-minute data set is used for each unit with a sliding window length of 10 points. Therefore, a total of 2.7×10^6 data points were fed to the F-ANN during the training process.

6.4.2 Results of location Identification

The objective of the trained F-ANN is to determine the location of a signal of unknown origin from one of the locations providing historical training data. For signature vector, the F-ANN will return an output vector. The column index of the output vector with the highest value indicates the

corresponding location to be the most likely source of the signal. To evaluate the performance of the F-ANN, the overall identification accuracy is defined as

$$Accuracy = \frac{I_{correct}}{I_{Total}} \times 100\% \quad (6.4)$$

where $I_{correct}$ represents the number of vectors that are correctly identified and I_{total} is the total number of vectors tested.

Table 6.1 Accuracy for FDR location identification

Case	Time Interval	Identification accuracy (%)
I	1 day	99.8
	1 week	99.3
	1 month	98.2
	6 months	90.1
	12 months	80.4
II	1 day	95.6
	1 week	99.3
	1 month	91.5
	6 months	50.2
	12 months	34.4
III	1 day	42.6
	1 week	35.3
	1 month	28.5
	6 months	27.2
	12 months	26.7

The identification accuracy for each case under different time intervals is listed in Table 6.1 I. It can be seen that Case I has the highest accuracy. The location of the a given signal can be identified at matching rate larger than 90% given a 6-month time interval. The accuracy is as large as 80.4% given a 12-month time interval between the signal of unknown origin and training data

in Case I. The confusion matrices of identification accuracy for Case I with time intervals 1 month and 12 months are shown in Table 6.2 and Table 6.3, respectively. For each table, the labels of the columns represent the actual location of the signals tested while the labels of the rows denote the location predicted by the F-ANN. The entries in the highlighted diagonals show the correct identification accuracy for each location. The accuracies are high, ranging from 97.23% to 98.82% (1 month) and 78.82% to 82.67% (12 months) for all locations, which demonstrates the effectiveness of the trained F-ANN for location identification.

Table 6.2 Confusion matrix for case I with a 1-month time interval

The location of tested FDRs		MI	TN	SC	WV	FL
Estimated location	MI	98.23	0.62	0.17	0.97	0.10
	TN	0.29	97.57	0.59	0.39	0.53
	SC	0.71	1.12	98.15	0.14	0.31
	WV	0.20	0.05	0.68	98.23	0.24
	FL	0.74	0.62	0.41	0.27	98.82

Table 6.3 Confusion matrix for case I with a 12-month time interval

The location of tested FDRs		MI	TN	SC	WV	FL
Estimated location	MI	80.42	3.21	4.51	5.78	6.24
	TN	5.15	82.67	3.59	5.26	3.45
	SC	4.56	5.21	81.56	4.99	7.21
	WV	6.12	2.97	1.98	79.12	4.28
	FL	3.75	5.94	8.39	4.85	78.82

There are three potential reasons for the phenomenon that the accuracy varies in different time. First, the local load may change with time (different seasons in a year). Therefore, the environmental noises, which contributes some portions in the local signatures, may be different when local loads are changed, e.g., switching on/off a cooling/heating system. As a result, in some occasions the environmental noise is very strong while environmental noises become weaker or even disappeared in some other occasions. Second, in a real power system, large disturbances may happen and overwhelm long-term environmental noises. The impact of this kind of disturbances

is that the local signatures of ENF signal is still there but hard to be extracted. Third, for our machine learning system, only 1-minute data points are used for identification test. It will be possible that the identified signatures is not covered in the 1-minute data set. The accuracy of the identification are influenced by whether testing data have recorded the sufficient local and extractable signatures. As illustrated in Figure 6.11, the accuracy of Case II is slightly reduced with the increased time intervals. This drop may be caused by the local load change with time. Therefore, to obtain high identification accuracy, the latest available data are preferred for the machine learning. In Case II, identification accuracy with a time interval of 1 month (91.5%) is slightly lower than in Case I (98.2%). Moreover, the rate of this decrease is greater than in Case I. Case III has a smallest geographic scale and considerably lower identification accuracy (below 50%) than Cases I and II. Therefore, it can be generally concluded from these results that location identification of a signal with a relatively large geographic scale leads to better performance than identification with a small geographic scale.

6.4.3 Discussion

To explore accuracy differences across geographic scales, the wavelet-extracted signatures are compared in Figure 6.12. A smaller magnitude of extracted signatures is observed as the geographic scale decreases. For Case I, the amplitude of the extracted signature is as large as 3.12×10^{-3} Hz compared with 5.21×10^{-4} Hz for Case III.

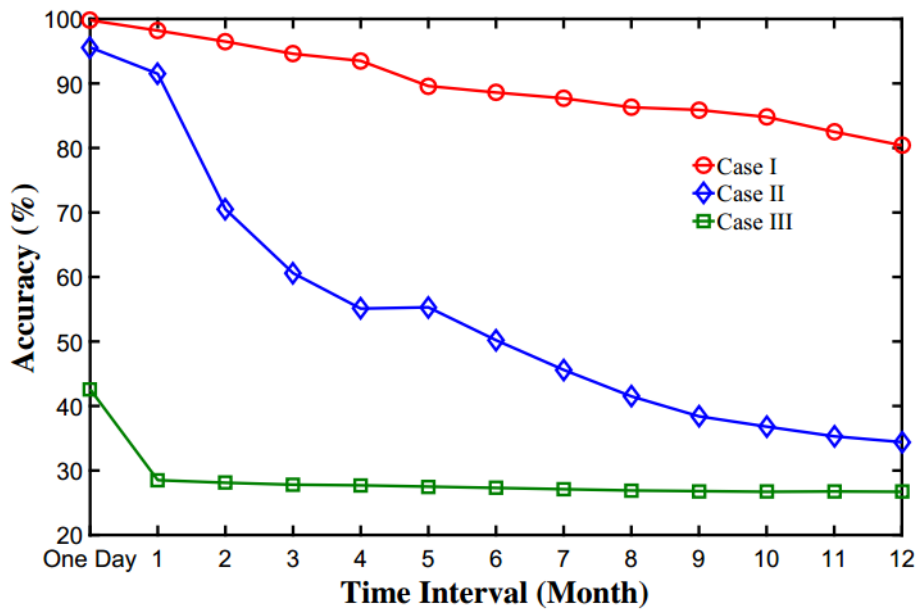


Figure 6.11. Identification accuracy versus the time interval used

As the signature is smaller given shorter distances, the signal may be heavily overwhelmed at the distribution-level by measurement uncertainty or noise. Therefore the wavelet approach cannot effectively extract any distinct features from

ENF signals, leading to the low identification accuracy of F- ANN. For Case III, the amplitude of the signature is close to the FDR frequency measurement resolution of 5.0×10^{-4} Hz.

To examine the correlation between extracted signatures in each case, the normalized cross-correlation of two ENF signals can be expressed as

$$\rho_{k,l} = \frac{\sum_{n=1}^N f_k(n)f_l(n)}{\sqrt{\sum_{n=1}^N f_k(n)^2 \cdot \sum_{n=1}^N f_l(n)^2}} \quad (6.5)$$

where N is the length of each of two signals and $f_l(n)$ is the ENF signal at time n and location l . The probability distributions of normalized cross-correlation for each case is shown in Figure 6.13. From Figure 6.13, the extracted signature with a relatively small geographic scale has a considerable high value of normalized cross-correlation distribution, which indicated a high similarity in ENF signals. This might cause the ENF difficulty to be differentiated. The mean normalized cross- correlations for each case are listed in Table 6.4. It can be seen from Table 6.4 that the value of cross-correlation of Case III (0.8484) is approximately 3 times larger than the value in Case I (0.2872). When the geographic scale is not large enough, the signatures are relatively attenuated and highly correlated. As a result, it is possible that the “true” signature is mostly subsumed by measurement uncertainty and noise, masking the identification references and leading to mistakes in location estimation. Therefore, to identify the ENF location at a small geographic scale, measurement device accuracy must significantly improve.

Table 6.4 Comparison of normalized cross-correlation of extracted signature

case	Normalized CC
I	0.2872
II	0.4112
III	0.8484

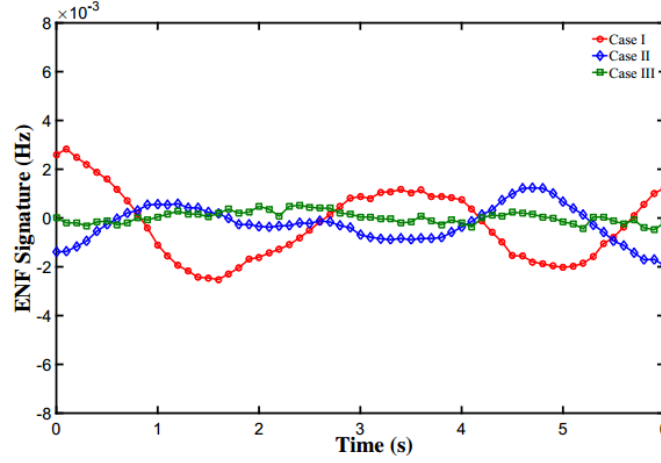


Figure 6.12. Comparison of extracted signatures from ENF signals

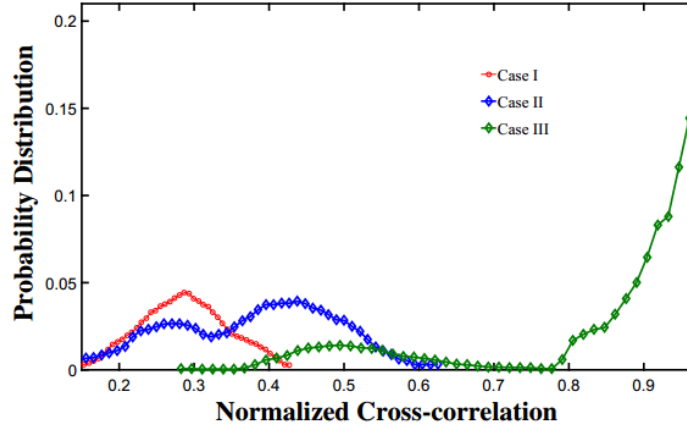


Figure 6.13. The probability distribution of normalized cross-correlation

6.5 Conclusion

In this chapter, a machine learning-based method is developed to identify the location of an ENF signal of unknown origin without concurrent information. First, an ENF reference database is established from FNET/GridEye measurement. Second, an L-level Daubechies wavelet is used for signature extraction from ENF signal and a pre-trained F-ANN to identify the location from which the signal originated.

Three case studies at multiple geographic scales are carried out using frequency data from the FNET/GridEye system to evaluate the performance and applicability of the proposed method. It is found that the accuracy of this method is dependent upon the geographic scales of the input ENF signal. For a large geographic scale (500 miles), accuracy of more than 90% and 80% can be

achieved using 6 and 12 month time intervals, respectively. This verifies the effectiveness of the proposed method on large scale location identification. For a small geographic scale, identification accuracy is low. To address why accuracy drops significantly with a smaller geographic scale, the signatures extracted from each case are compared. It is found that the signatures over a small geographic scale have high values of normalized cross-correlation. As a result, the true local signatures are likely to be subsumed by measurement uncertainty and noise, thus negatively impacting source location identification.

Since ENF signals carry strong potential as location stamps, future work will focus on improving the accuracy of identification with small geographic scales. At the current stage, only frequency measurement signals are used for identification. The next step is to exploit FNET/Grideyes synchronized voltage angle and amplitude measurements as supplementary information. Moreover, increasing the sampling data and output rate may be another possible approach to increase accuracy.

Acknowledgment

This chapter is, in part, a reprint of the material in the paper: Wenxuan Yao, Jiecheng Zhao, Micah Till, Shutang You, Yong Liu, Yi Cui, Yilu Liu, “Source Location Identification of Distribution-level Electric Network Frequency Signals at Multiple Geographic Scales”, *IEEE Access*, vo.5, pp.11166-11175, 2017

List of References

- [1] B. Wang, B. Fang, Y. Wang, H. Liu and Y. Liu, "Power System Transient Stability Assessment Based on Big Data and the Core Vector Machine," *IEEE Trans Smart Grid*, vol. 7, no. 5, pp. 2561-2570, Sept. 2016.
- [2] M. Wu, W. Huang, F. Q. Zhang, X. Luo, S. Maslennikov and E. Litvinov, "Power plant model verification at ISO New England," *2017 IEEE Power & Energy Society General Meeting*, Chicago, IL, 2017, pp. 1-5
- [3] S. You, Y. Liu, G. Kou, X. Zhang, Wenxuan Yao, Y Su, S. Hadley and Y. Liu, Non-Invasive Identification of Inertia Distribution Change in High Renewable Systems Using Distribution Level PMU, *IEEE Trans. Power System*, vol. 33, no. 1, pp. 1110-1112, Jan. 2018.
- [4] P. Héctor, Y. Wang, and H. Silva-Saravia. "On inertia distribution, inter-area oscillations and location of electronically-interfaced resources." *IEEE Trans. Power Systems*, vol. 33, no.1, pp. 995-1003, 2018
- [5] S. You, J. Guo, W. Yao, S. Wang, Y. Liu, and Y. Liu, "Ring-down oscillation mode identification using multivariate empirical mode decomposition," in *Proc. 2016 IEEE Power and Energy Society General Meeting*, 2016, pp. 1-5.
- [6] S. You, G. Kou, Y. Liu, X. Zhang, Y. Cui, M. Till, W. Yao and Y. Liu. Impact of High PV Penetration on the Inter-area Oscillations in the U.S. Eastern Interconnection, *IEEE Access*, vol. 5, pp. 4361-4369, 2017.
- [7] Y. Liu et al., "A Distribution Level Wide Area Monitoring System for the Electric Power Grid—FNET/GridEye," *IEEE Access*, vol. 5, no. , pp. 2329-2338, 2017.
- [8] A.G. Phadke, "Synchronized phasor measurements in power systems," *IEEE Computer Applications in Power*, vol. 6, no. 2, pp. 10-15, Apr. 1993.
- [9] Y. Liu, W. Yao, D. Zhou, L. Wu, S. You, H. Liu, L. Zhan, J. Zhao, H. Lu, W. Gao, Y. Liu, "Recent Developments of FNET/GridEye – A Situational Awareness Tool for the Smart Grid," *CSEE Journal of Power and Energy Systems*, vol. 2, no. 3, pp. 19-27, Sept. 2016.
- [10] IEEE Standard for Synchrophasors for Power System, C37.118-2011.1, IEEE Power System Relaying Committee of the Power Engineering Society.
- [11] IEEE Standard for Synchrophasors for Power System, C37.118-2011.2, IEEE Power System Relaying Committee of the Power Engineering Society.
- [12] FNET/GridEye Web Display, <http://fnetpublic.utk.edu/>
- [13] Y.Liu, L. Zhan and et.al. "Wide-Area Measurement System Development at the Distribution Level: an FNET/GridEye Example," *IEEE Trans. Power Deliver*, vol. 31, no. 2, pp. 721-731, April 2016.
- [14] L. Wang, J. Burgett, J. Zuo, C. Xu, B. J. Billian, R. W. Conners, and Y. Liu, "Frequency disturbance recorder design and developments," in *Proc. 2007 IEEE Power Eng. Soc. Gen. Meet.*, pp. 1–7.
- [15] Y. Zhang, Wenxuan Yao, S. You, W. Yu, L. Wu, Y. Cui, Y. Liu, Impacts of Power Grid Frequency Deviation on Time Error of Synchronous Electric Clock and Worldwide Power System Practices on Time Error Correction, *energies*, vol.9, no.9, 1283, 2017
- [16] J. Chai, J. Zhao, W. Yao, J. Guo and Y. Liu, "Application of Wide Area Power System Measurement for Digital Authentication", in *Proc. 2016 IEEE T&D Conference and Exposition*, pp.1-5.

- [17] W. Yao, L. Zhan, Y. Liu, M. Till, J. Zhao, L. Wu, Z. Teng, Y. Liu, "A Novel Method for Phasor Measurement Unit Sampling Time Error Compensation," vol. 9, no. 2, pp. 1063-1072, March 2018.
- [18] Y. Liu, Y. Jia, Z. Lin, Y. Liu, Y. Zhang and L. Wang, "Impact of GPS signal quality on the performance of phasor measurements," North American Power Symposium (NAPS), pp.1-7, Aug. 2011
- [19] X. Jiang, J. Zhang, B.J Harding, J.J Makela and A.D Dominguez-Garcia, "Spoofing GPS Receiver Clock Offset of Phasor Measurement Units," IEEE Trans. Power Systems, vol.28, no.3, pp.3253-3262, Aug. 2013
- [20] L. Zhan, J. Zhao, S. Gao, J. Cullis, Y. Liu, and Y. Liu, "Universal grid analyzer design and development," in Proc. 2015 IEEE Power Eng. Soc. Gen. Meet, pp. 1-5.
- [21] S. Soni, S. Bhil, D. Mehta and S. Wagh, "Linear state estimation model using phasor measurement unit (PMU) technology," Electrical Engineering, Computing Science and Automatic Control (CCE), 2012 9th International Conference, Mexico City, 2012, pp. 1-6.
- [22] J. De La Ree, V. Centeno, J. S. Thorp, and A. G. Phadke, "Synchronized Phasor Measurement Applications in Power Systems," *IEEE Trans. Smart Grid*, vol. 1, pp. 20-27, 2010.
- [23] V. Centeno, A. G. Phadke, A. Edris, J. Benton, M. Gaudi, and G. Michel, "An adaptive out-of-step relay for power system protection," *IEEE Trans. Power Del.*, vol. 12, no. 1, pp. 61-71, Jan. 1997.
- [24] IEEE Standard Procedures for Measurement of Power Frequency Electric and Magnetic Fields from AC Power Lines, IEEE STD 664, 1994, Reaffirmed 2008
- [25] K. Zhu, W. K. Lee and P. W. T. Pong, "Non-Contact Electric-Coupling-Based And Magnetic-Field-Sensing-Assisted Technique For Monitoring Voltage Of Overhead Power Transmission Lines," SENSORS, IEEE, Busan, 2015, pp. 1-4.
- [26] A. G. Phadke and J. Thorp, Synchronized Phasor Measurements and Their Applications. New York, NY, USA: Spring , 2008
- [27] G. Feng and A. Abur, "Fault Location Using Wide-Area Measurements and Sparse Estimation," *IEEE Trans. Power Systems* , vol.PP, no.99, pp.1-8
- [28] J. Zhao, J. Tan, L. Wu, L. Zhan, L. Yilu, J. R. Gracia, et al., "Impact of Measurement Error on Synchrophasor Applications," Oak Ridge National Laboratory 2015.
- [29] Y. Zhang, W. Yao, J. Culliss, G. Zhang, Z. Teng and Y. Liu, "Electrical field based wireless devices for contactless power grid phasor measurement," in *Proc. 2014 IEEE PES General Meeting*, pp. 1-5.
- [30] S. Mousavian, J. Valenzuela and J. Wang, "A Probabilistic Risk Mitigation Model for Cyber-Attacks to PMU Networks," *IEEE Trans on Power Systems*, vol. 30, no. 1, pp. 156-165, Jan. 2015.
- [31] SmartsenseCom.EPC Optical Power Monitoring System, http://www.smartsensecom.com/uploads/4/7/1/7/47174183/ssc_epc_optical_power_monitoring_system_-_brochure.pdf
- [32] Wenxuan Yao, David Wells, Daniel King, Andrew Herron, Thomas King, Yilu Liu, Utilization of optical sensors for phasor measurement units, Electric Power Systems Research, vol.156, March 2018, pp 12-14,

- [33] G. Zheng, Y. Liu and G. Radman, "Wide area frequency based generation trip event location estimation," IEEE Power and Energy Society General Meeting, San Diego, CA, 2012, pp. 1-6.
- [34] Z. Lin et al., "Application of wide area measurement systems to islanding detection of bulk power systems," *IEEE Trans on Power Systems*, vol. 28, no. 2, pp. 2006-2015, May 2013.
- [35] Y. Liu, W Yao, L. Zhan, H. Lu and Wei Gao, "Mobile electric field sensor based phasor measurement unit for monitoring an electric power grid", U.S. Patent. Application No. 20160025785, 2016
- [36] W. Yao et al., "Source Location Identification of Distribution-Level Electric Network Frequency Signals at Multiple Geographic Scales," *IEEE Access*, vol. 5, pp. 11166-11175, 2017.
- [37] T. Xia and Y. Liu, "Single-phase phase angle measurements in electric power systems," *Power Systems, IEEE Trans. Power Syst.*, vol.25, no.2, pp.844-852, May 2010.
- [38] W. Yao, Z. Teng, Q. Tang and Y. Gao, Measurement of power system harmonic based on adaptive Kaiser self-convolution window, *IET Generation, Transmission & Distribution*, vol. 10, no. 2, pp. 390-398, 2016.
- [39] Z. Ning and *et.al* "Dielectric Relaxation of MIM Capacitor and Its Effect on Sigma-Delta A/D Converters," *IEEE Trans. Semicond. Manuf.*, vol.21, no.4, pp.549-564, Nov. 2008
- [40] M. Yue, D. Wu and Z. Wang, "Data Compression for Image Sensor Arrays Using a 15-bit Two-Step Sigma-Delta ADC," *IEEE Journal Sensors*, vol.14, no.9, pp.2989-2998, Sept. 2014
- [41] A. Mertens and D. Eckardt, "Voltage and current sensing in power electronic converters using sigma-delta A/D conversion," *IEEE Trans. Industry Applications*, vol.34, no.5, pp.1139-1146, Sep 1998
- [42] Y.G. Kononov, M.A. Ospishchev, and V.Y. Rudnev. "Current and voltage synchronous measurements using NI cRIO system with sigma-delta ADC NI 92xx and S.E.A. GPS modules", *18th International Workshop on ADC Modelling and Testing*, Benevento, Italy, September 15-17, 2014
- [43] P. Romano, M. Paolone, J. Arnold, and R. Piacentini, "An interpolated-DFT synchrophasor estimation algorithm and its implementation in an FPGA-based PMU prototype," in *Proc. 2013 IEEE Power & Energy Society General Meeting*, pp.1-5.
- [44] S. Maharjan, J.C.H. Peng and, J.E Martinez, "Improved off-nominal operation of phasor measurement units using discrete fourier transformation," *IEEE Power and Energy Conference at Illinois (PECI)*, Feb. 2015
- [45] F.L Walls and J. Gagnepain, "Environmental sensitivities of quartz oscillators," *IEEE Trans. Ultrasonics, Ferroelectrics, and Frequency Control*, vol.39, no.2, pp.241-249, March 1992
- [46] F.L Walls and John R Vig. "Fundamental limits on the frequency stabilities of crystal oscillators," *IEEE Trans. on Ultrasonics, Ferroelectrics, and Frequency Control*, vol.42, no.4, pp.576-589, July 1995
- [47] G. C. Zweigle, L. S. Anderson, and A. Guzman-casillas, "Apparatus and algorithm for estimating synchronized phasors at pre-determined times referenced to an absolute time standard in an electrical system," U.S. Patent 7 480 580, Jan. 20, 2009

- [48] B.P. McGrath, D.G. Holmes, J.J.H. Galloway, "Power converter line synchronization using a discrete Fourier transform (DFT) based on a variable sample rate," *IEEE Trans. Power Electron.*, vol.20, no.4, pp.877-884, July 2005
- [49] T. Xia, "Frequency Monitoring Network (FNET) Algorithm Improvements and Application Development," Ph.D. dissertation, Dept. of EECS, Virginia Tech., Blacksburg, VA, 2010.
- [50] J. Chen, "Accurate frequency estimation with phasor angles," M.Sc.thesis, Bradley Dept. Elect. Comput. Eng., Virginia Polytechnic Inst. State Univ., Blacksburg, VA, 1994.
- [51] J.E Tate and T.J Overbye, "Line Outage Detection Using Phasor Angle Measurements," *IEEE Trans. Power Syst.*, vol.23, no.4, pp.1644-1652, Nov. 2008
- [52] L. Zhan, Y. Liu, W. Yao, J. Zhao, and Y. Liu, "Utilization of Chip Scale Atomic Clock for Synchrophasor Measurements," *IEEE Trans. Power Del.*, vol. PP, no. 99, 2016.
- [53] Z. Zhang, S. Gong, Dimitrovski, A.D and H. Li, "Time Synchronization Attack in Smart Grid: Impact and Analysis," in, *IEEE Trans Smart Grid*, vol.4, no.1, pp.87-98, March 2013
- [54] SPACE WEATHER AND GPS SYSTEMS, <http://www.swpc.noaa.gov/impacts/space-weather-and-gps-systems>
- [55] W. Yao, Y. Liu, D Zhou, Z Pan, J. Zhao, M. Till, L. Zhu, L. Zhan, Q. Tang and Y. Liu, Impact of GPS Signal Loss and Its Mitigation in Power System Synchronized Measurement Devices, *IEEE Transactions on Smart Grid*, vol. 9, no. 2, pp. 1141-1149, March 2018
- [56] W. Yao, D. Zhou L. Zhan, Y. Liu, Y Cui, S. You and Y. Liu, GPS signal loss in the wide area monitoring system: Prevalence, impact, and solution, *Electric Power Systems Research*, vol.147, pp. 254-262, 2017.
- [57] Motorola, "M12 Oncore User's Guide Supplement," 2000, <http://www.cnssys.com/files/M12+UsersGuide.pdf>
- [58] P. Zhang and K. W. Chan, "Reliability Evaluation of Phasor Measurement Unit Using Monte Carlo Dynamic Fault Tree Method," *IEEE Trans Smart Grid*, vol. 3, no. 3, pp. 1235-1243, Sept. 2012.
- [59] Quantumtm, SA.45s CSAC datasheet., http://www.microsemi.com/document-portal/doc_view/133305-quantum-sa-45s-csac
- [60] L. Zhan and et al., Improvement of timing reliability and data transfer security of synchrophasor measurements, 2014 IEEE PES T&D Conference and Exposition, ,pp, 1-5, 2014
- [61] A. Mazloomzadeh, M. H. Cintuglu and O. A. Mohammed, "Development and evaluation of a laboratory based phasor measurement devices," Innovative Smart Grid Technologies Conference (ISGT), 2015 IEEE Power & Energy Society, Washington, DC, 2015, pp. 1-5
- [62] "Transmission Line Reference Book, 345kV and Above/Second Edition", EPRI, 1982.
- [63] G. Wijeweera, Bahreyni, Behraad, C. Shafai, A Rajapakse, D.R. Swatek, "Micromachined Electric-Field Sensor to Measure AC and DC Fields in Power Systems," *IEEE Trans. Power Delivery*, 2009
- [64] X. Sun, Q. Huang, L. J. Jiang and P. W. T. Pong, "Overhead High-Voltage Transmission-Line Current Monitoring by Magnetoresistive Sensors and Current Source Reconstruction at Transmission Tower," *IEEE Trans. Magnetics*, vol. 50, no. 1, pp. 1-5, Jan. 2014.
- [65] Q. Huang, W. Zhen and P. W. T. Pong, "A Novel Approach for Fault Location of Overhead Transmission Line With Noncontact Magnetic-Field Measurement," *IEEE Trans. Power Delivery*, vol. 27, no. 3, pp. 1186-1195, July 2012.

- [66] G. Zhang, Y. Liu, Y. Zhang. "Accurate Magnetic Field Sensor And Method for Wireless Phasor Measurement Unit". U.S. Patent. No. 8437969, 2010
- [67] X. Sun, Q. Huang, Y. Hou, L. Jiang and P. W. T. Pong, "Noncontact Operation-State Monitoring Technology Based on Magnetic-Field Sensing for Overhead High-Voltage Transmission Lines," *IEEE Trans. Power Delivery*, vol. 28, no. 4, pp. 2145-2153, Oct. 2013.
- [68] G. S. N. Raju. Electromagnetic Field Theory and Transmission Lines, , India: Pearson, June, 2006
- [69] G.B. Iyyuni and S.A. Sebo, "Study of transmission line magnetic fields", Power Symposium, 1990. Proceedings of the Twenty-Second Annual North American 15-16 Oct. 1990.pp:222-231.
- [70] F. Rahmatian, P.P Chavez, N. Jaeger, "230 kV optical voltage transducers using multiple electric field sensors," *IEEE Trans. Power Delivery*, vol.17, no.2, pp.417-422, Apr 2002
- [71] X. Zhang, "High precision dynamic power system frequency estimation algorithm based on phasor approach," Master. Dissertation, Virginia Polytechnic Institute and State University, Blacksburg, VA, 2004.
- [72] A.G. Phadke, J.S. Thorp and M.G. Adamiak, "A new measurement technique for tracking voltage phasors, local system frequency, and rate of change of frequency," *IEEE Trans. Power App. Syst.*, vol. PAS-102, no.5, pp.1025-1038, May 1983.
- [73] R. F. Nuqui, M. Zarghami and M. Mendik, "The impact of optical current and voltage sensors on phasor measurements and applications," IEEE PES T&D 2010, New Orleans, LA, USA, 2010, pp. 1-7.
- [74] P. Niewczas and J. R. McDonald, "Advanced Optical Sensors for Power and Energy Systems Applications," *IEEE Instrum Meas Magazine*, vol. 10, no. 1, pp. 18-28, Feb. 2007.
- [75] W. Yao, Y. Zhang and et al, "Pioneer Design of Non-contact Synchronized Measurement Devices Using Electric and Magnetic Field Sensors," *IEEE Trans on Smart Grid*, early access, April, 2017
- [76] D. M. Lavery, R. J. Best and et al, "The OpenPMU Platform for Open-Source Phasor Measurements," *IEEE Trans. Instrum. Meas*, vol. 62, no. 4, pp. 701-709, April 2013.
- [77] H. Lu, L. Zhan, Y. Liu and W. Gao, "A Microgrid Monitoring System Over Mobile Platforms," *IEEE Trans. Smart Grid*, vol. 8, no. 2, pp. 749-758, March 2017.
- [78] K. A. Salunkhe and A. Kulkarni, "A wide area synchronized frequency measurement system using network time protocol," in Proceedings of the 16th National Power System Conference, 2010, pp. 266–271.
- [79] H. Lu, L. Zhan, Y. Liu and W. Gao, "Power grid frequency monitoring over mobile platforms," IEEE International Conference on Smart Grid Communications (SmartGridComm), Venice, 2014, pp. 505-510.
- [80] H. Lu, L. Zhan, Y. Liu and Wei Gao, "A GPS-free power grid monitoring system over mobile platforms," 2015 IEEE Power & Energy Society General Meeting, Denver, CO, 2015, pp. 1-5.
- [81] D. Macii, D. Petri, and A. Zorat, "Accuracy Analysis and Enhancement of DFT-Based Synchrophasor Estimators in off-Nominal Conditions," *IEEE Trans on Instru and Meas*, vol. 61, pp. 2653-2664, 2012.
- [82] MAXIM Integrated (2007), "MAX3421E, USB peripheral/host controller with SPI interface," copyright Maxim Integrated Products

- [83] W. Yao, H. Lu, M. Till, W. Gao, Y. Liu, Synchronized Wireless Measurement of Power System Frequency using Mobile Embedded Systems, *IEEE Transactions on Industrial Electronics*, vol. 65, no. 3, pp. 2775-2784, March 2018.
- [84] A. Moreno-Munoz, V. Pallares-Lopez, J. J. Gonzalez de la Rosa, R. Real-Calvo, M. Gonzalez-Redondo and I. M. Moreno-Garcia, "Embedding Synchronized Measurement Technology for Smart Grid Development," *IEEE Trans. Ind. Informat.*, vol. 9, no. 1, pp. 52-61, Feb. 2013.
- [85] J. Zhao, J. Tan, L. Wu, L. Zhan, W. Yao, Y. Liu, J. R. Gracia, P. Ewing, "Impact of Measurement Error on Synchrophasor Applications," *IEEE Power and Energy Society General Meeting*, Chicago, IL, 2017, pp.1-5
- [86] J. Zhao, L. Zhan, Y. Liu, H. Qi, J. R. Garcia and P. D. Ewing, "Measurement accuracy limitation analysis on synchrophasors," *2015 IEEE Power & Energy Society General Meeting*, Denver, CO, 2015, pp. 1-5.
- [87] D. Zhou et al., "Distributed Data Analytics Platform for Wide-Area Synchrophasor Measurement Systems," *IEEE Trans on Smart Grid*, vol. 7, no. 5, pp. 2397-2405, Sept. 2016.
- [88] Yi Cui , Ling Wu, Wenpeng Yu, Yong Liu, Wenxuan Yao, Dao Zhou, Yilu Liu, Inter-area oscillation statistical analysis of the U.S. Eastern interconnection, vol. 2017, issue 11, November 2017, pp. 595 – 605
- [89] Y. Ye, J. Dong and Y. Liu, "Analysis of power system disturbances based on distribution-level phasor measurements," *IEEE Power and Energy Society General Meeting*, San Diego, CA, 2011, pp. 1-7.
- [90] G. Hua, J. Goh, and V. L. L. Thing, "A dynamic matching algorithm for audio timestamp identification using the enf criterion," *IEEE Trans. Inf. Forensics Security*, vol. 9, no. 7, pp. 1045–1055, July 2014
- [91] C. Grigoros, "Applications of ENF criterion in forensic audio, video, computer and telecommunication analysis," *Forensic Science International*, vol. 167, no. 23, pp. 136 – 145, 2007, selected Articles of the 4th European Academy of Forensic Science Conference (EAFS2006) June 13-16, 2006 Helsinki, Finland.
- [92] Y. Liu, Z. Yuan, P. N. Markham, R. W. Conners, and Y. Liu, "Application of power system frequency for digital audio authentication," *IEEE Trans. Power Del.*, vol. 27, no. 4, pp. 1820–1828, Oct 2012.
- [93] R. Garg, A. L. Varna, A. Hajj-Ahmad, and M. Wu, "“seeing ” ENF: Power-signature-based timestamp for digital multimedia via optical sensing and signal processing," *IEEE Trans. Inf. Forensics Security*, vol. 8, no. 9, pp. 1417–1432, Sept 2013.
- [94] D. P. N. Rodriguez, J. A. Apolinario, and L. W. P. Biscainho, "Audio authenticity: Detecting ENF discontinuity with high precision phase analysis," *IEEE Trans. Inf. Forensics Security*, vol. 5, no. 3, pp. 534–543, Sept 2010.
- [95] M. M. Elmesalawy and M. M. Eissa, "New forensic ENF reference database for media recording authentication based on harmony search technique using GIS and wide area frequency measurements," *IEEE Trans. Inf. Forensics Security*, vol. 9, no. 4, pp. 633–644, April 2014.
- [96] H. Ma and H. Li, "Analysis of frequency dynamics in power grid: A bayesian structure learning approach," *IEEE Trans. Smart Grid*, vol. 4, no. 1, pp. 457–466, March 2013
- [97] A. Hajj-Ahmad, R. Garg, and M. Wu, "ENF-based region-of-recording identification for media signals," *IEEE Trans. Inf. Forensics Security*, vol. 10, no. 6, pp. 1125–1136, June 2015.

- [98] L. Fu, P. N. Markham, R. W. Conners, and Y. Liu, "An improved discrete fourier transform-based algorithm for electric network frequency extraction," *IEEE Trans. Inf. Forensics Security*, vol. 8, no. 7, pp. 1173–1181, July 2013.
- [99] R. Garg, A. Hajj-Ahmad, and M. Wu, "Geo-location estimation from electrical network frequency signals," *ICASSP*, pp. 2862–2866, 2013
- [100] A. Hajj-Ahmad, R. Garg, and M. Wu, "Instantaneous frequency estimation and localization for ENF signals," in *Proceedings of The 2012 Asia Pacific Signal and Information Processing Association Annual Summit and Conference*, Dec 2012, pp. 1–10.
- [101] Y. Zhang, P. Markham, and et al., "Wide-area frequency monitoring network FNET architecture and applications," *IEEE Trans. Smart Grid*, vol. 1, no. 2, pp. 159–167, Sept 2010
- [102] Y. Liu, C. Yao, C. Sun, and Y. Liu, "The authentication of digital audio recordings using power system frequency," *IEEE Potentials*, vol. 33, no. 2, pp. 39–42, March 2014.
- [103] Y. Liu, Z. Yuan, P. N. Markham, R. W. Conners, and Y. Liu, "Wide-area frequency as a criterion for digital audio recording authentication," in *2011 IEEE Power and Energy Society General Meeting*, July 2011, pp. 1–7
- [104] Y. Liu, Z. Yuan, P. N. Markham, R. W. Conners, and Y. Liu, "Power grid frequency data conditioning using robust statistics and b-spline functions," in *2012 IEEE Power and Energy Society General Meeting*, July 2012, pp. 1–6.
- [105] W. Li, J. Tang, J. Ma, and Y. Liu, "Online detection of start time and location for hypocenter in north America power grid," *IEEE Trans. Smart Grid*, vol. 1, no. 3, pp. 253–260, Dec 2010
- [106] K. L. V. Iyer, X. Lu, Y. Usama, V. Ramakrishnan, and N. C. Kar, "A twofold daubechies-wavelet-based module for fault detection and voltage regulation in SEIGs for distributed wind power generation," *IEEE Trans. Ind. Electron.*, vol. 60, no. 4, pp. 1638–1651, April 2013
- [107] S. You, Y., Liu, M. Till, J. Zhao, W. Yao, D. Zhou, L. Wu, Y. Su, .X. Zhang and Y. Liu, *Disturbance Location Determination Based on Electromechanical Wave Propagation in FNET/GridEye-a Distribution-Level Wide-Area Measurement System*, *IET Generation, Transmission & Distribution*, vol. 11, no. 18, pp. 4436–4443, 12 21 2017.
- [108] Y. Liu, S. You, P. Markam, "Observation and Applications of Electromechanical Wave Propagation Based on FNET/GridEye, a Wide-Area Frequency Monitoring Network", *IFAC World Congress*, 2017

Appendix

Appendix A

Selected Publications during Ph.D study

1. Journal Papers

- [J1] **W. Yao**, H. Lu, M. Till, W. Gao, Y. Liu, Synchronized Wireless Measurement of Power System Frequency using Mobile Embedded Systems, *IEEE Transactions on Industrial Electronics*, vol. 65, no. 3, pp. 2775-2784, March 2018.
- [J2] **W. Yao**, Y. Liu, D Zhou, Z Pan, J. Zhao, M. Till, L. Zhu, L. Zhan, Q. Tang and Y. Liu, Impact of GPS Signal Loss and Its Mitigation in Power System Synchronized Measurement Devices, *IEEE Transactions on Smart Grid*, Accepted-in press
- [J3] **W. Yao**, Y. Zhang, M. Till, Y. Liu and Y. Liu. Pioneer Design of Non-contact Synchronized Measurement Devices Using Electric and Magnetic Field Sensors. *IEEE Transactions on Smart Grid*, Accepted-in press
- [J4] **W. Yao**, L Zhan; Y Liu, M. Till, J. Zhao, L. Wu, Z. Teng and Y. Liu, A Novel Method for Phasor Measurement Unit Sampling Time Error Compensation, *IEEE Transactions on Smart Grid* , Accepted-in press
- [J5] **W. Yao**, Q Tang, Z. Teng, Y. Gao and H. Wen. Fast S-Transform for Time-Varying Voltage Flicker Analysis, *IEEE Transactions on Instrumentation & Measurement* , vol. 63, no. 1, January 2014
- [J6] **W. Yao**, Z. Teng, Q. Tang and Y. Gao, Measurement of power system harmonic based on adaptive Kaiser self-convolution window, *IET Generation, Transmission & Distribution*, vol. 10, no. 2, pp. 390-398, 2016.
- [J7] **W. Yao**, J. Zhao, M. Till, S. You, Y. Liu, Y. Cui and Y. Liu, Source Location Identification of Distribution-level Electric Network Frequency Signals at Multiple Geographic Scales, *IEEE Access*,vo.5, pp.11166-11175, 2017
- [J8] **W. Yao**, Z. Teng, Q. Tang and P. Zuo, Adaptive Dolph-Chebyshev Window based S Transform in Time-Frequency Analysis, *IET Signal Process*, vol. 8, no. 9, pp. 927-937, 2014.
- [J9] **W. Yao**, David Wells, Daniel King, Andrew Herron, Thomas King, Yilu Liu, Utilization of optical sensors for phasor measurement units, *Electric Power Systems Research*, vol.156, March 2018, pp 12-14,
- [J10] **W. Yao**, D. Zhou L. Zhan, Y. Liu, Y Cui, S. You and Y. Liu, GPS signal loss in the wide area monitoring system: Prevalence, impact, and solution, *Electric Power Systems Research*, vol.147, pp. 254-262, 2017
- [J11] **W. Yao**, K. Wang, D. Zhou, H. Lu, P. Markham, W. Gao and Y. Liu, Development of Distribution Level Phasor Measurement on Mobile Devices for Electric Energy Systems, *IEEE Transactions on Smart Grid*, under review
- [J12] H. Wen, C. Li, **W. Yao**, Power System Frequency Estimation of Sine-wave Corrupted With Noise By Windowed Three-point Interpolated DFT, *IEEE Transactions on Smart Grid*,

Accepted-in press

- [J13] H. Wen, J. Zhang, **W. Yao**, L. Tang, FFT-based Amplitude Estimation of Power Distribution Systems Signal Distorted by Harmonics and Noise, IEEE Transactions on Industrial Informatics, Accepted-in press
- [J14] S. You, Y. Liu, G. Kou, X. Zhang, **W. Yao**, Y. Su, S. Hadley and Y. Liu, Non-Invasive Identification of Inertia Distribution Change in High Renewable Systems Using Distribution Level PMU, IEEE Transactions on Power System, vol. 33, no. 1, pp. 1110-1112, Jan. 2018.
- [J15] L. Zhan, Y. Liu, **W. Yao**, J. Zhao and Y. Liu, Utilization of Chip-Scale Atomic Clock for Synchrophasor Measurements, IEEE Transactions on Power Delivery, vol. 31, no. 5, pp. 2299-2300, Oct. 2016.
- [J16] Y. Liu, L. Zhan, Y. Zhang, P. Markham, D. Zhou, J. Guo, Y. Lei, G. Kou, **W. Yao**, J. Chai and Y. Liu, Wide-Area-Measurement System Development at the Distribution Level: An FNET/GridEye Example, IEEE Transactions on Power Delivery, vol. 31, no. 2, pp. 721-731, April 2016.
- [J17] Y. Liu, S. You, **W. Yao**, Y. Cui, L. Wu, D. Zhou, J. Zhao, H. Liu and Y. Liu, A Distribution Level Wide Area Monitoring System for the Electric Power Grid–FNET/GridEye, IEEE Access, vol. 5, pp. 2329-2338, 2017.
- [J18] Y. Zhang, **W. Yao**, S. You, W. Yu, L. Wu, Y. Cui, Y. Liu, Impacts of Power Grid Frequency Deviation on Time Error of Synchronous Electric Clock and Worldwide Power System Practices on Time Error Correction, energies, vol.9, no.9, 1283, 2017
- [J19] S. You, G. Kou, Y. Liu, X. Zhang, Y. Cui, M. Till, **W. Yao** and Y. Liu. Impact of High PV Penetration on the Inter-area Oscillations in the U.S. Eastern Interconnection, IEEE Access, vol. 5, pp. 4361-4369, 2017.
- [J20] S. You, Y., Liu, M. Till, J. Zhao, **W. Yao**, D. Zhou, L. Wu, Y. Su, .X. Zhang and Y. Liu, Disturbance Location Determination Based on Electromechanical Wave Propagation in FNET/GridEye-a Distribution-Level Wide-Area Measurement System, IET Generation, Transmission & Distribution, vol. 11, no. 18, pp. 4436-4443, 12 21 2017.
- [J21] Yong Liu, **W. Yao** and et al., Recent developments of FNET/GridEye - A situational awareness tool for smart grid, CSEE Journal of Power and Energy Systems, vol. 2, no. 3, pp. 19-27, Sept. 2016.
- [J22] Yi Cui , Ling Wu, Wenpeng Yu, Yong Liu, **W. Yao**, Dao Zhou, Yilu Liu, Inter-area oscillation statistical analysis of the U.S. Eastern interconnection, vol. 2017, issue 11, November 2017, pp. 595 – 605

2. Conference Papers

- [C1] Y. C. Zhang, **W. Yao**, J. Culliss, G. Zhang, Z. Teng and Y. Liu, "Electrical field based wireless devices for contactless power grid phasor measurement," 2014 *IEEE Power and Energy Society General Meeting*, National Harbor, MD, 2014, pp. 1-5.
- [C2] J. Zhao, J. Tan, L. Wu, L. Zhan, **W. Yao**, Y. Liu, J. R. Gracia, P. Ewing, " Impact of Measurement Error on Synchrophasor Applications," *IEEE Power and Energy Society General Meeting*, Chicago, IL, 2017, pp.1-5
- [C3] J. Chai, J. Zhao, **W. Yao**, J. Guo and Y. Liu, "Application of wide area power system measurement for digital authentication," 2016 *IEEE/PES Transmission and Distribution Conference and Exposition (T&D)*, Dallas, TX, 2016, pp. 1-5.
- [C4] S. You, J. Guo, **W. Yao**, S. Wang, Y. Liu, and Y. Liu, "Ring-down oscillation mode identification using multivariate empirical mode decomposition," in Proc. 2016 IEEE Power and Energy Society General Meeting, 2016, pp. 1-5.

Appendix B

U.S. Patent application during Ph.D study

- [P1] Yilu Liu, **Wenxuan Yao**, Lingwei Zhan, Wei Gao, Haoyang Lu. Mobile electric field sensor based phasor measurement unit for monitoring an electric power grid, (Application No. 14/340120, Filed in July 2014, issued in April 2018)
- [P2] Yilu Liu, Lingwei Zhan, **Wenxuan Yao**. Universal Grid Analyzer power grid, (Application No. 14/802307, filed in July 2015, Published)
- [P3] **Wenxuan Yao**, Jiecheng Zhao, Yi Cui, Yilu Liu, Magnetic Field Based Wireless GMD/EMP-E3 Impact Monitoring Device,US Patent Application, No. 15/349779 (Filed in Nov. 2016)
- [P4] **Wenxuan Yao**, Jiecheng Zhao, Yilu Liu, Lingwei Zhan, Andrew Herron, Daniel King, Thomas King, Ultra-Fast synchronized measurement algorithms for power system fast situational awareness (Filed in Feb. 2017)
- [P5] Yilu Liu, Yi Cui, **Wenxuan Yao**, Ling Wu, Yong Liu and Feifei Bai, Power Disturbance Localization Based on Hybrid Computational Intelligence Techniques (US Patent, filled in April 2017)
- [P6] Yilu Liu, Jidong Chai, Jiecheng Zhao, **Wenxuan Yao**. Tampering detection and location identification of digital audio recordings, (Application No. 14/992974., Filed in Feb. 2016, Published)

Vita

Wenxuan Yao received his B.S. degree in electrical engineering from Hunan University in 2011. He started his Ph. D study at the University of Tennessee, Knoxville, in August 2014. His research interests include wide-area power system monitoring, synchrophasor measurement applications, embedded system development, power quality diagnosis and big data analysis for power system.